Analytical Modeling and Numerical Simulations of Time Delays in Attosecond Streaking of One- and Two-Photon Ionization

by

Cory Scott Goldsmith

B.S., University of Georgia, 2012

A thesis submitted to the

Faculty of the Graduate School of the

University of Colorado in partial fulfillment

of the requirements for the degree of

Doctor of Philosophy

Department of Chemistry and Biochemistry

2018

This thesis entitled:
Analytical Modeling and Numerical Simulations of Time Delays in Attosecond Streaking of One- and Two-Photon Ionization
written by Cory Scott Goldsmith
has been approved for the Department of Chemistry and Biochemistry

_____

Prof. Andreas Becker

_____

Prof. Agnieszka Jaroń-Becker

Date _____

The final copy of this thesis has been examined by the signatories, and we find that both the content and the form meet acceptable presentation standards of scholarly work in the above mentioned discipline.

Goldsmith, Cory Scott (Ph.D., Chemical Physics)

Analytical Modeling and Numerical Simulations of Time Delays in Attosecond Streaking of One- and Two-Photon Ionization

Thesis directed by Prof. Andreas Becker

The generation of attosecond-duration (1 as = 10^{-18} s) coherent light through the process of high-order harmonic generation has opened the perspective for probing fundamental processes, such as photoionization, on the natural timescale of electron dynamics in matter. One probing technique is the attosecond streaking method, in which the momentum of the photoelectron is measured as a function of the time delay between the ionizing, attosecond extreme ultraviolet (XUV) pulse, and a weak, femtosecond near-infrared (NIR) pulse which streaks the momentum of the photoelectron, known as a streaking trace. The observed trace contains time information about the photoionization process in the form of a time offset to the vector potential of the streaking field, known as the streaking time delay. Theoretical simulations show that for one-photon ionization this time delay is accumulated by the photoelectron in the continuum when propagating away from the parent ion, whereas for resonant two-photon ionization there exists an additional absorption delay which depends on the properties of the XUV pulse. In this thesis, we use both analytical techniques and numerical simulations to study the contributions of the total time delay observed in streaking, and further explore applications of the streaking time delay to gain insights into the electron dynamics.

We first derive an analytical formula for the streaking time delay in one-photon ionization. The predictions based on the model formula, which can be performed within seconds of computation time, are in good agreement with those of computationally extensive numerical simulations. We demonstrate that the analytical formula not only allows deeper insight into the nature of the time delay, but also offers the opportunity to effectively analyze other theoretical interpretations and potential effects, such as the effect of a chirp in the ionizing attosecond pulse on the time

delay measurement. We then apply time-dependent perturbation theory to derive an analytical formula for the absorption delay in resonant two-photon ionization. We use the analytical formula to demonstrate how the absorption delay can be controlled further by the attosecond pulse duration and central frequency in case of an isolated resonance. Furthermore, we show how multiple resonances within the bandwidth of the ionizing pulses as well as the streaking field influence the absorption delay in model systems as well as simple atoms and molecules. We conclude by exploring the option to apply isolated elliptically polarized attosecond pulses to obtain sub-attosecond temporal information via the observation of photoelectron angular distributions as a function of the ellipticity of the pulse.

Dedication

To my sister Rachel. We miss you dearly

Acknowledgements

There are too many people to acknowledge, but I'll do my best in making sure not to leave out too many. First and foremost I would like to thank my advisors Andreas and Agnieszka for helping me achieve my dream of becoming a PhD. I certainly could not have done this without their help. When I strayed too far, they were always there to guide me back to the right path. I also thank them for always supporting my efforts, even when I became distracted by other happenings in my life. I would also like to thank my committee members John Bohn, Carl Lineberger, Margaret Murnane, and David Jonas for intriguing conversations during my tenure at CU Boulder.

As was alluded to in my Dedication, my sister Rachel passed away in March 2015, during the work leading to this thesis. This was without a doubt, and probably will be forever, the hardest thing I have ever endured in my life. I would be lying if I said that it didn't cross my mind, several times, to quit graduate school during this time. However, the support of Andreas and Agnieszka, my fellow group members, and my parents allowed me to continue pursuing my doctorate. I pushed on, knowing that Rachel would want me to finish, and here I am. On that note, I would like to thank my parents for being the strongest people I know, and for giving me all of the opportunities in life that allowed me to make it to this point. They are the people who are most responsible for this work. For without them, I would be lost. I would also like to thank my grandmothers Therese Goldsmith and Rita Schoenberg, my Aunts Jean Goldsmith and Leah Stitzer, my Uncles Richard Youtz and Frederic Goldsmith, and my cousins Yaakov and Chaim Stitzer, David, Deborah, and Liz Ross, as well as Shifra Stitzer and Andy Berman.

I would also like to express my deepest gratitude towards my fellow group members, past and

present: Jing Su, Hongcheng Ni, Andrew Spott, Michelle Miller, Yuqing Xia, Carlos Hernández-García, Dan Weflen, Brynn Reiff, Joel Venzke, Tennesse Joyce, Andres Mora, and Zetong Xue. I would not have been able to make the jump to physics from chemistry if it were not for the help of these talented physicists. Many of them also helped me to become a programmer, as I had almost no programming experience coming into the group. Most importantly, they were always willing to assist when I needed to discuss anything, whether academic or personal. I truly consider all of you my friends, and appreciate having you in my life.

Working in JILA was an extraordinary experience, and I would like to thank the staff and my fellow JILAns for providing such a welcoming environment. I also would like to thank Professors Michael Duncan and Gary Douberly at the University of Georgia for mentoring me during my undergraduate education, and leading me on a path that resulted in my being here. Furthermore, I was fortunate enough to do an internship for Ableton AG in Berlin during the summer of my fourth year. This was one of the best summers of my life, and I would like to thank Neil Burdock and Ableton for the life-changing experiences I encountered there.

The friends I have made in Boulder and Denver after moving from Atlanta were extremely helpful during the last six years. There are countless times I was encouraged by close friends to continue when I felt like giving up, or made me happy when I was extremely depressed and/or exhausted. Being involved in the Denver music scene and Denver Trance Family also greatly helped with this. At that, I really should thank music itself. If I weren't composing music and playing shows during my PhD, I surely would've lost it.

I end by listing the names of friends that were most instrumental in motivating me and helping me to keep my eyes on the prize whilst completing this thesis, and for just making my life better in general (hopefully not forgetting any): Phoebe Tengdin, Alex Hopkins, Vince and Kara Casini, Devon Whitt, Zak Bissani, Kelsey Higgins, Timothy Watts, Patrick Farace, Joey Hreha, Evan Cerwonka, Andy Clark, Jordan Brown, Blas Lopez, Jay and Lyndzey Miller, Capers Hammond, Magnus and Spenser Fain, Chris Davis, Seth Hensel, Daniel Loyd, Niels Wright, Hayes Capers, Matthew McCloskey, John Cameron, Zaak Kerstetter, Brittany Nelson, Tom Osmond,

Maxi Bethge, Duncan Newell, Luigi Palagano, Evan Dackerman, Kimberly Hall, Stephen Kirkwood, Claire Hart, Steven Galloni, Stuart Mclellan, Craig Hughes, Rick Welsch, CJ Robinson, Ryan Reuting, Britton Lee, Micki Pi, Nick Bell, Greg and Cayla Kimble, Ashley Kisner, Mitch Zonneveld, Erik Sowers, and Brandon Heffernan.

Contents

Chapter

[1] The results of this section are also presented in C. Goldsmith, J. Su, A. Becker, and A. Jaroń-Becker, Phys. Rev. A **96**, 053410 (2017).

[2] The results of this section are also presented in C. Goldsmith, A. Jaroń-Becker, and A. Becker, J. Phys. B **51**, 025601 (2018).

[3] The results of this section are also presented in C. Goldsmith, J. Su, A. Jaroń-Becker, and A. Becker, J. Phys. B: At. Mol. Opt. Phys. **51**, 155602 (2018).

Tables

Table

Figures

Figure

Chapter 1

Introduction

1.1 The attosecond time scale and electron dynamics

The understanding of electron dynamics has played a fundamental role in technology and the advancement of atomic and molecular physics in the past century. Chemical reactions depend on the behavior of electrons, as does the response of atomic and molecular systems to external fields. In this sense, electrons participate in nearly every aspect of modern technology, and thus their dynamics are essential to understand. Considering the energy-time form of the uncertainty principle, $\Delta E \Delta t \sim \hbar$, a time scale of tens to hundreds of femtoseconds (1 fs $= 1 \times 10^{-15}$ s) is expected for energies of millielectron volts (1 meV $= 1 \times 10^{-3}$ eV), corresponding to the order of magnitude of the difference between vibrational energy levels in molecules. The separation of electronic states in an atom or molecule is on the order of eV, corresponding to an attosecond (1 as $= 1 \times 10^{-18}$ s) time scale. An alternative, intuitive picture of the time scale is given by the Bohr model for the hydrogen atom. Within this model, the classical kinetic energy of the electron in the ground state is $E_k = v^2/2 = 1/2$, and therefore the period of the classical orbit is $T = 2\pi/v = 2\pi$ in Hartree atomic units (a.u.). Therefore the atomic unit of time is 24.19 as $= 24.19 \times 10^{-18}$ s, which corresponds to the period of the classical electron circling in this first Bohr orbit divided by 2π.

In order to observe the dynamics of attosecond processes, it is necessary to use measurement tools with resolution of this magnitude (e.g., [2, 10, 13]). A video camera captures processes on millisecond time scales by taking snapshots with a shutter time quick enough to resolve the motion

of most macroscopic objects. To study the real-time evolution of electron dynamics by taking snapshots of its probability distribution, a "camera" with a shutter time on the attosecond time scale is required. It is thus expected that probing, and furthermore controlling electron dynamics is possible using pulses of light of durations on this time scale. The recent advent of high-order harmonic generation (HHG) in gases [30–40] has enabled us to generate isolated pulses and pulse trains of attosecond duration, which provides such a tool for observing electron dynamics.

Among the many interesting physical processes which occur in the attosecond time regime, photoionization is one which has a long history dating back to the beginning of quantum mechanics. In 1905, Albert Einstein demonstrated the photoelectric effect [41] (translation [42]), which led to the proposal of the existence of photons. Einstein showed that in order for the electron to escape the potential of its parent ion, it needed to absorb a light quanta (photon) with enough energy to overcome the binding energy of this potential, and that the final kinetic energy $E_{k,f}$ of such an electron is expressed in atomic units ($\hbar = m_e = e = 1$) as:

$$E_{k,f} = \sqrt{2\,(\omega - I_p)}, \tag{1.1}$$

where ω is the energy of the photon and I_p is the ionization potential, also known as the binding energy or work function. At the time when Einstein received the Nobel Prize in Physics, i.e., 1921, the physical interpretation of the ionization process concerning its temporal resolution remained elusive. With the advent of attosecond pulses, we now have the capabilities of probing the photoionization process on the natural time scale of the electron.

In 1931, the process of two-photon absorption was predicted by Maria Göppert-Mayer in her doctoral dissertation [43]. In such a process, the light interacting with the matter is sufficiently intense such that two-photons are absorbed in a transition. In relation to the photoelectric effect, this means that if $I_p > \omega$, the system may still be ionized by two photons if $I_p < 2\omega$, and in such a case the kinetic energy of the emitted electron is

$$E_{k,f} = \sqrt{2\,(2\omega - I_p)}. \tag{1.2}$$

As we will discuss in this thesis, there are differences in the dynamics of one- and two-photon

ionization which have important implications in the quest to use attosecond pulses to observe and control electrons. These differences as they relate to attosecond experiments, and specifically the attosecond streaking experiment (see section 1.3.1.1) were first pointed out by a former colleague, Jing Su [16, 20] in the proposal of a so-called absorption delay for a resonant two-photon ionization process. The present work builds upon the work of Su, as well as suggests how the idea of the absorption delay can be extended to different attosecond experiments.

1.2 Attosecond pulse generation via high harmonic generation

The effort towards studying dynamics in matter on decreasingly shorter time scales has driven technological advances over the past decades. After the invention of mode-locking in 1965, the minimum duration of laser pulses decreased continuously until 1986 when 6 fs pulses were generated [44]. As seen in Fig. 1.1, there was only marginal progress from 1986 until 2001, as a radically different technology was needed to break the 6 fs benchmark, which took 15 years to develop [38, 45–53]. This effort subsequently led to the development of ultrashort laser pulses from such prominent sources as ultrashort electron pulses [54], X-ray free electron laser pulses [55] as well as femtosecond laser pulses via the process of high harmonic generation [47, 48]. Strong laser pulses with peak intensities on the order of 10^{13} - 10^{15} W/cm^2 have field strengths of similar magnitude to the internal electric field caused by the Coulomb force in atoms and molecules. With such a high intensity, many non-linear processes can occur. One of these processes is high harmonic generation (HHG) in gases, which occurs when an intense laser beam (usually a near-infrared (NIR) Ti:Sapphire pulse) is focused into an atomic or molecular gas medium.

The HHG process has been most successfully described using a semi-classical three-step model [32–34]. According to this model, the incident laser electric field is sufficiently intense such that the Coulomb field of the atomic system is tilted significantly, and an electron now has sufficient probability of tunneling through the Coulomb barrier in a process called tunneling ionization, as shown in Fig. 1.2(a). After tunnel ionization has occured, the electron wavepacket is accelerated in the laser electric field first away and then, upon reversal of the field direction, back to the parent ion.

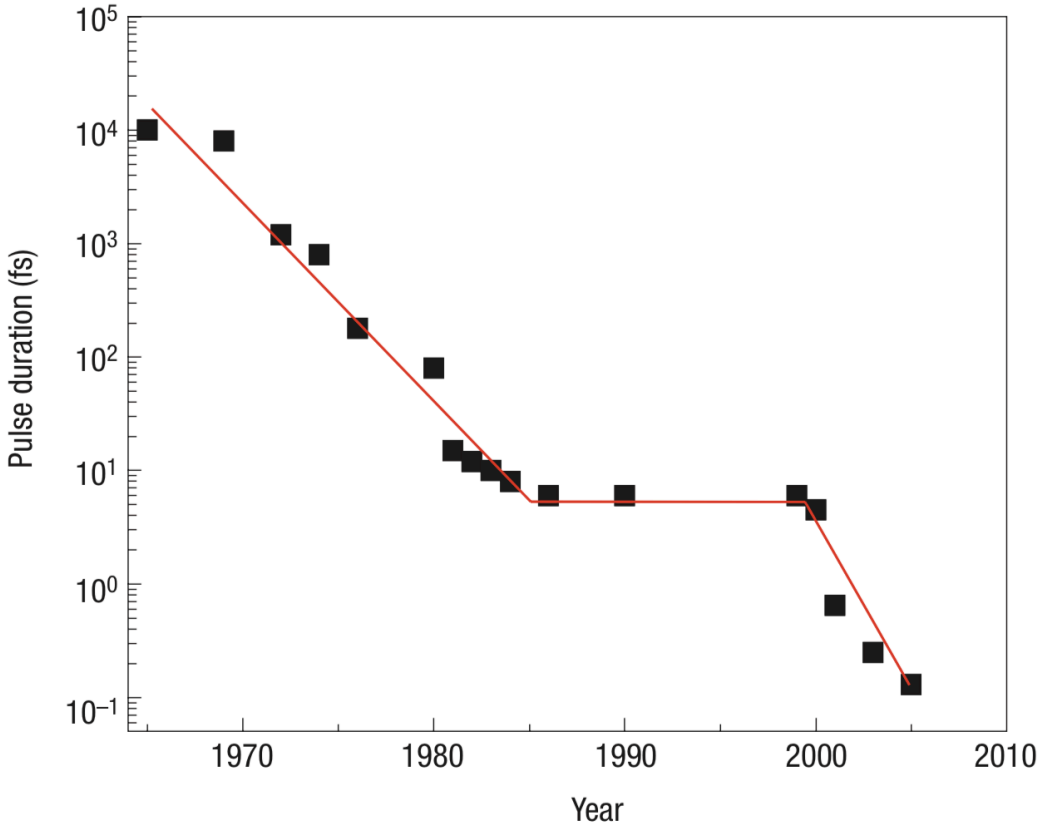

Figure 1.1: Development and decrease of laser pulse duration. The minimum duration continuously decreased until the mid 1980s. Following marginal progress for more than a decade, the femtosecond barrier (10^0 on the y-axis) was broken in 2001 (Taken from [2]).

Upon recombining with the parent ion, the energy gained from the absorption of many photons in the continuum from the driving field is emitted as a high energy photon. Using a quantum mechanical picture, the three step model is reflected via a product of three probability amplitudes, accounting for ionization, propagation, and recombination of the electron wavepacket. Due to the quasiperiodic repetition of this process every half cycle of the laser field, the resulting emission spectrum is discrete, consisting of odd harmonics of the driving laser's central frequency.

Some of the basic features of HHG spectra and the underlying mechanism can be understood from a simplified classical analysis [56], i.e. by solving Newton's equation in one dimension, for propagation of a point-like electron in an oscillating linearly polarized electric field $E(t)$:

$$\frac{d^2x}{dt^2} = -E(t)\,x, \tag{1.3}$$

assuming that the electron is released with zero velocity at the location of the parent ion (i.e., $x = 0$). In Figure 1.2 (d), the corresponding classical trajectories are shown, emerging at a central cycle of the driving field. The grey lines show classical trajectories which do not return to the parent ion, and therefore cannot be related to the generation of harmonics. The analysis of the trajectories, that return to the parent ion, leads to the prediction of a cut-off energy in the HHG spectrum of

$$E_{max} = I_p + 3.17U_p \simeq I\lambda_0^2, \tag{1.4}$$

where I_p is the ionization potential of the atom, $U_p = I/4\omega_0^2$ is the ponderomotive potential, and $I = E_0^2$ is the peak intensity of the laser pulse. This cutoff can clearly be seen in Fig 1.2(b). The ionization potential contributes to the cutoff energy via the recombination step, wherein the electron recombines to the ground state from the continuum, and the contribution related to the ponderomotive energy can be well predicted through the classical analysis of the possible electron trajectories contributing to HHG, neglecting the remaining Coulombic force from the parent ion. In Fig. 1.2(c), the kinetic energy of an electron released into an electric field at different points in time is plotted according to the simulated instant of ionization and predicted moment of recombination [4].

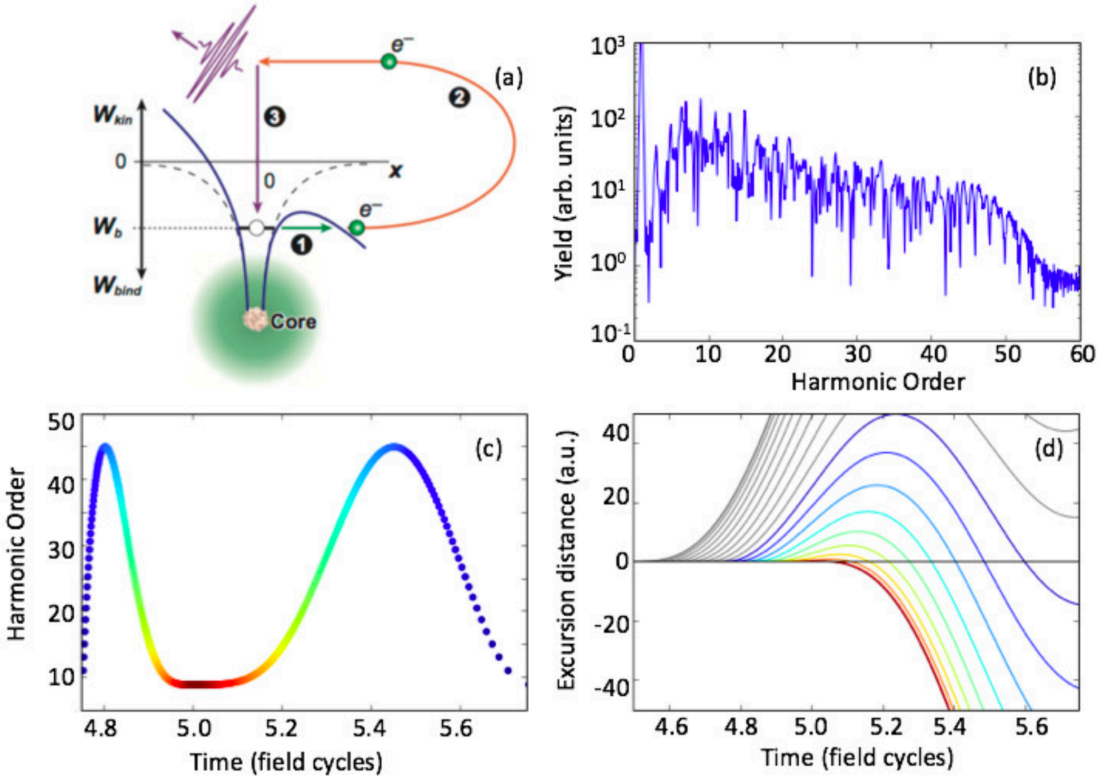

Figure 1.2: (a) HHG can be conceptualized via a three-step model instigated by the tunnel ionization of an electric wavepacket, which then propagates and accelerates in the incident laser field, and finally recombines with the parent core. Upon recombination, the energy absorbed from the electric field during propagation is released as a high-energy photon (from [3]). (b) A prototypical example of an HHG spectrum, featuring radiation with consistent efficiency over an extended interval of frequencies. (c) Via a classical model, one can predict the photon energies contributing to the HHG spectrum, indicating a time-dependent relationship between ionization, recombination, and the energy of the photon released. Each color corresponds to the same classical trajectory which is indicated in (d); Classical trajectories leading to HHG, grey lines indicate trajectories for ionization events without recombination, thus non-contributing to HHG (Taken from [4]).

Furthermore, there are several conclusions which can be drawn from the analysis giving rise to panels (c) and (d) in Fig. 1.2: for every energy except the cut-off frequency, electron propagation along two different trajectories contribute to each photon energy, which follow short and long excursion distances, respectively. Only the electrons ionized in the second and fourth quarters of an optical cycle of the laser field may be driven back to the parent ion for the recombination step. This temporal confinement of the underlying mechanism of HHG results in the generation of a train of attosecond pulses spaced by half of the optical period of the driving laser pulse.

For many applications, and for some techniques explored in this thesis, it is preferable to use an isolated attosecond pulse (IAP) as opposed to an attosecond pulse train (APT). The generation of IAPs is currently possible in a few different ways, which are summarized in Fig. 1.3. Using a time-frequency analysis [4], as well as according to the classical analysis within the three-step picture, it can be shown that the highest energies in an HHG spectrum are selectively emitted near the peak of the electric field. A method for generating IAPs that takes advantage of this fact is shown in Fig. 1.3 (a), in which one selects photon energies near the cutoff that are only emitted through one recombination event, by using a filter to absorb lower energy photons [5]. A second method for generating IAPs is called polarization gating. In this technique the polarization of the driving laser pulse is changed as a function of time (Fig. 1.3 (b)) [6]. Through this technique, near-linear polarization is achieved only near the center of the laser pulse. In this narrow window, the electron can recombine efficiently with the parent ion, releasing an attosecond pulse. The remaining electron wavepackets which are released at different ionization times, when the pulse is elliptically or circularly polarized, are driven away from the position of the parent ion, preventing recombination from taking place, and consequently an isolated pulse is emitted [6, 56, 57]. A third technique is shown in Fig. 1.3(c), where one introduces a time-dependent rotation of the wavefront direction of an intense, few-cycle laser field, providing a method for spatially separating the attosecond pulses in an APT [7, 58]. The emitted light acquires a time-dependent propagation direction based on the moment of production from the rotated intense field. Since the spatial position of each pulse in the train is well defined, the directional extraction of individual pulses may be achieved. Finally, we

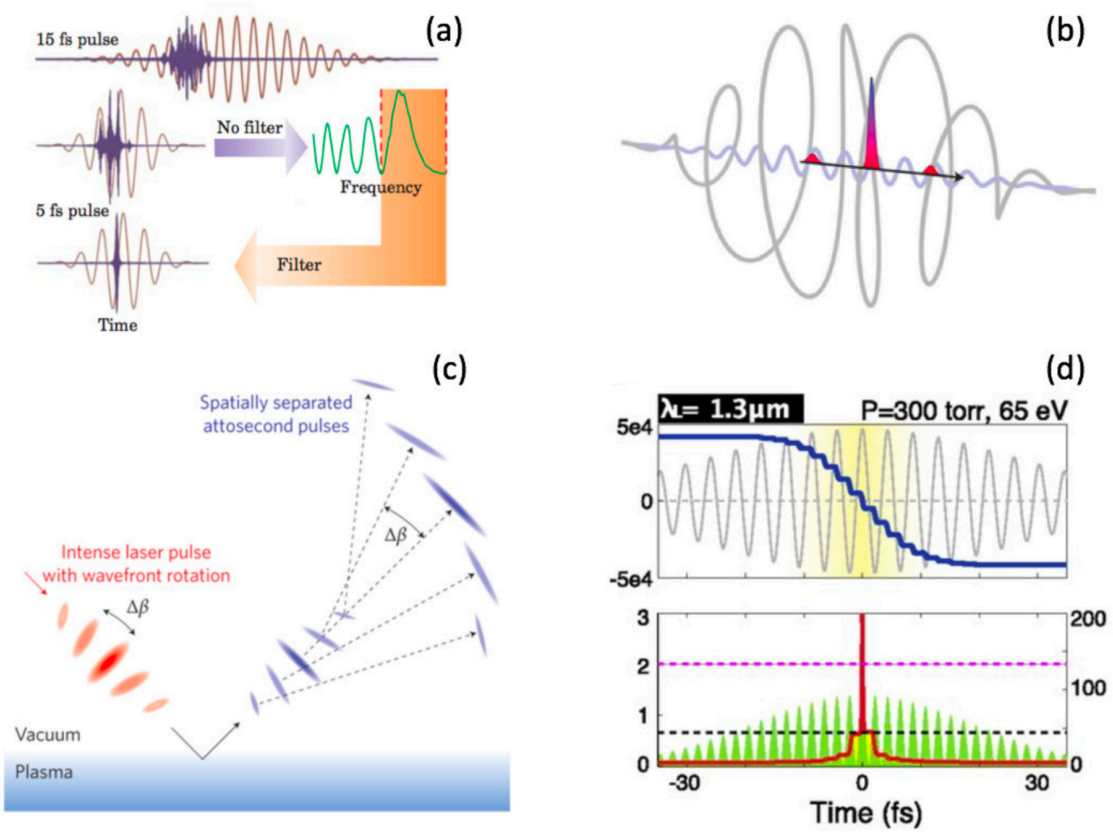

Figure 1.3: Methods developed to isolate attosecond pulses from HHG, including: (a) filtering cutoff frequencies [5], (b) varying the polarization of the electric field [6], (c) rotating the spatial wavefront of the driving field [7], and (d) manipulating the phase matching conditions of the emitted radiation [8] (Taken from [4]).

mention the generation of IAPs in systems featuring high intensities and midinfrared light sources, such as the case in Fig. 1.3(d) [8,40]. This technique relies upon the manipulation of phase-matching conditions for the emitted radiation in order to create an IAP. It is found that increasing the pulse duration and gas pressure allows the index of refraction of the target gas to change during the course of the light pulse, such that emission near the peak of the laser field can be favored and isolated from light emission occuring at different times.

Very recently, it has become possible to control the polarization state of the generated attosecond laser pulses [9]. This will come to our advantage towards the end of this thesis, when proposing a technique to probe time delays using isolated attosecond pulses of elliptical polarization to ionize atomic species. In Fig. 1.4, the technique for producing such pulses is shown. Huang *et al.* have shown that by using two ultrashort (down to a single cycle) counter-rotating elliptically polarized fundamental beams in a non-collinear geometry one can generate isolated elliptically polarized attosecond pulses [9]. By varying the ellipticity of the counter-rotating few-cycle incident pulses, one gains full control of the polarization states of isolated attosecond pulses.

1.3 Attosecond spectroscopy

Attosecond laser pulses have an intrinsically large bandwidth in energy, and are not yet intense enough to be used for attosecond pump, attosecond probe measurements. Therefore, a number of experiments using a combination of attosecond pulses and more intense femtosecond pulses have been used in the attempt of characterizing ultrafast phenomena. In this section, we summarize some of the more common techniques, putting an emphasis on those studied in this thesis. In general there are two different ways of extracting information about ultrafast dynamics using attosecond pulses; namely by measuring electrons ionized by the attosecond pulse, or by observing the absorption spectrum of the system. This means either detecting the photoelectrons, or the light before and after the propagation of the pulses through a target system.

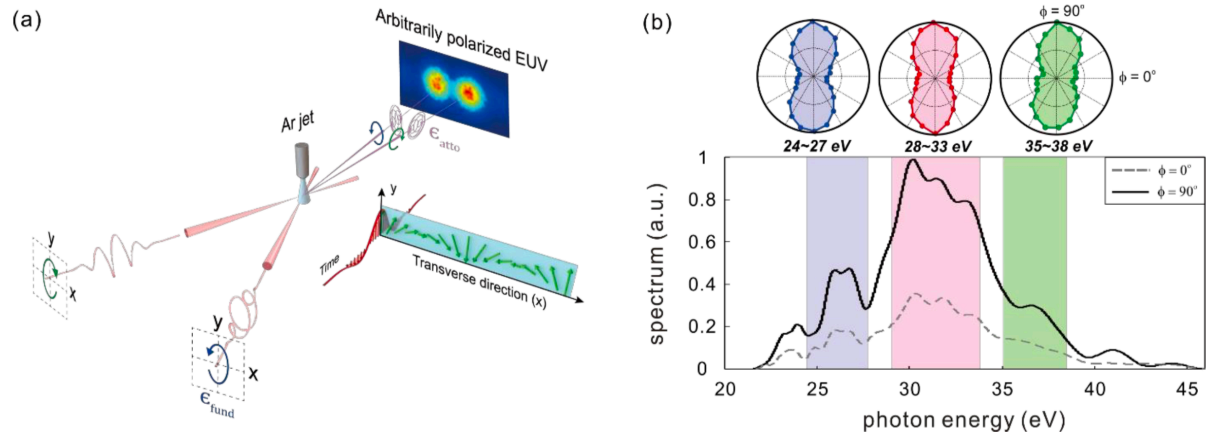

Figure 1.4: (a) Two elliptically polarized beams with opposite helicity are focused into a gas jet in a non-collinear fashion to generate an isolated attosecond pulse of arbitrary polarization. The inset displays the electric field distribution on the focal plane – rotating local electric field vectors crossing the transverse direction. The driving pulses are as short as one-cycle, generating isolated pulses. (b) Continuous spectra taken when an analyzer selects its polarization along the semi-major (black line) and semi-minor (gray dashed line) axes of elliptically polarized attosecond pulses with an average ellipticity of 0.43. The ellipticity is analyzed in three different photon energy ranges, and are nearly identical. (Taken from [9]).

1.3.1 Attosecond measurements via photoemission

1.3.1.1 Attosecond streaking

The concept of the streaking camera has been around for decades with the intention of characterizing the temporal structure of a short light pulse [59,60]. The scheme for this conventional streak camera is shown on the left side of Fig. 1.5. In such a measurement photoelectrons are emitted from a photocathode after interaction with a short light pulse. The time-dependent probability of the emission is proportional to the temporal intensity of the pulse. During the propagation towards the detector, the electron crosses a time-dependent voltage gradient $V(t)$, and therefore the electrons are deflected to a degree which is dependent on the moment of release of the electrons. Thus, the spatial distribution of the photoelectrons on the screen may be directly converted to a temporal pattern corresponding to the temporal structure of the incident pulse. Such a conventional streak camera can achieve this goal with subpicosecond (1 ps = 10^{-12} s) resolution for a voltage ramp that is within a fraction of a nanosecond (1 ns = 10^{-9} s) [59].

The attosecond streak camera originally shared the same goal as the conventional streak camera, but aimed to measure the temporal structure of an even shorter pulse, on the scale of attoseconds [53, 61–63]. The technique involves using two laser pulses: an attosecond XUV pulse which initiates an ultrafast process, typically ionization, and a few-cycle infrared streaking pulse that is used to modulate the final momentum of the electron according to its release instant (right side of Fig. 1.5). That is, photoelectrons ionized by the XUV pulse at different instants along the streaking field have different final momenta, which can be estimated by considering a classical electron propagating in a field, whilst neglecting the Coulomb potential of the ion core. Assuming that a free electron with momentum $\mathbf{k}_0$ is released into the continuum at an instant in time t_i, the particle interacts with the streaking field $\mathbf{E}_\mathrm{s}(t)$ as it propagates, and the final momentum is modified by the vector potential of this field $\mathbf{A}_\mathrm{s}(t)$ as

$$\mathbf{k}_f^{(\mathrm{free})}(t_i) \simeq \mathbf{k}_0 - \int_{t_i}^{T} \mathbf{E}_s(t)\, dt = \mathbf{k}_0 - \mathbf{A}_s(t_i), \tag{1.5}$$

where the streaking pulse has duration T such that $\mathbf{A}_s(T) = 0$ given that the pulse starts at

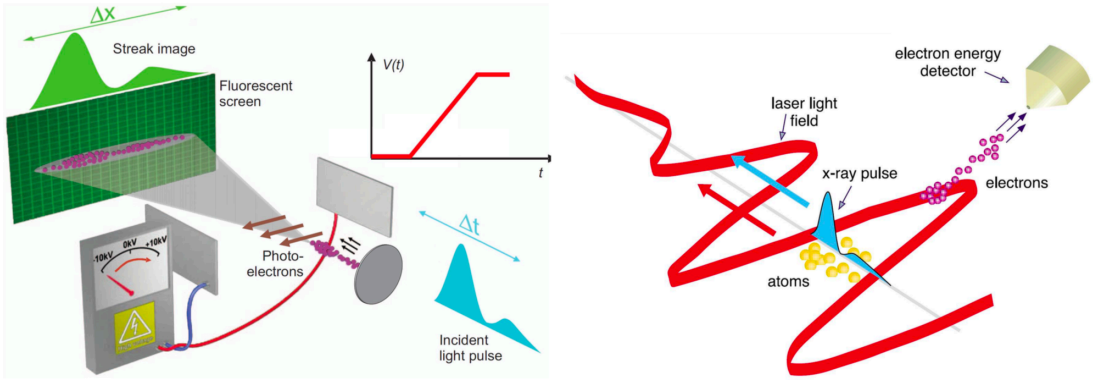

Figure 1.5: Conventional (left, taken from [10]) and attosecond (right, taken from [11]) streak cameras.

$t = 0$. The dynamics of the electron in the continuum however, depend on its interaction with the Coulomb potential of the residual ion, as well as the initial bound state $|n, l\rangle$ from which it was ionized. As a result, numerical simulations reveal that the final electron momentum as a function of release time shows a temporal offset with respect to the vector potential given by

$$\mathbf{k}_f^{(n,l)}(t_i) = \mathbf{k}_0 - \mathbf{A}_s(t_i + \Delta t_s^{(n,l)}), \tag{1.6}$$

where $\Delta t_s^{(n,l)}$ denotes the offset obtained for an electron which initially populated the bound state $|n, l\rangle$ of the atom. Throughout this thesis, we refer to this offset as the "streaking time delay", or "streaking delay" for short. We note that because the XUV pulse initiates the transition of the electron into the continuum in a streaking setup, the asymptotic momentum of the electron in Eqs. (1.5) and (1.6) is typically defined in terms of the XUV photon energy as $\mathbf{k}_0 = \hat{\mathbf{k}}\sqrt{2(\omega - I_p)}$, where ω the XUV photon energy, and I_p is the ionization potential corresponding to the initial state $|n, l\rangle$.

In an attosecond streaking experiment however, the exact form of the vector potential for the field is not measured. Instead, temporal information may be gained only through the comparison of traces resulting from photoelectrons exposed to the same streaking field, but which populated different orbitals initially. That is, in experiment one measures the quantity

$$\Delta t_{s,\text{expt}}^{(nl,n'l')} = \left|\Delta t_s^{(n,l)} - \Delta t_s^{(n',l')}\right| \tag{1.7}$$

for photoelectrons emitted from two different inital states $|n, l\rangle$ and $|n', l'\rangle$, as is demonstrated in Fig. 1.6. The first measurement of such a quantity was in an experiment by Schultze *et al.* [17], where they showed that $\Delta t_{s,\text{expt}}^{(2p,2s)}$ for neon atom is non-zero, which started a long debate in the theoretical literature as is discussed in the next Chapter. In this thesis, we will primarily focus on the theoretical determination of the streaking delay $\Delta t_s^{(n,l)}$ for various atomic species. In the remaining Chapters, the initial state is always implied in the context of the problem, and therefore we simply refer to this quantity hereforth as Δt_s.

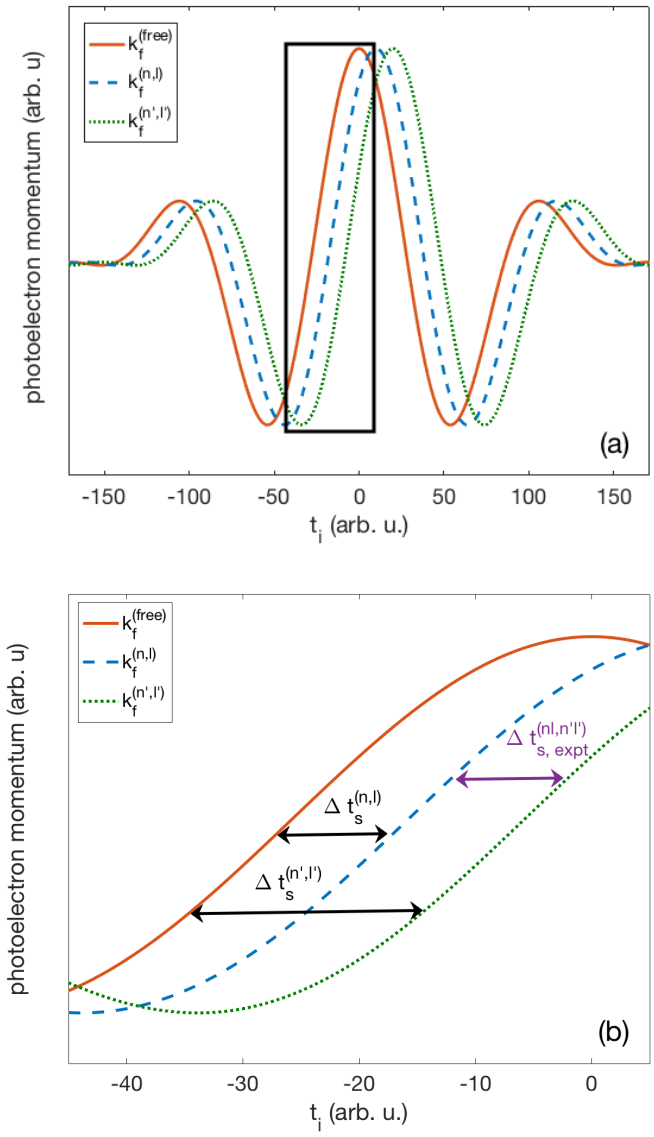

Figure 1.6: Conceptual visualization of the streaking time delays $\Delta t_{s,\text{expt}}^{(nl,n'l')}$, $\Delta t_s^{(n,l)}$, and $\Delta t_s^{(n',l')}$ for two different streaking traces as compared to that of a free particle. Panel (b) is an enlargement of the traces shown in panel (a) to clearly show the different time delays.

1.3.1.2 Reconstruction of attosecond beating by interfering two-photon transitions (RABBITT)

A similar experiment to streaking invokes an attosecond pulse train, as opposed to an isolated attosecond pulse, in conjunction with a long weak near-infrared pulse, and is known as the reconstruction of attosecond beating by interference of two-photon transitions, or RABBITT. In this method, an atom is ionized using a comb of high harmonics. The additional presence of the fundamental laser with frequency ω induces the formation of sideband peaks in between adjacent harmonics due to two-photon transitions including the absorption or emission of an infrared photon [12]. There are two distinct interfering quantum paths contributing to the same sideband (c.f., Fig. 1.7). Similar to attosecond streaking, the delay between the attosecond pulse train and the driving laser field, which we call t_i for consistency, is varied. It can be shown that the amplitude of the sideband signal from a given shell $|n, l\rangle$ is modulated as [51]

$$S\left(t_i\right) = \alpha + \beta \cos\left[2\omega\left(t_i - \Delta t_A - \Delta t_R^{(n,l)}\right)\right], \tag{1.8}$$

where α and β are two t_i-independent constants, Δt_A is a term proportional to the difference in phase between consecutive harmonics which is related to the group delay of the attosecond pulses, and $\Delta t_R^{(n,l)}$ represents the atomic delay due to the two-photon ionization process. We call this last term the RABBITT delay to make the analogy to the streaking delay. In combination with the measurement of the amplitudes of the harmonics, the phase information can be used to reconstruct the temporal profile of the attosecond pulses and the electron wavepackets initiated by the pulse train. In experiment, similar to streaking experiments, experimentalists typically observe a relative RABBITT time delay for the emission of electrons from two different orbitals, which is given by

$$\Delta t_{R,\text{expt}}^{(nl,n'l')} = \left|\Delta t_R^{(n,l)} - \Delta t_R^{(n',l')}\right|. \tag{1.9}$$

As an example, in the case of Ref. [12] $\Delta t_{R,\text{expt}}^{(3p,3s)}$ was measured for argon atom.

It has been shown [64] that in the limiting case of a continuous-wave, monochromatic field and a periodic repetition of identical attosecond pulses in the train, the RABBITT time delay

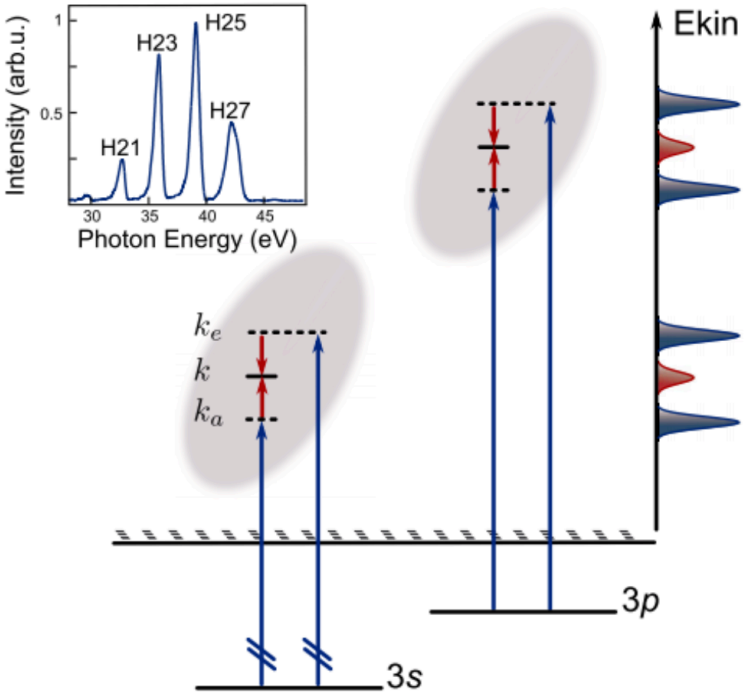

Figure 1.7: Schematic of the principle of the RABBITT technique, where for simplicity only two harmonics are indicated. Two electron wave packets originating from different shells are simultaneously created using the same comb of high harmonics. The outgoing wavepackets are further probed with a weak IR field. The experimental harmonic spectrum used is also shown (Taken from [12]).

agrees with the streaking time delay. RABBITT is in general less demanding experimentally than streaking, as it is easier to produce attosecond pulse trains than isolated pulses, and the probing infrared field can be weaker in RABBITT than in streaking [65]. Furthermore, since multiple sidebands are present in a typical RABBITT signal, time delays can be measured for multiple photoelectron kinetic energies. In contrast, a streaking experiment allows for the determination of a single time delay only.

1.3.1.3 Attoclock: Angular streaking

The attoclock is another attosecond measurement technique, different from streaking and RABBITT in the sense that no attosecond pulse is necessary to achieve attosecond time resolution. The experiment involves the application of a femtosecond (two-cycle or shorter) nearly-circular polarized laser pulse with matter. The rotation of the field acts as a "clock", where the electric field vector in the polarization plane serves as the clock-hand (see Fig. 1.8). The target is ionized by this pulse, and the final emission angle of the photoelectron is related to the instant of ionization. Typically, it is assumed that the ionization is initiated by a tunnel ionization event, and the propagation of the electron wavepacket in the combined fields of the circularly polarized field and Coulomb field of the remaining ion must be taken into account.

This technique has been used to resolve the so-called tunneling time-delay [13, 66]. This quantity relates to the question, if an electron wavepacket takes a finite time to tunnel through a barrier, and is that time measurable on an attosecond time scale? In this method, peak positions in the final angular distribution can be measured with an angular resolution of about 1°. For an 800 nm pulse typical in such an experiment, this corresponds to a temporal resolution of roughly 7.4 as [66].

1.3.2 Attosecond measurements via absorption

Another class of time-resolved attosecond measurements depends on measuring an absorption spectrum, as opposed to a photoelectron spectrum, as a function of delay between a femtosecond

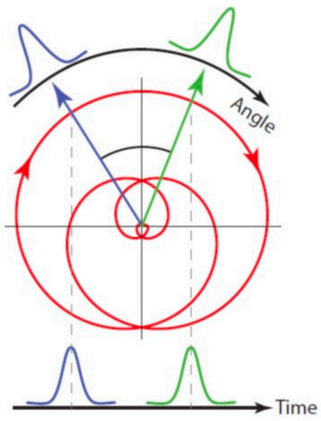

Figure 1.8: Schematic of the attoclock, where an electron wavepacket is liberated via tunnel ionization. The rotation of the polarization vector of the field acts as a minute hand for the attoclock, and the time-dependent emission can be mapped via the angular dependence of the distribution (Taken from [13]).

near-infrared pulse and an attosecond XUV pulse. In this thesis, we will show that such pump-probe techniques can be used to compliment photoemission experiments.

1.3.2.1 Attosecond transient absorption spectroscopy

Attosecond transient absorption spectroscopy (ATAS) is characterized by the absorption of the pump and probe light by a medium. The technique has some similarities to a classical Beer's Law absorption experiment in chemistry [14]. The amount of light which leaves the medium is different from that which was incident upon the medium. The amount of light absorbed depends upon the wavelength of the light and the system being probed. ATAS is different from classical absorption spectroscopy in that temporal resolution is achieved by delaying the near-infrared femtosecond pulse and the attosecond XUV pulse. The experiment can be performed where the infrared pulse precedes (conventional pulse sequence) or follows (unconventional pulse sequence) the XUV pulse. The response of the medium to the light at the single-atom/molecule level can be calculated as [14]

$$S(\omega,\tau) = 2\mathrm{Im}\left[\tilde{E}^{*}_{in}(\omega,\tau)\,\tilde{d}(\omega,\tau)\right], \tag{1.10}$$

where $\tilde{E}_{in}$ is the Fourier transform of the combined NIR-XUV electric fields, and $\tilde{d}$ is the Fourier transform of the time-dependent dipole $d(t) = -\langle \Psi(\mathbf{r};t) |\mathbf{r}| \Psi(\mathbf{r};t) \rangle$. Including the effects of macroscopic propagation via Maxwell's equations can improve agreement with experiment, as is seen in Fig. 1.9 where a comparison is shown between theoretical simulations with (b) and without (a) macroscopic propagation and experiment (c) for the transient absorption spectrum of helium atom [14]. In experiment, the spectrum is obtained by subtracting the spectrum of the combined fields leaving the sample from the original spectrum of the fields prior to traversing through the sample.

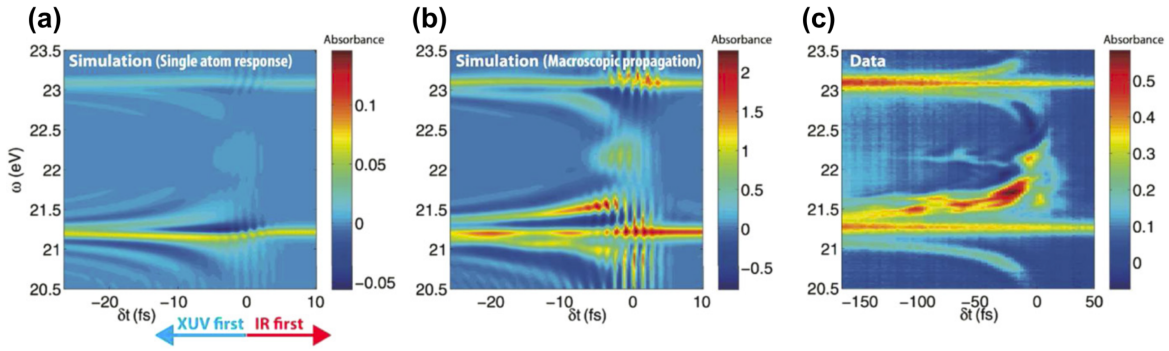

Figure 1.9: Single atom (a) and macroscopic (b) calculations of the transient absorption in helium, compared with experiment (c). It can be seen that macroscopic effects play a role in determining the absorption spectrum (Figures taken from [14], experiment by [15]).

1.4 Organization of this thesis

In the last section, we discussed how time delays in photoemission may be observed using the streaking or RABBITT techniques. In this context, we wish to contribute to the understanding how to time resolve simple quantum mechanical processes, such one- and two-photon ionization, using attosecond pulses. In our quest to understand such dynamics, we have used analytical models to explore the time delays measured in attosecond streaking experiments like that reported in Ref. [17]. We have considered the original application of streaking measurements related to one-photon ionization as well as their extensions to resonant two-photon ionization, involving an isolated

resonance as well as multiple resonances. Additionally we have explored the perspective to use the recently developed technique of generation of isolated elliptically polarized attosecond pulses to obtain information on a sub-attosecond time scale in an extension of the attoclock concept. The structure and organization of this thesis is given as follows:

Recently, it has been predicted [20, 67] that a resonant multiphoton process leads to an additional phase shift and therefore time delay, called the absorption time delay. We contribute to this discussion by analytically predicting such a delay in the case of an isolated resonance, and showing that it has a dependence upon the pulse duration and central frequency of the attosecond pulse. This additional delay is sensitive to the structure of the target, particularly in the case where multiple resonances are within the bandwidth of the ionizing attosecond pulse. In the overlapping resonance case, we show that transient absorption spectroscopy provides complementary information which sheds light on the mechanism. Additionally, we have begun the effort of extending the concept of the attoclock to isolated elliptically polarized attosecond pulses. To this end, we propose a new method where a single attosecond pulse is used to gain temporal information.

In Chapter 2, we review previous work regarding photoemission time delays in recent years, particularly as it relates to attosecond experiments such as streaking. To this end, we will briefly mention some of the key experimental observations of photoemission delays using attosecond techniques, and then continue with a discussion of past theoretical interpretations of the streaking delay for one-photon ionization. We further discuss recent work related to the absorption delay in resonant two-photon ionization in the context of both streaking and RABBITT methods.

In Chapter 3, we review the analytical and numerical models used in this thesis to solve the relevant time dependent Schrödinger equation (TDSE). We begin by formulating the approximations made in the semi-classical description of the interaction of attosecond laser pulses with matter. We then review time-dependent perturbation theory and scattering phases which provides the basis for the analytical models developed in the thesis. We conclude Chapter 3 by presenting our numerical method for solving the TDSE, including techniques for obtaining initial field-free states, propagation of the wavefunction in the time domain, absorbing boundary conditions, using

single active electron (SAE) potentials, and finally the extraction of the time delay from simulations of attosecond streaking.

In Chapter 4, we develop an analytical formula to further analyze and predict time delays in one-photon ionization. Our formula accurately reproduces, in a few seconds of computation time, the results of high-level TDSE simulations. Furthermore, we show that our analysis provides new insight into the separation of the streaking delay in the so-called sum rule. We then apply our formula to study recently proposed theoretical interpretations and potential other effects on the attosecond streaking measurements. For example, we show that the effect of the attochirp can be significant in a frequency regime close to the Cooper minimum in the photoionization cross section of argon atom.

Chapter 5 includes our studies regarding the absorption delay in resonant two-photon ionization, and in particular the difference between the case of an isolated resonance and overlapping resonances. We first develop an analytical formulation of the absorption delay in the case of an isolated resonance using time-dependent perturbation theory. The results obtained with this ansatz demonstrate the dependence of the absorption delay upon both the duration and the central frequency of the ionizing attosecond pulse. We then extend our studies to the case when multiple resonances are excited within the bandwidth of the attosecond XUV pulse, and discuss the potential influence of the streaking field on the absorption time delay in model systems as well as simple atoms and molecules.

In Chapter 6, we propose the use of isolated elliptically polarized XUV attosecond pulses to further study dynamics in photoemission. As a first step, we show that the angular distribution of the emitted photoelectron can be controlled with the ellipticity of the pulse. We then explore the potential application of isolated elliptically polarized attosecond pulses to so-called "ring-current" states. We then end with a summary of the work over these last six years.

Chapter 2

Delays in Photoionization and Previous Theoretical Analysis

As mentioned in the previous Chapter, the measurement of photoemission time delays can provide temporal information on the attosecond time scale. The concept of a time delay in quantum mechanics was first introduced in scattering theory, and dates back to the PhD work of Eisenbud in the late 1940s [68]. It was further developed by Wigner and Smith in the next decade [69, 70]. Given the assumption of a central potential, Eisenbud, Wigner, and Smith derived a group delay for the partial wave with angular momentum l of a scattered particle, evaluated asymptotically given that the potential decays faster than $1/r$ as:

$$\Delta t_{\mathrm{WS}}^{\mathrm{scat}}(E,l) = t_p(R) - t_0(R)|_{R\to\infty} = \left(\frac{\partial\phi_l(E)}{\partial E}\right|_{R\to\infty}, \tag{2.1}$$

where $\phi_l(E)$ is the scattering phase for the lth partial wave at electron kinetic energy E, and WS refers to "Wigner-Smith". The time delay is most simply defined as the difference of the time t_p, that the particle spends crossing the region R with the potential, and the time t_0 that a free particle would spend crossing the same region (see Fig. 2.1).

For the scattering off an ionic potential containing a short range part and a Coulomb term $-Z/r$ for nuclear charge Z, defining the time delay in this manner becomes problematic. It is well known [71] that the delay in this case may be decomposed as

$$\Delta t_{\mathrm{WS}}^{\mathrm{scat}}(E,l) = \Delta t_{\mathrm{short}}(E,l) + \Delta t_{\mathrm{phase}}(E,l) + \Delta t_{\log}(E) \tag{2.2}$$

where the first term $\Delta t_{\mathrm{short}}$ is the contribution from the short range part of the atomic potential, while $\Delta t_{\mathrm{phase}}$ and $\Delta t_{\log}$ are the well known "Coulomb phase" and "logarithmic" terms, respectively.

Note that the logarithmic term is independent of l, as the effect of the long-range part of the Coulomb potential on scattering is independent of angular momentum. These last two terms result from scattering off the $-Z/r$ part of the ionic potential for nuclear charge Z. However, whereas Δt_{phase} converges as $R \to \infty$, the term $\Delta t_{\log}$ diverges. Indeed, this term is responsible for the well known "logarithmic divergence" of the time delay in the case of a Coulomb potential [71, 72]. Therefore, one typically refers to the first two terms alone when discussing the "Wigner Smith" (WS) delay in the context of scattering off an ionic core with a long range Coulomb potential [22,73]:

$$\Delta t_{\text{WS}}(E,l) = \Delta t_{\text{short}}(E,l) + \Delta t_{\text{phase}}(E,l). \tag{2.3}$$

Since photoionization can be modeled as a "half-scattering" process, the discussion of a photoemission delay in Ref. [17] reignited theoretical interest in the relevance of the WS delay in this context (e.g. [29, 74–79]). Specifically, the time delays measured in both streaking and RABBITT experiments (c.f., section 1.3.1) have been attributed to the sum of the WS delay and an additional term. Yet, the interpretation of the measured time delay and the extraction of the WS delay in attosecond experiments have been a source of much controversy over the past seven years, particularly due to the disagreement of results of numerical simulations with data of the streaking measurement of Ref. [17]. Furthermore, as will be discussed in section 2.3, extension of the original attosecond time delay concept, as for example in Refs. [20] and [80], showed that the time delay measured in attosecond streaking and RABBITT respectively, includes an additional contribution, called the absorption delay, in the case of resonant two-photon ionization processes (as compared to non-resonant ionization). In this Chapter, we will review some of the experimental results important to photoemission delays in section 2.1. Then, we will review past theoretical work with respect to the different contributions to the streaking delay in sections 2.2 and 2.3.

2.1 Experimental observations

The attosecond streak camera, an established experiment for pulse characterization in attosecond science [53, 61–63], was used by Schultze *et al.* [17] to demonstrate the possible use of

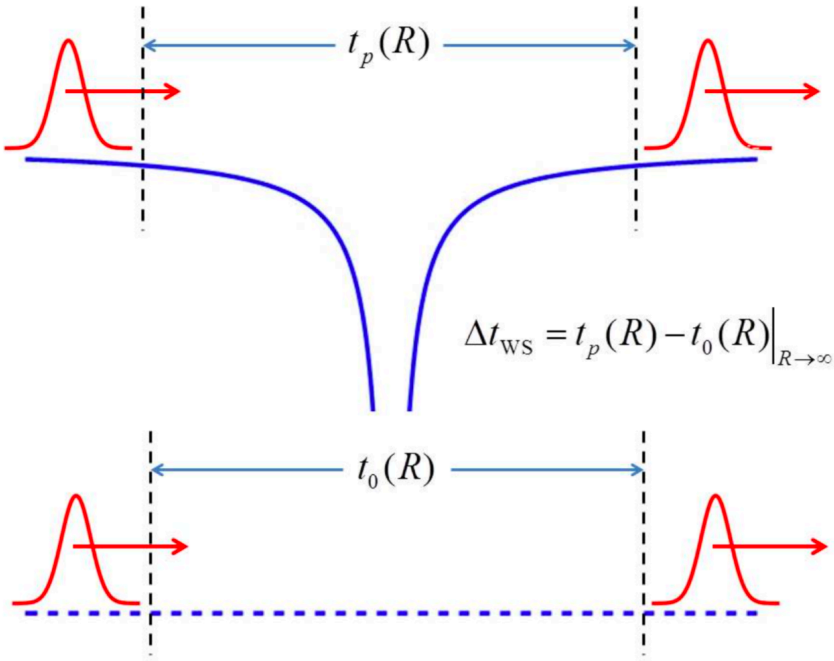

Figure 2.1: Schematic for the WS time delay in scattering, taken from Ref. [16]. The time delay Δt_{WS} is defined as $\Delta t_{\mathrm{WS}} = t_p(R) - t_0(R)|_{R\to\infty}$ [16]. The time $t_p(R)$ is the duration a particle (or wavepacket) spends in a region of space R within the potential (top), and $t_0(R)$ is the duration that the same particle or wavepacket spends in the same region R, but without the presence of the potential, i.e., free particle (bottom), as the region R extends to infinity.

this technique to study temporal dynamics of electrons during XUV photoionization of atoms. The fundamental question posed was whether or not there was a time delay between the photoemission of electrons from different orbitals, specifically in this case of the $2s$ and $2p$ orbitals in a neon atom. In the experiment, two streaking traces (c.f., Fig. 2.2) are recorded simultaneously for emission from the $2s$ and $2p$ orbitals in neon atom. The 200 attosecond pulse used had a central frequency of 100 eV, which is sufficient to ionize an electron from either one of the orbitals. A 4 fs IR pulse is used to "streak" the momentum as described in the previous Chapter.

In comparing the two streaking traces for the ionization of 2s and 2p electrons, a time delay between the two events can be extracted using the frequency resolved optical gating for complete reconstruction of attosecond bursts (FROG-CRAB) algorithm [17]. In the study of Schultze *et al.*, a 21 ± 5 as offset between the two streaking traces was observed (c.f., Fig. 2.2), which has been interpreted as a time delay in the photoemission of the 2p electron with respect to that of the 2s electron. While the work of Schultze *et al.* has not been repeated directly by another attosecond streaking experiment, the $2p-2s$ photoemission time delay in Neon was recently revisited experimentally by Isinger *et al.*, but using the RABBITT technique with an attosecond pulse train [18].

The experiment of Isinger *et al.*, and specifically the interpretation of their results, depends upon being able to achieve sufficient spectral resolution to distinguish between the signals of two processes separated by 7.2 eV, which is on the order of the bandwidth of a typical attosecond pulse (the bandwidth of the attosecond pulse used in Ref. [17] was ~ 14 eV). In order to achieve such standards in resolution, they invoke a method used by Ye and co-workers in Ref. [81]. This method has been demonstrated to circumvent the natural trade-off between temporal and spectral resolution in the visible spectrum by using high-resolution frequency combs based on phase-stable femtosecond pulse trains [81]. In Ref. [18], Isinger *et al.* extended this method to an XUV attosecond pulse train, and they achieved a train of attosecond pulses with harmonic comb teeth of only 1 eV in bandwidth. They used this pulse train in a RABBITT setup (c.f., section 1.3.1.2), and in doing so suggest that the experiment of Schultze *et al.* did not have sufficient spectral resolution

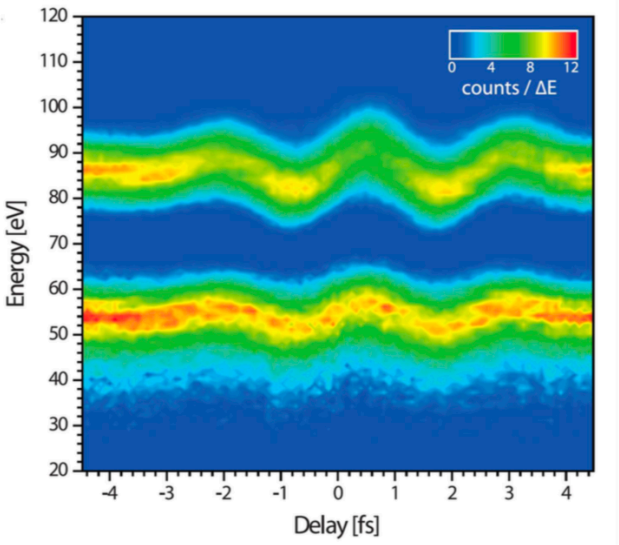

Figure 2.2: The raw attosecond streaking spectrogram data for neon atom from the experiment of Schultze *et al.* shows that the photoelectrons emitted from the $2p$ state (higher energy/top signal) are delayed with respect to those of the $2s$ state (lower energy/bottom signal) as a function of delay between the attosecond XUV and streaking IR pulses. (Captured from [17]).

to disentangle the signal from direct $2s$ ionization and that of the so-called "shake-up" process in which a $2p$ electron is ionized while a second electron is excited to the $3p$ state (c.f., Fig. 2.3 (a)), and that therefore the time delay $\Delta t_{s,\mathrm{expt}}^{(2p,2s)}$ obtained in Ref. [17] was distorted by the overlap of these two signals. Isinger *et al.* show that their resolution is sufficient that they can distinguish between the two sideband oscillation amplitudes, as shown in Fig. 2.3 (b), such that they were also able to obtain the phase (c.f., Fig. 2.3 (c)), and therefore the RABBITT time delays corresponding to these processes, as shown in Fig. 2.4. The authors of Ref. [18] state that the shake-up harmonic oscillates out of phase with the sideband, which causes a sudden drop in the energy-resolved phase. Since the phases due to direct and shake-up contribution can be distinguished in their RABBITT signal, the time delays $\Delta t_{R,\mathrm{expt}}^{(2p,2s)}$ and $\Delta t_{R,\mathrm{expt}}^{(2p,3p_{\mathrm{su}})}$, where $3p_{su}$ refers to the signal resulting from the shake up process, may be obtained. Once being able to eliminate the possibility of contributions from the shake-up pathway, the obtained $\Delta t_{R,\mathrm{expt}}^{(2p,2s)}$ achieved agreement with theoretical calculations implementing many-body perturbation theory [18, 19, 64], as shown in Fig. 2.4.

2.2 Theoretical analysis and interpretation of photoemission time delays

As mentioned in the introduction, in theoretical analysis typically the time delay for emission from one particular orbital is considered, which in the streaking technique is defined as the offset of the streaking curve for emission from one orbital as compared to the streaking of a free electron (or, equivalently, the vector potential, see section 1.3.1.1). This time delay has been widely attributed to the sum of two terms [22, 24, 25, 73], which we refer to as the "sum rule". The first term is the Wigner-Smith delay (2.3), and the second term is due to the coupling of the long-range tail of the Coulomb potential of the residual ion and the streaking laser field upon the propagation of the electron. In this section we review the past work done in justifying this rule.

2.2.1 The sum rule

As a first step, Schultze *et al.* [17] proposed to apply Eq. (2.1) in order to interpret the measured time delay, despite its divergence for Coulomb potentials, which raised concerns from

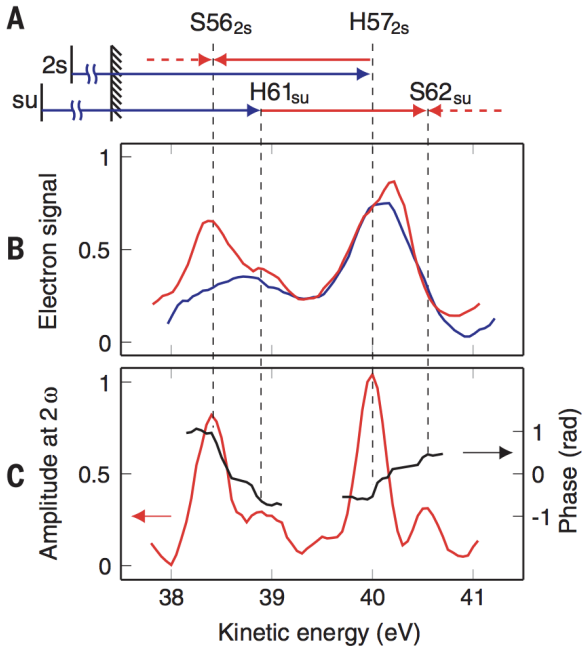

Figure 2.3: (a) Kinetic energy diagram as presented in the work of Isinger *et al.* for direct $2s$ ionization and $2p$ ionization accompanied by $2p \rightarrow 3p$ excitation (shake-up). (b) Photoelectron spectra obtained with XUV only (blue) and XUV + IR (red). (c) Energy-resolved intensity and phase of the two photon oscillation, obtained by Fourier transform of the signal. The symbol H, e.g. H61, corresponds to the direct signal from a high harmonic, where as S, e.g. S56, refers to a sideband signal (Taken from Ref. [18]).

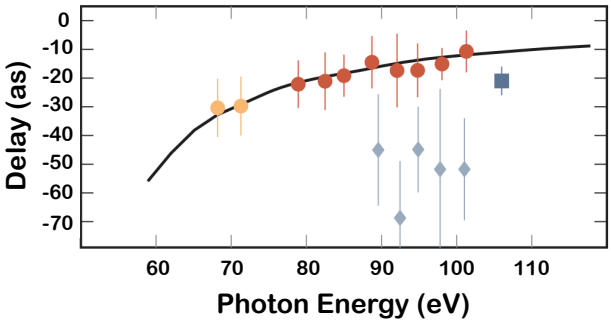

Figure 2.4: Time delay differences $\Delta t_R^{2s} - \Delta t_R^{2p}$ in neon from the experiment in Ref. [18] as a function of photon energy. The yellow and red dots were obtained via two different measurements. Theoretical calculations within many-body perturbation theory [19] agree very well with the experimental data (solid line). The obtained time delay differences $\Delta t_R^{3p_{su}} - \Delta t_R^{2p}$ between shake-up and 2p ionization (diamonds), as well as the time delay obtained in the experiment from Ref. [17] (square), are also shown (Taken from Ref. [18]).

some theorists [73, 82–84]. Nagele *et al.* [73] and Zhang *et al.* [84] discovered independently that the non-divergent WS delay defined by Eq. (2.3) does not account for the streaking delay obtained in calculations alone, unless the potential is very short ranged. In the case of Ref. [73], Nagele *et al.* calculated the streaking trace classically, and they confirmed that indeed the calculated trace shows an offset from the original streaking formula for a free particle, i.e. $\mathbf{k}_f(t_i) \simeq \mathbf{k}_0 - \mathbf{A}_s(t_i)$. Nonetheless, this time offset, or time delay, in general did not agree with the WS time delay. It was then concluded that there is an additional contribution to the streaking delay due to the interplay of the long-range tail of the Coulomb potential and the streaking laser, and we refer to this term throughout the thesis as the "Coulomb-Laser Coupling" Δt_{CLC}.

Inspired by this result, Ivanov *et al.* [85] derived an analytical formula for Δt_{CLC} by using an eikonal approximation-based quantum approach. Within the eikonal approximation, they predicted that the short-range part of the potential also coupled to the streaking field. Therefore, it was proposed that Δt_{CLC} did not only arise from the long-range Coulomb potential, but the short-range part as well, and this short-range contribution was on the order of Δt_{WS}. They then proceeded to use their formula for Δt_{CLC} to calculate $\Delta t_{\mathrm{s}} = \Delta t_{\mathrm{WS}} + \Delta t_{\mathrm{CLC}}$ for both the 2p and 2s photoemission in neon atom, using calculations of Δt_{WS} from Ref. [86], and obtained a time delay of 18 as, which is within the uncertainty of the measured streaking delay of Schultze *et al.* 21 ± 5 as. However, Nagele *et al.* pointed out that the prediction of a short-range contribution to Δt_{CLC} must be incorrect, because for short-range potentials the streaking delay is found to be equal to the WS delay [24]. Therefore, it was concluded that the coupling delay Δt_{CLC} has no relation to the short-range part of the atomic potential, and arises solely from the coupling effect of the streaking field with the long-range tail of the Coulomb potential. In Ref. [24], it was further concluded that because Δt_{CLC} only depends on the long-range Coulomb tail of the potential, it must be the same for all single-electron systems with the same parent ion charge. The streaking delay written as the well known sum rule:

$$\Delta t_s = \Delta t_{\mathrm{WS}} + \Delta t_{\mathrm{CLC}} \tag{2.4}$$

can therefore be obtained for all systems with the same asymptotic behavior as the hydrogen atom, by calculating Δt_{WS} via Eq.(2.3) and calculating $\Delta t_{\mathrm{CLC}} = \Delta t_s - \Delta t_{\mathrm{WS}}$ for the hydrogen atom. It is important to note that the sum rule is supported by numerical streaking simulations and analysis of laser assisted photoionization using perturbation theory (see review [64]). To this end, in Chapter 4, we present an alternative way to justify the sum rule.

In the time since, many publications in the literature have made use of Eq. (2.4) (e.g., [17, 18, 22, 24–26, 29, 64, 73, 85–91]), using the Δt_{CLC} calculations obtained by Nagele *et al.* for hydrogen atom [24] in the manner described above and using Eq. (2.3) for Δt_{WS}. It has been used to theoretically analyze additional effects such as multielectron effects [25,29], the effect of an attochirp [91] and the possibility of a multielectron "shake-up" process [25], however no agreement with the original experiment of [17] was obtained. As we mentioned in section 2.1 though, using the RABBITT technique and the contribution of a shake-up process may explain the disagreement with the original measurement [18].

2.2.2 Classical streaking and the delay as a field-weighted sum

Motivated by studies showing that the streaking delay calculated by TDSE simulations was in good agreement with classical simulations [73], Su and coworkers further analyzed the solution of the Newton equation for the propagation of the photoelectron in the streaking field [92, 93]:

$$\frac{d\mathbf{k}\left(t\right)}{dt} = -\mathbf{E}_s\left(t\right) - \nabla V\left(\mathbf{r}\right), \tag{2.5}$$

where $\mathbf{k}\left(t\right)$ is the momentum of the photoelectron, $\mathbf{E}_s\left(t\right)$ is the streaking field, and $V\left(\mathbf{r}\right)$ is the potential of the residual ion. Considering a linearly polarized field, the simultaneous interaction of the electron with the laser and Coulomb fields takes effect along the direction of the laser polarization, typically chosen as the $z-$axis:

$$\frac{dk_z\left(t\right)}{dt} = -E_s\left(t\right) - \frac{dV}{dz}. \tag{2.6}$$

Su *et al.* then integrated this equation directly to solve for the momentum k_z as $z \to \infty$ (denoted $k_{f,z}$), and set it equal to the $z-$component of the streaking equation Eq. (1.6):

$$k_{f,z}(t_i) = \sqrt{k_{0,z}^2 - 2\int_{t_i}^{T_s} E_s(t)k_z(t)dt} = k_{0,z} - A_s(t_i + \Delta t_s) \tag{2.7}$$

where $k_z(t)$ in the integrand is the $z-$component of the momentum of the electron in the combined streaking field and Coulomb potential, $k_{0,z}$ is the streaking-field-free asymptotic momentum, and t_i is the time of transition into the continuum, which often is assumed to coincide with the peak of the NIR pulse. Note that the top bound of the integral on the left hand side of the equation is set to the duration of the streaking pulse T_s as opposed to ∞, because $E_s(t) = 0$ for $t > T_s$, given that the pulse starts at $t = 0$. Su *et al.* proceeded by making the approximation that one can expand $A_s(t_i + \Delta t_s) \simeq A_s(t_i) + \Delta t_s E_s(t_i)$ for small Δt_s on the right hand side of Eq. (2.7). In addition, they reasoned that the second term under the square root on the left hand side is typically small, and therefore expanded the square root to first order. After these two approximations, they solve for the streaking delay as

$$\Delta t_s \simeq \frac{1}{E_s(t_i)} \int_{t_i}^{T_s} E_s(t) \left[1 - \frac{k_z(t)}{k_{0,z}}\right] dt. \tag{2.8}$$

Su *et al.* then made this equation more instructive by further rewriting this equation as a discrete sum via assuming that the streaking field and electron momentum are approximately constant in the time interval $[t_j, t_j + \delta t]$, i.e. $E_s(t) \simeq E_s(t_j)$ and $k_z(t) \simeq k_z(t_j)$, to get:

$$\Delta t_s \simeq \frac{1}{E_s(t_i)} \sum_{j=1}^{N} E_s(t_j) \left[1 - \frac{k_z(t_j)}{k_0}\right] \delta t \tag{2.9}$$

$$= \sum_{j=1}^{N} \frac{E_s(t_j)}{E_s(t_i)} \Delta t_{\text{field-free}}^{(j)}. \tag{2.10}$$

In this equation, $\Delta t_{\text{field-free}}^{(j)}$ is the piecewise field-free time delay that the electron accumulates during its propagation in the time interval $[t_j, t_j + \delta t]$ and over the related finite region $[z_j, z_j + \delta z]$ of the potential $V(\mathbf{r})$ without the laser field as compared to the propagation of a free particle over the same distance in space. This formula provided an interesting interpretation of the streaking delay which we will refer to throughout this thesis. That is, the streaking delay can be viewed as

a sum of piecewise field-free time delays weighted by the streaking field strength present as the electron wavepacket propagates over the corresponding part of the potential. In Chapter 4, we will show, by extending this interpretation to a quantum mechanical picture, under which conditions this formula can be further approximated by the sum rule.

A critical note is that per our discussions in sections 2.2.1 and 2.2.2, we see that it has been determined in two different formalisms that, for one photon ionization, the streaking delay is solely accumulated during propagation of the photoelectron in the continuum [20]. For this reason we refer to the streaking delay Δt_s in the context of one-photon ionization as the "continuum delay" Δt_c.

2.3 The absorption delay in two-photon ionization

In the previous section, we discussed the status of the theoretical analysis for the attosecond streaking of one-photon ionization. In this section we discuss past work going beyond the one-photon absorption, where in some of these scenarios it has been shown that neither the sum rule nor Eq. (2.8) is sufficient to account for the streaking time delay in theoretical calculations. For example in resonant two-photon ionization, once accounting for both the WS and CLC time delays, an additional delay, which is dependent upon the properties of the ionizing pulse, can be observed in the attosecond streaking of resonant two-photon processes. This was discovered by Su and coworkers in their comparison of streaking delays in one- and two-photon non-resonant ionization vs. resonant two-photon ionization [20], and independently by Martín and coworkers [80] when studying RABBITT (c.f., 1.3.1.2) through a Fano resonance embedded in the continuum.

In the work of Ref. [20] it was shown that the streaking delay for resonant two-photon ionization could be expressed as

$$\Delta t_s = \Delta t_{abs} + \Delta t_c, \tag{2.11}$$

where Δt_c is the "continuum delay" discussed at the conclusion of the last section. The additional absorption time delay Δt_{abs} was found to be zero for one-photon as well as non-resonant two-

photon transitions. Additionally as shown in Fig. 2.5, the streaking delay resulting from resonant two-photon ionization shows a strong, linear dependence upon the pulse duration of the ionizing pulse, whereas the same dependence is not seen for the streaking delays corresponding to one-photon and non-resonant two-photon ionization. In order to obtain the absorption time delay, Su *et al.* show that it is possible to obtain the contribution using the continuum delay Δt_c in two ways. One can either calculate Δt_c via a classical analysis, or using the streaking delay for the one-photon process of the same final kinetic energy as the two-photon process. The latter can be used because by definition, the streaking delay and continuum delay are equivalent ($\Delta t_s = \Delta t_c$) for one-photon ionization. The absorption delay Δt_{abs} is then calculated via an equivalent form of Eq. (2.11):

$$\Delta t_{\text{abs}} = \Delta t_s^{(2\omega)} - \Delta t_c, \tag{2.12}$$

where we use $\Delta t_s^{(2\omega)}$ to denote the streaking delay for the two-photon process.

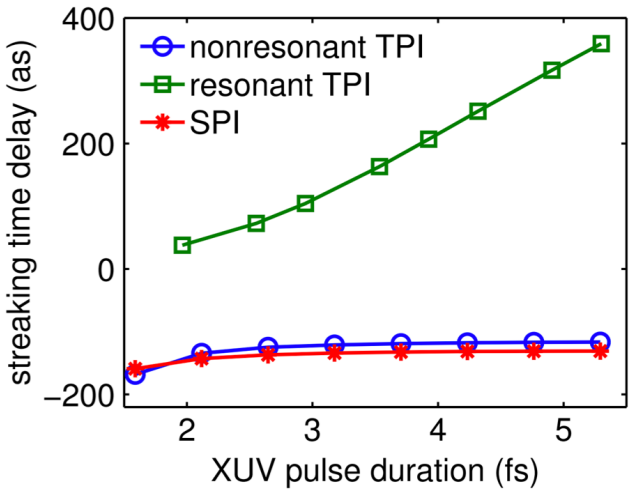

Figure 2.5: (a) Streaking time delay simulations from Su *et al.* [20] as a function of XUV pulse duration for 3D helium atom. Three ionization processes are considered: non-resonant two-photon ionization (TPI) (blue lines with circles), resonant TPI (green lines with squares), and single photon ionization (SPI) (red lines with asterisks). (Taken from Ref. [20]).

Around the same time, Martín and coworkers [80] found via TDSE simulations that in a RABBITT setup as a harmonic traverses a resonance, both the phase shift and frequency of the

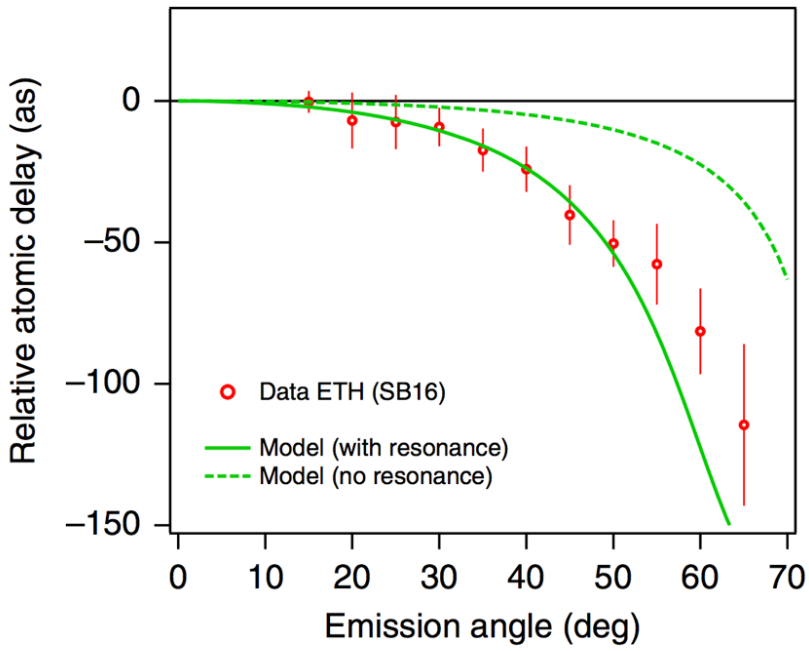

Figure 2.6: Angular-resolved time delays from Ref. [21]. The measured atomic time delay (red symbols) is shown as a function of electron emission angle for SB16. The green lines show the calculated values in resonant (solid) and non-resonant (dashed) conditions. The error bars indicate the standard deviation of the measurements. (Taken from Ref. [21])

sideband beating significantly varies with photon energy. They additionally showed that the sideband signals persist even when the pump and probe pulses do not overlap, which is contrary to the findings of non-resonant RABBITT. Further studies were done, resulting in the conclusion that there must be an additional delay when traversing through a resonance. Argenti along with Martín and others [67] parameterized the RABBITT delay for resonant two-photon transitions as the sum of the time delay from the non-resonant process, plus an additional delay resulting from the resonance. Thus, they independently deduced from their results a similar conclusion as Su *et al.* for the resonant two-photon ionization process. A year later, Cirelli *et al.* were able to measure the angle-resolved RABBITT time delay of argon experimentally in the vicinity of the $3s^{-1}np$ autoionizing resonances, and found that the presence of the resonance affected the angular dependence of the RABBITT delay [21]. Using a theoretical model based on the work of [67], the authors were able to confirm this interpretation, and therefore the existence of the additional absorption delay predicted by Argenti *et al.* This is demonstrated in Fig. 2.6, where the time delays predicted by the model both with and without inclusion of the resonance are compared as a function of angle. It is clear in the figure that the experimental data are in better agreement with the theoretical prediction when including the resonant term. This additional delay in RABBITT measurements is not the focus of this thesis, however it is analogous to the absorption delay in attosecond streaking discussed above.

Chapter 3

Methods for solving the time-dependent Schrödinger equation

Within this thesis, we study the interaction of ultrashort laser pulses with either one-electron systems like hydrogen atom and H_2^+, or multielectron systems approximated by single active electron (SAE) potentials (c.f., section 3.1.4). Therefore, we need to solve the time-dependent Schrödinger equation (TDSE) for a single-electron wavefunction $\Psi(\mathbf{r},t)$. The TDSE is expressed as

$$i\frac{\partial\Psi(\mathbf{r},t)}{\partial t} = \left(\hat{H}_0(\mathbf{r}) + \hat{V}_I(\mathbf{r},t)\right)\Psi(\mathbf{r},t), \tag{3.1}$$

where $\mathbf{r}$ is the position of the electron, $\hat{H}_0$ is the field-free (time-independent) Hamiltonian of the system, $\hat{V}_I$ describes the interaction of the system with the laser field, and the total Hamiltonian is therefore given by $\hat{H}(\mathbf{r},t) = \hat{H}_0(\mathbf{r}) + \hat{V}_I(\mathbf{r},t)$. The goal is to determine $\Psi(\mathbf{r},t)$ throughout the time of the simulation, given an initial condition. There exist few examples where Eq. (3.1) may be solved accurately via analytical methods. It is common to, when appropriate, use approximations like perturbation theory. These approximations can simplify the problem sufficiently in order to gain insight via analytical expressions. For the interaction with an intense laser pulse, when the exact solution is needed, we must turn to numerical solvers.

In this Chapter, we review the analytical and numerical techniques relevant to calculating observables in the interaction of a system with an attosecond pulse and/or a femtosecond (mid-infrared) laser pulse. In the first section 3.1, we discuss the analytical formulation of both field and matter, as well as their interaction within both a classical and semi-classical framework. We also show specific methods for analytically modeling the dynamics of the interaction, including

time-dependent perturbation theory, single active electron potentials, the partial-wave expansion of scattering theory, and the classical Newton equation describing the motion of the electron in an electromagnetic field. In section 3.2, we describe our methods for solving Eq. (3.1) numerically on a finite grid. Lastly, we conclude with a discussion regarding how to obtain time delays in numerical simulations of attosecond streaking in section 3.3.

3.1 Semi-classical formulation of the interaction between field and matter

In order to write down $\hat{V}_I$ in Eq. (3.1), we need to describe the electromagnetic field interacting with the atom or molecule of interest. In general throughout this thesis, we will assume that the field can be described classically by an electric field $\mathbf{E}(\mathbf{r},t)$ and a magnetic field $\mathbf{B}(\mathbf{r},t)$, which satisfy Maxwell's equations (without sources):

$$\begin{aligned} \nabla\cdot\mathbf{E} &= 0, \\ \nabla\cdot\mathbf{B} &= 0, \\ \nabla\times\mathbf{E} &= -\frac{\partial\mathbf{B}}{\partial t}, \\ \nabla\times\mathbf{B} &= \frac{1}{c^2}\frac{\partial\mathbf{E}}{\partial t}, \end{aligned} \tag{3.2}$$

where c is the speed of light in vacuum. We can generate the fields $\mathbf{E}$ and $\mathbf{B}$ via the use of scalar and vector potentials $\phi(\mathbf{r},t)$ and $\mathbf{A}(\mathbf{r},t)$ respectively by

$$\mathbf{E} = \nabla\phi - \frac{1}{c}\frac{\partial\mathbf{A}}{\partial t} \tag{3.3}$$

$$\mathbf{B} = \nabla\times\mathbf{A}. \tag{3.4}$$

Since only the fields $\mathbf{E}$ and $\mathbf{B}$ have a unique physical significance as opposed to the potentials, Maxwell's equations (3.2) must be gauge invariant with respect to the scalar and vector potentials (for arbitrary real, differentiable function $f(\mathbf{r},t)$):

$$\mathbf{A} \rightarrow \mathbf{A}' = \mathbf{A} + \nabla f, \tag{3.5}$$

$$\phi \rightarrow \phi' = \phi - \frac{\partial f}{\partial t}. \tag{3.6}$$

As a general statement, in this thesis we use the radiation, or Coulomb gauge, which is defned by the condition

$$\nabla \cdot \mathbf{A} = 0. \tag{3.7}$$

This gauge is typically chosen when no sources are present, implying that $\phi = 0$ and

$$\mathbf{E} = -\frac{1}{c}\frac{\partial \mathbf{A}}{\partial t} \tag{3.8}$$

$$\mathbf{B} = \nabla \times \mathbf{A}. \tag{3.9}$$

For a finite laser pulse, the solution of Eq. (3.2) is given by a superposition of monochromatic plane waves with the appropriate amplitudes, frequencies and phases. In the case where each plane wave component propagates in the same direction $\hat{\mathbf{k}}_{\mathrm{L}}$ in a field with linear polarization direction $\hat{\epsilon}$, the vector potential in the Coulomb gauge can be written as [94]

$$\mathbf{A}(\mathbf{r}, t) = \hat{\epsilon} \int_0^\infty A_0(\omega) \sin\left(\mathbf{k}_{\mathrm{L}} \cdot \mathbf{r} - \omega t - \phi_{\mathrm{CEP}}(\omega)\right) d\omega, \tag{3.10}$$

where $\phi_{\mathrm{CEP}}(\omega)$ is the carrier envelope phase associated with the angular frequency ω and propagation vector $\mathbf{k}_{\mathrm{L}} = (\omega/c)\,\hat{\mathbf{k}}_{\mathrm{L}}$. The corresponding electric field is then

$$\mathbf{E}(\mathbf{r}, t) = \hat{\epsilon} \int_0^\infty E_0(\omega) \cos\left(\mathbf{k}_{\mathrm{L}} \cdot \mathbf{r} - \omega t - \phi_{\mathrm{CEP}}(\omega)\right) d\omega, \tag{3.11}$$

with $E_0(\omega) = \frac{\omega}{c} A_0(\omega)$. In general, these fields may be written as the product of a carrier wave and an envelope function $\mathcal{E}_0(t, \mathbf{k}_{\mathrm{L}}, \mathbf{r}, T)$ with pulse duration $T = \frac{2\pi N}{\omega}$ for an N-cycle pulse along a polarization direction $\hat{\epsilon}$, such that

$$\mathbf{E}(\mathbf{r}, t) = \hat{\epsilon} E_0 \mathcal{E}_0(t, \mathbf{k}_L, \mathbf{r}, T) \cos\left(\omega t - \mathbf{k}_L \cdot \mathbf{r} + \phi_{\mathrm{CEP}}\right). \tag{3.12}$$

It follows that a laser pulse of arbitrary polarization with ellipticity parameter ξ can be readily described in a similar manner. For two orthogonal unit basis vectors $\hat{\epsilon}_1$ and $\hat{\epsilon}_2$ (each mutually orthogonal to $\hat{\mathbf{k}}_{\mathrm{L}}$), the electric field is now [94]

$$\begin{aligned} \mathbf{E}(\mathbf{r}, t) = & \frac{E_0 \mathcal{E}_0(t, \mathbf{k}_{\mathrm{L}}, \mathbf{r}, T)}{\sqrt{1+\xi^2}} \left[\hat{\epsilon}_1 \cos\left(\omega t - \mathbf{k}_{\mathrm{L}} \cdot \mathbf{r} + \phi_{\mathrm{CEP}}(\omega)\right)\right. \\ & \left. -\xi \hat{\epsilon}_2 \sin\left(\omega t - \mathbf{k}_{\mathrm{L}} \cdot \mathbf{r} + \phi_{\mathrm{CEP}}(\omega)\right)\right]. \end{aligned} \tag{3.13}$$

Note that linearly polarized fields can be recovered from Eq. (3.13) via setting ellipticity to zero.

A further simplification can be made, as the dependence of the field upon the spatial coordinate $\mathbf{r}$ may be neglected by invoking the so-called dipole approximation, which states that because the size of the atom (on the order of $1\text{Å} = 10^{-10}$ m) is much smaller than the wavelength of the radiation, we may assume that the electron experiences approximately the same field in all space relevant for the interaction. This approximation consists of neglecting the "retardation effect" due to the wave vector $\mathbf{k}$ [95]. Thus, we take only the first term in the expansion of the spatial modulation factor

$$e^{i\mathbf{k}\cdot\mathbf{r}} \simeq 1 + \mathbf{k}\cdot\mathbf{r} + ..., \tag{3.14}$$

namely unity. Therefore the field in Eq. (3.13) becomes

$$\mathbf{E}(t) = \frac{E_0 \mathcal{E}_0(t,T)}{\sqrt{1+\xi^2}} \left[\hat{\epsilon}_1 \cos(\omega t + \phi_{CEP}) - \xi\hat{\epsilon}_2 \sin(\omega t + \phi_{CEP})\right], . \tag{3.15}$$

All of the electric fields used in this thesis are of this form.

3.1.1 Classical electron dynamics in a laser field

In various scenarios, especially those where an electron is in the continuum, it has been shown that certain aspects of its dynamics can be described classically. We therefore begin by writing down the classical Hamiltonian for an electron in a radiation field without the influence of any other potentials:

$$H(t) = \frac{1}{2}\left(\mathbf{p} - \frac{1}{c}\mathbf{A}(t)\right)^2 \tag{3.16}$$

If we compare this Hamiltonian to that of the motion of a free electron, we see that the momentum $\mathbf{p}$ has been replaced with $\mathbf{p} - \mathbf{A}/c$. This can be justified through the use of the Hamilton equations, which leads to the Lorentz equation governing the classical, non-relativistic dynamics of a free electron (of charge $q = -e = -1$) in a laser field as

$$\frac{d\mathbf{p}}{dt} = -\left[\mathbf{E}(\mathbf{r},t) + \mathbf{p}\times\mathbf{B}(\mathbf{r},t)\right]. \tag{3.17}$$

In photoemission however, the electron is leaving an atomic potential $V(\mathbf{r})$, and we must include this potential in the Newton equation to fully describe the classical dynamics of a photoelectron

propagating away from a Coulomb potential. Furthermore, the magnitudes of the magnetic and electric fields are related by the relation $|\mathbf{B}| = |\mathbf{E}|/c$, and for the intensities of the electric fields used in this thesis, this relation implies that $|\mathbf{B}| << |\mathbf{E}|$. Therefore, we can neglect the contribution of the magnetic field to the force, and one has

$$\frac{d\mathbf{p}}{dt} = -\mathbf{E}(\mathbf{r},t) - \nabla V(\mathbf{r}). \tag{3.18}$$

It is common to gain insights in the interpretation of streaking measurements, and to complement quantum simulations, by using classical analysis of the electron dynamics in the continuum based on Eq. (3.18). For streaking simulations in particular, we may sample initial conditions for the solution of Eq. (3.18) in Monte Carlo calculations, which will be described further in Chapter 5.

3.1.2 Semi-classical dynamics

In order to describe the dynamics quantum mechanically, we perform the usual prescription for converting classical quantities to quantum operators, and obtain the semiclassical Schrödinger equation:

$$\begin{aligned} i\frac{\partial\Psi(\mathbf{r},t)}{\partial t} &= \left[\frac{\left(-i\nabla - \frac{1}{c}\mathbf{A}\right)^2}{2} + V(\mathbf{r},t)\right]\Psi(\mathbf{r},t) \\ &\equiv \left[\hat{H}_0 + \hat{V}_I\right]\Psi(\mathbf{r},t), \end{aligned} \tag{3.19}$$

which identifies the semiclassical electron-field interaction Hamiltonian

$$\hat{V}_I(\mathbf{r},t) = \frac{1}{c}\left[2i\mathbf{A}(\mathbf{r},t)\cdot\nabla + i\nabla\cdot\mathbf{A}(\mathbf{r},t)\right] + \frac{1}{2c^2}\mathbf{A}^2(\mathbf{r},t), \tag{3.20}$$

and the field-free part of the Hamiltonian is

$$\hat{H}_0 = -\frac{\nabla^2}{2} + V(\mathbf{r}). \tag{3.21}$$

In Eq. (3.20), the $i\nabla\cdot\mathbf{A}$ term vanishes by definition of the Coulomb gauge, and therefore Eq. (3.19) becomes

$$i\frac{\partial\Psi(\mathbf{r},t)}{\partial t} = \left[-\frac{\nabla^2}{2} + \frac{i}{c}\mathbf{A}(t)\cdot\nabla + \frac{1}{2c^2}\mathbf{A}^2(t) + V(\mathbf{r})\right]\Psi(\mathbf{r},t) \tag{3.22}$$

which is known as the "velocity gauge" form of the TDSE. Under dipole approximation, we may make the gauge transformation

$$\Psi(\mathbf{r},t) = e^{(i/c)\mathbf{r}\cdot\mathbf{A}(t)}\psi(\mathbf{r},t), \tag{3.23}$$

and upon substitution into the TDSE (3.22) and using the definition of the electric field ($\mathbf{E}(t) = -\frac{1}{c}\frac{\partial \mathbf{A}(t)}{\partial t}$), we get the so-called "length gauge" form of the TDSE:

$$i\frac{\partial\psi(\mathbf{r},t)}{\partial t} = \left[-\frac{\nabla^2}{2} + V(\mathbf{r}) - \mathbf{r}\cdot\mathbf{E}(t)\right]\psi(\mathbf{r},t). \tag{3.24}$$

Gauge invariance, by definition, implies that using either gauge in our calculations should give the same results. However, in numerical simulations, the use of either gauge comes with a set of advantages and disadvantages, and so the choice of gauge can become important, depending on the problem being solved numerically. This will be further discussed in the following section, however for the moment, we choose the length gauge without loss of generality.

The solutions to Eq. (3.1) are, in general, not guaranteed to have analytical forms, and must be determined numerically. However, under certain approximations and in some specific cases, the equation can be resolved analytically. One such approximation method is the so-called perturbation theory, which becomes applicable when the field is sufficiently weak as compared to the binding Coulomb potential.

3.1.3 Time-dependent perturbation theory

3.1.3.1 Time-evolution operator

In general, it is assumed that we know the state of our system at a given time t_0, and wish to determine its state at a later time t. Therefore, the problem is determining the unitary time-evolution operator $U(t,t_0)$. As its name implies, this operator describes the evolution of the state of the system in time in the Schrödinger representation. The evolution operator is completely determined by the Hamiltonian $\hat{H}(t)$, and is defined by the integral equation

$$\hat{U}(t,t_0) = \hat{1} - i\int_{t_0}^{t}\hat{H}(t_1)\,\hat{U}(t_1,t_0)\,dt_1 \tag{3.25}$$

and the initial condition $\hat{U}(t_0, t_0) = 1$. Due to the fact that $\hat{H}(t)$ is Hermitian, $\hat{U}(t, t_0)$ is unitary, and therefore

$$\hat{U}^{\dagger}(t, t_1) = \hat{U}(t_1, t). \tag{3.26}$$

From this we get the equivalent definition of

$$\hat{U}(t, t_0) = \hat{1} - i \int_{t_0}^{t} \hat{U}(t, t_1)\, \hat{H}(t_1)\, dt_1. \tag{3.27}$$

having replaced the evolution operator in Eq. (3.25) by its Hermitian conjugate and used Eq. (3.26).

Let us define the time-evolution operator for the field-free problem as $\hat{U}_0(t, t_0)$, which corresponds to $\hat{H}_0$ via a Schrödinger-like equation:

$$i\frac{\partial \hat{U}_0(t, t_0)}{\partial t} = \hat{H}_0 \hat{U}_0(t, t_0), \qquad \hat{U}_0(t_0, t_0) = 1. \tag{3.28}$$

Assuming that $\hat{U}_0(t, t_0)$ is known, we may determine $\hat{U}$ if we can form the unitary operator

$$\hat{U}_I(t, t_0) = \hat{U}_0^{\dagger}(t, t_0)\, \hat{U}(t, t_0), \tag{3.29}$$

which is the evolution operator in the interaction representation. Furthermore, it can be shown [72] that the time dependence of $\hat{U}_I$ is determined by the Hamiltonian

$$\hat{V}_I'(t) \equiv \hat{U}_0^{\dagger}(t, t_0)\, \hat{V}_I(t)\, \hat{U}_0(t, t_0). \tag{3.30}$$

Equivalently, $\hat{U}_I(t, t_0)$ is defined by

$$\hat{U}_I(t, t_0) = \hat{1} - i \int_{t_0}^{t} \hat{V}_I'(t_1)\, \hat{U}_I(t_1, t_0)\, dt_1. \tag{3.31}$$

The solutions to the integral equations (3.31) and (3.25) may be obtained formally via iteration, i.e. substituting $1 - i\int_{t_0}^{t_2} \hat{V}_I'(t_2)\, \hat{U}_I(t_2, t_0)\, dt_2$ for $\hat{U}_I(t_1, t_0)$ in the right hand side of Eq. (3.31), we get

$$\hat{U}_I(t, t_0) = \hat{1} - i \int_{t_0}^{t} \hat{V}_I'(t_1)\, dt_1 + (-i)^2 \int_{t_0}^{t} \int_{t_0}^{t_1} \hat{V}_I'(t_1)\, \hat{V}_I'(t_2)\, \hat{U}(t_2, t_0)\, dt_2 dt_1. \tag{3.32}$$

Continuing in this manner, defining

$$\hat{U}_I^{(n)} \equiv (-i)^n \int_{t > t_n > t_{n-1} > \ldots > t_1 > t_0} \hat{V}_I'(t_n)\, \hat{V}_I'(t_{n-1}) \ldots \hat{V}_I'(t_1)\, dt_n\, dt_{n-1} \ldots dt_1, \tag{3.33}$$

and using Eqs. (3.29) and (3.30), we get the following expansion for $\hat{U}$:

$$\hat{U}(t,t_0) = \hat{U}_0(t,t_0) + \sum_{n=1}^{\infty} \hat{U}_n(t,t_0), \tag{3.34}$$

where

$$\begin{aligned} \hat{U}_n(t,t_0) \equiv (-i)^n \int_{t>t_n>t_{n-1}>\ldots>t_1>t_0} & \hat{U}_0(t,t_n)\,\hat{V}_I(t_n)\,\hat{U}_0(t_n,t_{n-1})\,\hat{V}_I(t_{n-1})\ldots \\ & \ldots\hat{U}_0(t_2,t_1)\,\hat{V}_I(t_1)\,\hat{U}_0(t_1,t_0)\,dt_n\,dt_{n-1}\ldots dt_1. \end{aligned} \tag{3.35}$$

It is clear, since Eq. (3.34) is an infinte sum, that approximations are needed if we wish to proceed. In the case that the interaction term $\hat{V}_I(t)$ (in our case, the interaction of the laser with the system) is weak compared to the field-free Hamiltonian $\hat{H}_0$ (the atomic or molecular potential), we may truncate the power series (3.34) to a given order.

3.1.3.2 Transition amplitudes and lowest-order perturbation theory

The method of the previous section is particularly applicable in cases where $\hat{H}_0$ is time-independent, such as for a bound state of an atom or molecule. In addition, we assume that the solutions for this Hamiltonian are known. The evolution operator $\hat{U}_0$ is then

$$\hat{U}_0(t,t_1) = e^{-i\hat{H}_0(t-t_1)}. \tag{3.36}$$

At this point, we also introduce the notation

$$\omega_{mn} = E_m - E_n \tag{3.37}$$

$$V_{mn} = \langle m | V_I(t) | n \rangle, \tag{3.38}$$

where states $|m\rangle$ and $|n\rangle$ are eigenstates of $\hat{H}_0$ with energies E_m and E_n.

We assume that the system is in an eigenstate $|a\rangle$ of $\hat{H}_0$ at some initial time t_0. The goal is to calculate the amplitudes whose square moduli are the time-dependent probabilities of measuring the system in any bound state of $\hat{H}_0$. Such an amplitude can be expressed as

$$c_{ba} = \left\langle b \left| \hat{U}(t,t_0) \right| a \right\rangle. \tag{3.39}$$

If we substitute the expansion Eq. (3.34) for the time evolution operator, we get

$$c_{ba} = \sum_{n=1}^{\infty} c_{ba}^{(n)} = \sum_{n=1}^{\infty} \left\langle b \left| \hat{U}_n \right| a \right\rangle . \tag{3.40}$$

We can then write the successive contributions to the amplitude, e.g. the first order contribution is

$$\begin{aligned} c_{ba}^{(1)}(t) &= -i \int_{t_0}^{t} e^{-iE_b(t-t_1)} V_{ba}(t_1)\, e^{-iE_a(t_1-t_0)} dt_1 \\ &= -i \int_{t_0}^{t} e^{i\omega_{ba} t_1} V_{ba}(t_1)\, dt_1, \end{aligned} \tag{3.41}$$

and the second-order contribution is

$$c_{ba}^{(2)}(t) = -\sum\!\!\!\!\!\!\int_m \int_{t_0}^{t} \int_{t_0}^{t_1} V_{bm}(t_2)\, e^{i\omega_{bm} t_2} V_{ma}(t_1)\, e^{i\omega_{ma} t_1} dt_1 dt_2, \tag{3.42}$$

where the sum with integral represents a sum over both discrete and continuous eigenstates of $\hat{H}_0$.

Now we are prepared to consider the dynamics induced by a laser field, which is the case relevant for this thesis. Let us consider a linearly polarized pulse with field strength E_0 and arbitrary envelope $\mathcal{E}_0(t,T)$ of pulse durartion T, given by [94]

$$\mathbf{E}(t) = \hat{\epsilon} E_0 \mathcal{E}_0(t,T) \cos(\omega t + \phi_{\mathrm{CEP}}), \tag{3.43}$$

and the corresponding interaction Hamiltonian is given in the length gauge by

$$\hat{V}_I(t) = -\frac{E_0 \mathcal{E}_0(t,T)}{2} \left[e^{i(\omega t+\phi)} + e^{-i(\omega t+\phi)} \right] \left(\hat{\epsilon} \cdot \hat{\mathbf{d}} \right), \tag{3.44}$$

where $\mathbf{d} = -\mathbf{r}$ is the electric dipole moment operator for the system. At this point it is also useful to introduce the transition dipole matrix element as

$$\mu_{ji} = \langle j | \hat{\epsilon} \cdot \mathbf{d} | i \rangle . \tag{3.45}$$

We then get, to first order in the perturbation

$$c_{fi}^{(1)}(t) = \frac{i \mu_{fi} E_0}{2} \int_{-\infty}^{t} \mathcal{E}_0(t_1,T) \left(e^{i(\omega_{fi}+\omega)t_1} e^{i\phi_{\mathrm{CEP}}} + e^{i(\omega_{fi}-\omega)t_1} e^{-i\phi_{\mathrm{CEP}}} \right) dt_1, \tag{3.46}$$

and for nth order

$$
\begin{aligned}
c_{fi}^{(n)}(t) &= \left(\frac{iE_0}{2}\right)^n \sum_{m_1}\sum_{m_2}\cdots\sum_{m_{n-1}} \mu_{fm_1}\mu_{m_1m_2}\cdots\mu_{m_{n-1}i} \\
&\times \int_{-\infty}^{t} dt_1 \;\; \mathcal{E}_0(t_1,T)\left\{e^{i\left[(\omega+\omega_{fm_1})t_1+\phi_{\text{CEP}}\right]} + e^{-i\left[(\omega-\omega_{fm_1})t_1+\phi_{\text{CEP}}\right]}\right\} \\
&\times \int_{-\infty}^{t_1} dt_2 \;\; \mathcal{E}_0(t_2,T)\left\{e^{i\left((\omega+\omega_{m_1m_2})t_2+\phi_{\text{CEP}}\right)} + e^{-i\left[(\omega-\omega_{m_1m_2})t_2+\phi_{\text{CEP}}\right]}\right\} \\
&\times \;\; ... \;\; \times \int_{-\infty}^{t_{n-1}} dt_n \;\; \mathcal{E}_0(t_n,T)\left\{e^{i\left[(\omega+\omega_{m_{n-1}i})t_n+\phi_{\text{CEP}}\right]} + e^{-i\left[(\omega-\omega_{m_{n-1}i})t_n+\phi_{\text{CEP}}\right]}\right\}.
\end{aligned}
\tag{3.47}
$$

Note that the integral in Eq. (3.46) has two dominant contributions at $\omega_{fi}+\omega=0$ and $\omega_{fi}-\omega=0$ (most easily seen in the case of a continuous wave field, i.e., $\mathcal{E}_0(t,T)=1$ [94]), and these correspond to stimulated emission and absorption of a photon, respectfully. Thus, for example, one photon ionization may be modeled with first order time-dependent perturbation theory by neglecting the stimulated emission term and considering the first order transition of a bound state to a continuum state. This process can be extended out to nth order to describe n-photon processes in the perturbative regime (see Eq. (3.47)), and we will use it to model two-photon ionization in Chapter 5.

3.1.4 Single Active Electron potentials

When studying a system with two or more electrons, the full numerical solution of the TDSE becomes impractical. For processes in which the intense laser field predominantly interacts with one electron only, it is useful to invoke single active electron (SAE) potentials which model the behavior of the multielectron potential from the perspective of one of the electrons, thus reducing the problem to a one-electron TDSE like Eq. (3.1). SAE potentials are commonly obtained through the use of density functional theory, and are often fit to analytical forms for ease of use and potential physical interpretation [96]. The SAE potentials used in this thesis are those demonstrated in the work of Tong and Lin [97], which are expressed as

$$
V(r) = -\frac{Z_c + a_1 e^{-a_2 r} + a_3 r e^{-a_4 r} + a_5 e^{-a_6 r}}{r}. \tag{3.48}
$$

The first term in this potential, $-Z_c/r$ is the Coulomb tail seen at large r, the two Yukawa terms and the exponential term describe the short-range interaction, and the a_i's are obtained by fitting to the numerical potential calculated from self-interaction free density functional theory (for details, see Ref. [96]). We will see in Chapter 4 that such a form for the potential is convenient in determining streaking time delays analytically.

3.1.5 The scattering phase and the WS time delay

The Wigner-Smith delay is most popularly displayed as the energy derivative of the asymptotic scattering phase for a given partial wave l (c.f., Eq. (2.1)). In the analytical method presented in Chapter 4, we will need to obtain the scattering phase shifts in order to take their derivatives directly. For this reason, we briefly review the origin of the scattering phase shifts. In general, a scattering process may be simply described as the interaction between an incident scatterer and a target. As the scatterer approaches the scattering center its wavefunction is modified, and the usual task is determining how and why it is modified by the particular potential of the target. Photoionization can be considered as a half-scattering process [22], and thus observables in formal (full-)scattering theory become useful in describing the propagation of the electron as it leaves its parent ion, the primary observable being the cross-section $\sigma(\Omega)$. The cross-section represents the flux of the outgoing scattered wavefunction as a function of the solid angle Ω, and as we will see, is closely related to the scattering phase.

First, we limit ourselves to the discussion of elastic scattering of electrons by short-range, central potentials $V(r)$ which approach zero asymptotically faster than $1/r$, and we will then discuss the special case of the Coulomb potential afterwards. In a typical scattering process it is required that the observation method is made sufficiently far away such that the wave propagation detected is unaffected by the presence of the scattering center. At such distances, the stationary scattering state solution to the Schrödinger equation consists of three components: a plane wave of definite linear momentum propagating towards the target, a wave that corresponds to transmission through the target without scattering, and lastly a scattered wave [98]. The first term can be

simply expressed asymptotically as a plane wave with definite linear momentum. This is also the same asymptotic form of the second term, with the same momentum, as it is merely a continuation of the incoming wave. At large distances, the scattered wavefunction has the form of an outgoing spherical wave with an amplitude that varies with solid angle. Therefore, if E is the energy and $\mathbf{k}$ is the initial momentum of the particle, we can relate the cross section to the solution of the time-independent Schrödinger equation

$$\left(-\frac{\nabla^2}{2} + V(\mathbf{r})\right)\psi_{\mathbf{k}}(\mathbf{r}) = E\psi_{\mathbf{k}}(\mathbf{r}), \tag{3.49}$$

whose asymptotic behavior at $r \to \infty$ is of the form

$$\psi_{\mathbf{k}}(\mathbf{r})|_{r\to\infty} \simeq e^{i\mathbf{k}\cdot\mathbf{r}} + f(\Omega)\frac{e^{ikr}}{r} \tag{3.50}$$

where $f(\Omega)$ is the scattering amplitude as a function of solid angle Ω. The square modulus of the scattering amplitude gives the cross section for the process, and as we will show next, contains the information essential in determining the phase shifts [72].

We are mainly considering central potentials in this thesis, and therefore the direction of the incident wave vector $\mathbf{k}$ is an axis of rotational symmetry such that if it is taken as the polar axis, the wavefunction and the scattering amplitude are not dependent upon the azimuthal angle ϕ. We therefore decompose the solution in terms of partial waves by expanding in Legendre polynomials;

$$\psi_k(r,\theta) = \sum_l \frac{y_l(r)}{r} P_l(\cos\theta) \tag{3.51}$$

$$f(\Omega) = f(\theta) = \sum_l f_l P_l(\cos\theta) \tag{3.52}$$

where y_l is a solution of the radial equation

$$\left[\frac{d^2}{dr^2} + \left(2(E - V(r)) - \frac{l(l+1)}{r^2}\right)\right] y_l(r) = 0 \tag{3.53}$$

and has an asymptotic form of

$$y_l|_{r\to\infty} \sim a_l \sin\left(kr - \frac{l\pi}{2} + \phi_l\right). \tag{3.54}$$

In Eq. (3.54), a_l is a normalization constant, and ϕ_l is the scattering phase for the l-th partial wave, which is the same for all regular solutions of Eq. (3.53). It can be shown [72] that the scattering amplitude can be represented in terms of the phase shifts as

$$f(\theta) = \frac{1}{k}\sum_{l=0}^{\infty}(2l+1)\,P_l(\cos\theta)\,e^{i\phi_l}\sin\phi_l\,, \tag{3.55}$$

and therefore the scattering cross-section $\sigma(\Omega) = |f(\Omega)|^2$ may also be expressed in this manner. The important point is that all of the information regarding the effect of the scattering potential is contained in the phase shifts. We note that the only difference in a half-scattering process such as ionization is that the phase shift obtained from a full-scattering process is divided by two.

Now, although associating time with a quantum operator faces fundamental conceptual difficulties [99], Eisenbud [68], Wigner [69], and Smith [70] pointed out that when restricted to the domain of scattering states, an expectation value of the time operator can be formed using the correspondence identity $t \to -i\frac{\partial}{\partial E}$, which for the case of scattering off a spherical potential [22] gives a group delay for each partial wave as

$$\Delta t_{WS}(E,l) = 2\frac{\partial\phi_l(E)}{\partial E}, \tag{3.56}$$

and therefore in a half-scattering process, by dividing by two we end up with Eq. (2.1). This expression then represents the time delay of the outgoing wavepacket relative to that of a free particle wavepacket traversing the same scattering region. It is implied from the use of asymptotic solutions in the derivation that the scattering region extends to infinity, which justifies writing the WS delay as Eq. (2.1).

In the above discussion, we have assumed that the binding potential decays to zero faster than $1/r$, a condition which the Coulomb potential, which is of central importance to this thesis, does not satisfy. The scattering problem may be adjusted accordingly by observing that the asymptotic form of the wavefunction should now be a Coulomb wave [72] as opposed to a plane wave. For the scattering of an electron by the Coulomb potential $V(r) = -Z/r$ with nuclear charge Z, the

asymptotic form of the outgoing wavefunction is proportional to

$$\psi_{\text{Coulomb}}|_{r\to\infty} \sim \sin\left(kr - \frac{l\pi}{2} + \sigma_l + \frac{Z}{k}\ln(2kr)\right) \tag{3.57}$$

where

$$\sigma_l = \arg\Gamma\left(l + 1 - i\frac{Z}{k}\right) \tag{3.58}$$

is the so-called Coulomb phase shift and the term $\frac{Z}{k}\ln(2kr)$ is the well known logarithmic divergence of the Coulomb potential, and is the reason that the scattering phase, and therefore the WS delay, diverges for Coulomb scattering, as was discussed at the beginning of Chapter 2. We use these phases and discuss the logarithmic divergence as it applies to attosecond streaking in further detail in Chapter 4.

3.2 Numerical Methods

In general, the above methods for solving Eq. (3.1) and its observables are not always applicable, and so in such a case we need methods of obtaining the solutions numerically. For example, our discussion of perturbation theory in section 3.1.3 depends on the condition that the interaction of the laser with the electron is of significantly less strength than the interaction of the electron with the binding Coulomb potential. Nevertheless, once the field is of sufficient strength, as is common in strong-field laser physics, the two interactions are now of similar magnitude. In such a case, perturbation theory can not be used; neither interaction can be considered as a perturbation to the other.

In this section, we describe our methods for obtaining the solution of the relevant TDSE numerically. For all cases, we discretize the TDSE on a spatial and temporal grid. Since this grid must be finite, it is possible that part of the wavefunction reaches the grid boundary during propagation. Therefore we also describe our method of including effective absorbers along the boundaries of the grid in space, in order to suppress reflections at the boundaries. Such reflections give non-physical effects in simulations, and therefore must be eliminated to a sufficient degree.

We conclude this section with a discussion of how to obtain time delays from streaking simulations using the solutions of the corresponding TDSE.

3.2.1 Discretization and propagation of the TDSE

We are primarily interested in the interaction of matter when exposed to an ultrashort laser pulse. That is, the operator $\hat{V}_I(\mathbf{r}, t)$ in Eq. (3.1) includes this time-dependent interaction. We describe $\hat{H}_0(\mathbf{r})$ using Eq. (3.21), which is time-independent and its eigenfunctions correspond to the field-free bound states of the system. We mentioned in section 3.1.2 that the observables obtained from the TDSE are gauge independent with respect to how we represent the interaction Hamiltonian. That is, the field-matter interaction term $\hat{V}_I$ can be represented in different gauges, and it was mentioned that there were advantages in using one over the other in numerical simulations, depending on the physics being studied. Despite the invariance of the solutions with respect to the gauge chosen, in practice the choice of gauge affects various aspects of the numerical calculations. While the velocity gauge has been found to converge more rapidly for simulating the interaction of atomic hydrogen with intense, low-frequency laser pulses [100], the length gauge has been shown to be more accurate for calculating photomomentum spectra [101–104], such as is necessary for streaking simulations. We therefore use length gauge for our calculations, unless explicitly mentioned otherwise.

A common method of solving second-order partial differential equations like Eq. (3.1) is to discretize the wavefunction on a spatial-temporal grid with spatial step Δx_j along the j-th dimension (with number of points for M dimensions $\{N_{x_1}, N_{x_2}, ..., N_{x_M}\}$), and propagating the solution forward in time by discrete intervals Δt. In order to propagate the solution by Δt, we need to discretize the time-evolution operator discussed in section 3.1.3.

The goal is to obtain an accurate representation of the evolution operator over the interval $[t_i, t_{i+1}]$ for $i \in [0, N-1]$ where N is the number of time intervals. We recall from the discussion in section 3.1.3 that the time evolution operator is completely determined by the Hamiltonian.

Therefore, we begin by discretizing Eq. (3.25) as [94]:

$$\hat{U}\left(t_{i+1}, t_i\right) = \hat{1} - i \int_{t_i}^{t_{i+1}} \hat{H}\left(t_1\right) \hat{U}\left(t_1, t_i\right) dt_1, \tag{3.59}$$

and by iteration, we get the result as

$$\hat{U}\left(t_{i+1}, t_i\right) = \hat{1} - \sum_{n=1}^{\infty} \hat{U}_n\left(t_{i+1}, t_i\right), \tag{3.60}$$

where

$$\hat{U}_n\left(t_{i+1}, t_i\right) = (-i)^n \int_{t_i}^{t_{i+1}} dt_1 \int_{t_i}^{t_1} dt_2 ... \int_{t_i}^{t_{n-1}} dt_n \hat{H}\left(t_1\right) \hat{H}\left(t_2\right) ... \hat{H}\left(t_n\right). \tag{3.61}$$

Now, given that the number of time intervals N is sufficiently large, we can make the approximation that the Hamiltonian $\hat{H}\left(t\right)$ stays constant during each interval $[t_i,\, t_{i+1}]$ and thus

$$\hat{H}\left(t\right) = \hat{H}\left(t_i\right) \quad \text{for} \quad t_i \leq t \leq t_{i+1}. \tag{3.62}$$

With this assumption, the integrals in (Eq. 3.61) are now simplified to

$$\hat{U}_n\left(t_{i+1},\, t_i\right) = (-i)^n \frac{\left[\hat{H}\left(t_i\right) \Delta t\right]^n}{n!}. \tag{3.63}$$

We are then able to formally sum Eq. (3.60) to yield our approximation for the evolution operator as

$$\hat{U}\left(t_{i+1},\, t_i\right) = e^{-i\hat{H}(t_i)\Delta t}. \tag{3.64}$$

This means that for each small time step taken by the wavefunction, we have

$$\Psi\left(\mathbf{r}, t + \Delta t\right) \simeq e^{-i\hat{H}(t)\Delta t} \Psi\left(\mathbf{r}, t\right). \tag{3.65}$$

3.2.1.1 Split-operator scheme

A further simplification to solving the TDSE in multiple dimensions can be made by decomposing the Hamiltonian along each of the N_M spatial dimensions of the problem as (using the length gauge as an example)

$$\hat{H}_{\text{tot}} = \hat{H}_{x_1} + \hat{H}_{x_2} + ... + \hat{H}_{x_M}, \tag{3.66}$$

where

$$\hat{H}_{x_1} = -\frac{\nabla_{x_1}^2}{2} + \mathbf{E}\cdot\mathbf{x}_1 + \frac{V(\mathbf{r})}{M}, \tag{3.67}$$

$$\hat{H}_{x_2} = -\frac{\nabla_{x_2}^2}{2} + \mathbf{E}\cdot\mathbf{x}_2 + \frac{V(\mathbf{r})}{M}, ... \tag{3.68}$$

$$\hat{H}_{x_M} = -\frac{\nabla_{x_M}^2}{2} + \mathbf{E}\cdot\mathbf{x}_M + \frac{V(\mathbf{r})}{M} \tag{3.69}$$

With this decomposition, we may rewrite Eq. (3.65) as

$$\Psi(\mathbf{r}, t+\Delta t) \simeq e^{-i\hat{H}_{x_1}(t)\frac{\Delta t}{2}} e^{-i\hat{H}_{x_2}(t)\frac{\Delta t}{2}} \ ... \ e^{-i\hat{H}_{x_M}(t)\Delta t} \ ... \ e^{-i\hat{H}_{x_2}(t)\frac{\Delta t}{2}} e^{-i\hat{H}_{x_1}(t)\frac{\Delta t}{2}}, \tag{3.70}$$

using the Baker-Campbell Hausdorff formula, which can be shown to have accuracy $O\left(\Delta t^3\right)$ [105]. In general, we will not consider $M > 3$ in this thesis, however the strategy extends to any number of dimensions and is not restricted by the coordinate geometry chosen. Using this method, known as the split-operator scheme, the propagation of the wavefunction in time is now reduced to subsequent propagation along a single dimension at a time. In the next section, we demonstrate the propagation procedure, but using only a single dimension for clarity.

3.2.1.2 Crank-Nicolson Method

The Crank-Nicolson method [106] is a standard method for numerically obtaining the solution of partial differential equations. It is a unitary, stable, and energy conserving method which can describe the solution of the TDSE to second order accuracy in space and time. For small time steps Δt, the solution of the Schrödinger equation can be approximated as

$$\Psi(t+\Delta t) \approx e^{-iH(t)\Delta t}\Psi(t) \approx \frac{1 - i\frac{\Delta t}{2}H}{1 + i\frac{\Delta t}{2}H}\Psi(t). \tag{3.71}$$

where the Cayley unitary transformation [107] is used on the right hand side, which preserves the norm of the wavefunction. It then follows that

$$\left(1 + i\frac{\Delta t}{2}H\right)\Psi(t+\Delta t) = \left(1 - i\frac{\Delta t}{2}H\right)\Psi(t). \tag{3.72}$$

Now, the Hamiltonian $\hat{H}(t)$ can be decomposed into different coordinates, where each component is a one-dimensional (1D) Hamiltonian given by

$$H = A(x,y,t)\frac{\partial^2}{\partial x^2} + B(x,y,t)\frac{\partial}{\partial x} + V(x,y,t), \tag{3.73}$$

where x stands for the coordinate of interest and y represents the remaining spatial coordinates. $A(x,y)$ and $B(x,y)$ are functions which are chosen to be appropriate for the geometry of the system. Then using the second-order discretization scheme, Eq. (3.72) reveals

$$\begin{aligned} & \Psi_n(t+\Delta t) + i\frac{\Delta t}{2}\left(A_n(y)\frac{\Psi_{n+1}(t+\Delta t) - 2\Psi_n(t+\Delta t) + \Psi_{n-1}(t+\Delta t)}{(\Delta x)^2}\right. \\ & \left. + B_n(y)\frac{\Psi_{n+1}(t+\Delta t) - \Psi_{n-1}(t+\Delta t)}{2\Delta x} + V_n(y)\Psi_n(t+\Delta t)\right) \\ = \; & \Psi_n(t) - i\frac{\Delta t}{2}\left(A_n(y)\frac{\Psi_{n+1}(t) - 2\Psi_n(t) + \Psi_{n-1}(t)}{(\Delta x)^2}\right. \\ & \left. + B_n(y)\frac{\Psi_{n+1}(t) - \Psi_{n-1}(t)}{2\Delta x} + V_n(y)\Psi_n(t)\right), \end{aligned} \tag{3.74}$$

where n represents the respective grid point in the x-direction on the discretized spatial grid.

Equation (3.74) leads to the following system of linear equations:

$$\begin{pmatrix} {}_2X_1 & {}_3X_1 & 0 & 0 & \cdots & 0 & 0 & 0 \\ {}_1X_2 & {}_2X_2 & {}_3X_2 & 0 & \cdots & 0 & 0 & 0 \\ 0 & {}_1X_3 & {}_2X_3 & {}_3X_3 & \cdots & 0 & 0 & 0 \\ \vdots & \vdots & \vdots & \vdots & \ddots & \vdots & \vdots & \vdots \\ 0 & 0 & 0 & 0 & \cdots & {}_1X_{N-1} & {}_2X_{N-1} & {}_3X_{N-1} \\ 0 & 0 & 0 & 0 & \cdots & 0 & {}_1X_N & {}_2X_N \end{pmatrix} \begin{pmatrix} \Psi_1(t+\Delta t) \\ \Psi_2(t+\Delta t) \\ \Psi_3(t+\Delta t) \\ \vdots \\ \Psi_{N-1}(t+\Delta t) \\ \Psi_N(t+\Delta t) \end{pmatrix}$$

$$= \tag{3.75}$$

$$\begin{pmatrix} {}_2Y_1 & {}_3Y_1 & 0 & 0 & \cdots & 0 & 0 & 0 \\ {}_1Y_2 & {}_2Y_2 & {}_3Y_2 & 0 & \cdots & 0 & 0 & 0 \\ 0 & {}_1Y_3 & {}_2Y_3 & {}_3Y_3 & \cdots & 0 & 0 & 0 \\ \vdots & \vdots & \vdots & \vdots & \ddots & \vdots & \vdots & \vdots \\ 0 & 0 & 0 & 0 & \cdots & {}_1Y_{N-1} & {}_2Y_{N-1} & {}_3Y_{N-1} \\ 0 & 0 & 0 & 0 & \cdots & 0 & {}_1Y_N & {}_2Y_N \end{pmatrix} \begin{pmatrix} \Psi_1(t) \\ \Psi_2(t) \\ \Psi_3(t) \\ \vdots \\ \Psi_{N-1}(t) \\ \Psi_N(t) \end{pmatrix},$$

where now N is the total number of grid points in the x-direction and

$$\begin{aligned} {}_1X_n &= \frac{i\Delta t}{2(\Delta x)^2}A_n(y) - \frac{i\Delta t}{4\Delta x}B_n(y), && (3.76) \\ {}_2X_n &= 1 - \frac{i\Delta t}{(\Delta x)^2}A_n(y) + \frac{i\Delta t}{2}V_n(y), && (3.77) \\ {}_3X_n &= \frac{i\Delta t}{2(\Delta x)^2}A_n(y) + \frac{i\Delta t}{4\Delta x}B_n(y), && (3.78) \\ {}_1Y_n &= -\frac{i\Delta t}{2(\Delta x)^2}A_n(y) + \frac{i\Delta t}{4\Delta x}B_n(y), && (3.79) \\ {}_2Y_n &= 1 + \frac{i\Delta t}{(\Delta x)^2}A_n(y) - \frac{i\Delta t}{2}V_n(y), && (3.80) \\ {}_3Y_n &= -\frac{i\Delta t}{2(\Delta x)^2}A_n(y) - \frac{i\Delta t}{4\Delta x}B_n(y). && (3.81) \end{aligned}$$

The matrix on the left side of Eq. (3.75) is of tridiagonal form, and thus the linear equations can be solved by LU decomposition [108]. We note that the symmetry of the Hamiltonian is adapted by

modifying the boundaries of the grid in the relevant spatial dimension. As an example, in cylindrical coordinates the radial coordinate ρ lies in the interval $[0, \rho_{max}]$, which requires a modification of the boundary condition at $\rho = 0$.

Due to recent developments in our code, we are able to do a Crank-Nicolson propagation directly (as opposed to using the split-operator scheme, c.f., Eq. (3.70)) with

$$\Psi\left(\mathbf{r}, t + \Delta t\right) = e^{i\hat{H}(t)\Delta t}\Psi\left(\mathbf{r}, t\right), \tag{3.82}$$

which scales as $O(N\log N)$, but has advantages in parallelization, specifically with regards to distributed memory. Therefore, given a large number ($\gtrapprox 1000$) CPU cores and with the use of PETSc and SLEPc [109, 110], the direct Crank-Nicolson propagation with the total Hamiltonian becomes less costly than the split operator technique. Once implemented in our code, the direct Crank-Nicolson propagation was used as an alternative, in particular for the simulations in Chapter 6.

3.2.2 Calculation of bound states

In order to determine the initial conditions for solving Eq. (3.1), which typically is an eigenstate of the system of interest, we need to solve the time-independent Schrödinger equation

$$\hat{H}_0\Psi\left(\mathbf{r}\right) = E\Psi\left(\mathbf{r}\right), \tag{3.83}$$

with certain boundary conditions (e.g., $\Psi\left(r = 0\right) = \Psi\left(r \to \infty\right) = 0$ for a 3D Coulomb potential). In order to solve this equation for one or many dimensions, it has been shown that the imaginary time propagation (ITP) method as well as the Krylov-Schur method implemented in SLEPc are two dependable tools in obtaining eigenvalues and eigenvectors for the system being studied [109, 110]. ITP is based upon the propagation of a random guess for a wavefunction (usually a Gaussian wavepacket for atomic states) in the field-free Hamiltonian, i.e.,

$$i\frac{\partial\Psi\left(\mathbf{r}, t\right)}{\partial t} = \hat{H}_0\Psi\left(\mathbf{r}, t\right). \tag{3.84}$$

One may write the time-dependent wavefunction $\Psi(\mathbf{r},t)$ as an expansion in the Hilbert space of $\hat{H}_0$:

$$\Psi(\mathbf{r},t)=\sum_j c_j\phi_j(\mathbf{r})\,e^{-iE_jt}, \tag{3.85}$$

where $\phi_j(\mathbf{r})$ represents the jth eigenstate with energy eigenvalue E_j, and c_j is the amplitude coefficient, which is the projection of $\Psi(\mathbf{r},t=0)$ onto $\phi_j(\mathbf{r})$. If we propagate in imaginary time, i.e., $t\rightarrow -it'$ starting from our initial guess, the wavefunction after N propagation steps of time step Δt becomes

$$\Psi(\mathbf{r},t=N\Delta t)=\sum_j c_j\phi_j(\mathbf{r})\,e^{-iE_jN\Delta t}, \tag{3.86}$$

If N is sufficiently large, the first term is vastly larger than the others, and so all other terms become negligible, i.e.,

$$\frac{c_je^{-iE_jN\Delta t}}{c_0e^{-iE_0N\Delta t}}=\frac{c_j}{c_0}e^{-i(E_0-E_j)N\Delta t}\rightarrow 0. \tag{3.87}$$

Therefore, the ground state is solved for as

$$\phi_0(\mathbf{r})=\Psi'(\mathbf{r},t=N\Delta t) \tag{3.88}$$

where $\Psi'(\mathbf{r},t=N\Delta t)$ denotes the normalized wavefunction in this instance. The excited states are obtained with the same idea, however the states that are lower in energy than the calculated state need to be projected out after each propagation step.

ITP works well for most of our simulations, and is easy to implement. However, the accuracy and efficiency of the method can at times be less ideal. In these cases we use the highly parallel Krylov-Schur method using SLEPc [110]. In particular, when more than 4 or 5 eigenstates are needed for a simulation of a process in more than one dimension, ITP converges at a relatively slow rate. Using SLEPc, we are able to solve for many tens of eigenstates on a similar time scale. Furthermore, in two or more dimensions, the split operator technique is used when implementing ITP, which is limited in its parallel capabilities as compared to using SLEPc and Krylov-Schur (see previous section).

3.2.3 Exterior complex scaling

In order to simulate ionization processes, we need to propagate the ionized outgoing wavepacket on the finite-grid. If no boundary conditions are implemented however, eventually this wavepacket will be reflected by the boundaries of our grid. Such a reflection causes artificial processes to occur in our simulations which are not physical, such as interference with a slower outgoing wavepacket, and therefore must be eliminated. We use the exterior complex scaling (ECS) method to avoid this complication [111–113]. In ECS, an exponentially decaying term in the propagator absorbs the outgoing flux, which may happen if a complex coordinate axis is artificially set in the absorbing region as (assuming 1D for simplification):

$$x = x_0 + (x - x_0)\, e^{i\eta}, \tag{3.89}$$

where η is the scaling angle with $0 < \eta < \pi/2$ and x_0 is the starting point of the absorbing boundary. In the length-gauge, the solution of the reduced 1D TDSE from Eq. (3.1) in the absorption region is

$$\begin{aligned} \Psi\left(t + \Delta t\right) &= e^{-i\left(\hat{p}^2/2 + V_0(x) + E(t)x\right)\Delta t}\Psi\left(t\right) \\ &= e^{-i\cos(2\eta)\hat{p}^2\Delta t/2} e^{-\sin(2\eta)\hat{p}^2\Delta t/2} e^{-iV_0(x)\Delta t} e^{-iE(t)\left[x_0 + (x-x_0)e^{i\eta}\right]\Delta t}\Psi\left(t\right), \end{aligned} \tag{3.90}$$

with the field-free potential term $V_0\left(x\right)$ untransformed in this region and

$$e^{-iE(t)\left[x_0 + (x-x_0)e^{i\eta}\right]\Delta t} = e^{-iE(t)[x_0 + (x-x_0)\cos\eta]\Delta t} e^{E(t)[x_0 + (x-x_0)\sin\eta]\Delta t}. \tag{3.91}$$

It is clear that in the second row of Eq. (3.90), the second exponential decays exponentially and hence can absorb the outgoing probability that has entered the boundary region. It is important to note however that the second exponential term on the right-hand side of Eq. (3.91) can become an undesired source when the sign of the electric field $E\left(t\right)$ is positive. Under certain extreme conditions, this term causes the wavefunction to blow up, inducing numerical issues. It has therefore been recommended by He *et al.* [111] and McCurdy and coworkers [112], amongst others, that the ECS method be implemented without rotating the electric field interaction into the complex plane.

That is, one drops the $e^{i\eta}$ term in Eq. (3.91), and instead propagates using

$$\Psi\left(t+\Delta t\right)=e^{-i\cos(2\eta)\hat{p}^{2}\Delta t/2}e^{-\sin(2\eta)\hat{p}^{2}\Delta t/2}e^{-iV_{0}(x)\Delta t}e^{-iE(t)x\Delta t}\Psi\left(t\right), \tag{3.92}$$

meaning that the non-transformed standard field coupling is used over the entirety of the grid, which includes the absorbing region. Further work on this method was done by McCurdy and coworkers [112] and Scrinzi [113], amongst others. The work of [112] showed that numerical error can arise for long-time propagations, but can be controlled by extending the finite grid. This work also showed that the procedure is formally exact when applied in the appropriate gauge. The method described in [113] is called infinite-range ECS. It is given this name because in principle, the method also keeps a record of the dynamics in the region outside the absorber. In conclusion, this relatively simple modification of the traditional ECS method has been shown to be a dependable absorber of the outgoing flux without any undesirable divergences, and also effectively suppresses reflections as compared to the use of a masking function [111–113], and we therefore use it in our simulations throughout this thesis.

3.3 Extraction of time delays from simulations of attosecond streaking

In Chapter 1, we introduced the streaking time delay as the temporal shift of the observed streaking trace with respect to the trace predicted by the original streaking formula, $\mathbf{k}_f = \mathbf{k}_0 - \mathbf{A}_s\left(t_i\right)$. In order to obtain this delay in numerical simulations, we need to calculate the streaking trace as accurately as possible without making excessive approximations [16]. We therefore simulate the streaking experiment by numerically solving the following TDSE:

$$i\frac{\partial\Psi(\mathbf{r},t)}{\partial t}=\left[\frac{p^{2}}{2}+V(\mathbf{r})+\left(\mathbf{E}_{\mathrm{XUV}}\left(t\right)+\mathbf{E}_{s}\left(t\right)\right)\cdot\mathbf{r}\right]\Psi(\mathbf{r},t), \tag{3.93}$$

where we assume that the ionizing and streaking fields $\mathbf{E}_{XUV}$ and $\mathbf{E}_s(t)$ are polarized along the same axis, which we define as the $\hat{z}$-direction without loss of generality.

We must solve Eq. (3.93) for each delay between the XUV and streaking (IR) pulses to get a streaking trace. We do so on a grid in space and time by using the common Crank-Nicolson

method described above. In each simulation we propagate the wavefunction on the grid for a sufficient time such that both pulses have ceased and the ionized wavepacket is far from the ionic core. We confirm in every simulation that the outgoing wavepackets stay on the grid and do not reach the boundaries. It is required to have a small enough time step to capture the interaction of the attosecond XUV pulse with the atom or molecule, whilst also having a large grid to allow for the separation of the photoelectron wavepacket from the remaining core. For this reason, separating the ionized wavepacket in this manner can become costly in certain limits.

The streaking trace itself is characterized by a momentum distribution as a function of XUV-IR delay. To this end, we spatially separate the ionized wavepacket from the rest of the wavefunction, which is possible due to the long propagation times used in the simulations, and then perform a Fourier transform of the remaining wavepacket. This therefore requires propagating the ionizing wavepacket sufficiently far away from the nucleus so that the small error due to projection onto plane waves instead of Coulomb waves is negligible [16]. After varying the XUV-IR delay τ a sufficient number of times, we obtain the streaking trace, in which the momentum of the photoelectron along the polarization direction of the field $k_{f,z}$ is given as a function of τ. For the present case we normally present the streaking trace in the form of the expectation value of the final momentum as a function of the relative delay in order to compare with other calculations. For model systems with one spatial dimension this is trivial, however for systems with more than one dimension, we calculate the expectation value of the momentum in the laser polarization direction with an opening angle of 5 to 10 degrees [16]. As mentioned prior, the streaking time delay relates to a momentum shift Δk and can be understood as the temporal shift of the TDSE trace with respect to the trace predicted by the original streaking formula. In practice, we do not compare these two traces directly in order to obtain the streaking delay (see section 1.3.1.1). Instead we extract the delay by fitting the TDSE streaking trace to

$$k_{f,z}(\tau) = k_{0,z} - \alpha A_s(\tau + \Delta t_s) \tag{3.94}$$

where $k_{0,z}$, α, and Δt_s are three fitting parameters, which can be retrieved using a least-square

method.

In Chapter 2, we discussed the existence of an absorption delay in the attosecond streaking of resonant two-photon ionization of atoms. For extracting the absorption delay in such processes in our calculations, we obtain two streaking traces for each simulation. As discussed in section 2.3, we may determine the continuum delay by calculating the streaking trace for a one-photon ionization process of the same final electron kinetic energy [20]. Alternatively, we can get the continuum delay via classical calculations of the streaking trace (c.f., section 2.2.2). Both methods are used in certain cases throughout this thesis. It is then straightforward to calculate the absorption delay Δt_a by subtracting the continuum delay Δt_c from the observed streaking delay Δt_s in the resonant two-photon process, as is shown in Fig. 3.1.

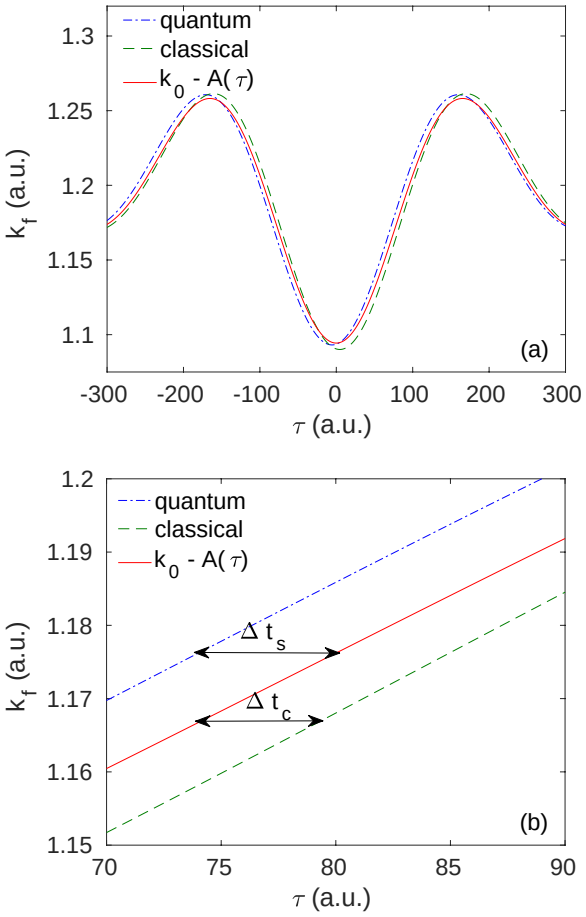

Figure 3.1: Three streaking traces for a resonant two-photon ionization from numerical streaking simulations (blue solid curve), classical electron trajectory calculations (green dashed line), and the reference free-particle streaking formula $k_f^{free}(\tau) = k_0 - A_s(\tau)$ (red dashed-dotted curve). Panel (b) is an enlargement of the traces in panel (a) to show the streaking (Δt_s) and continuum (Δt_c) time delay. Laser parameters used in the simulations are: $I_{\rm XUV} = 1.0 \times 10^{13}$ W/cm^2, $\omega_{\rm XUV} = 81.81$ eV, $T_{\rm XUV} = 550$ as, and $\phi_{\rm XUV} = -\pi/2$; $I_s = 1.0 \times 10^{11}$ W/cm^2, $\lambda_s = 2400$ nm, $N_s = 3$, and $\phi_{\rm s} = -\pi/2$.

Chapter 4

Analytical estimates of time delays in streaked photoionization of atoms

With the measurement of a photoemission delay in an attosecond streaking experiment [17], it became crucial for theorists to explain the experimental observation with results of high level calculations. Although agreement with experiment has not been achieved in each case, much insight was gained during the analysis of the problem. The streaking time delay Δt_s is usually studied via the sum of the Wigner-Smith time delay Δt_{WS} [69, 70], related to the short-range part of the residual ion potential, and a term Δt_{CLC}, related to the coupling between the laser field and the long-range part of the Coulomb potential [17, 22, 24–26, 64, 73, 85–91, 114].

In this Chapter, we set out with an alternative estimate of the streaking time delay, which consists of a sum of streaking field weighted field-free delays [92], in order to derive in section 4.1 an analytical formula describing the streaking delay. With the analytical formula, we are able to obtain predictions for the streaking time delay in a few seconds, while the results are in very good agreement with those of numerical simulations, which typically take hours or days of computation time. We then show that by separating long- and short-range terms in the formula, we can recover the two aforementioned terms previously used to describe the observed delay, and hence provide an alternative justification of the widely used sum rule. Finally, we proceed by showing that the analytical formula offers the opportunity to effectively analyze other theoretical interpretations as well as potential effects, such as the effect of an attochirp in the ionizing XUV pulse.We then show an application of our analytical formula in determining the effect of an attochirp on the streaking delay in section 4.2.2.

4.1 Short- and long-range contributions to the streaking delay[1]

In this section, we develop an analytical estimation of the streaking delay. Using our analytical form, we are able to study the connection between the two interpretations of the streaking delay discussed in Chapter 2. That is, under certain approximations the streaking field weighted field-free delay sum may be further approximated by the sum of the Wigner-Smith delay and Coulomb laser coupling term.

4.1.1 Field-free time delays and the cutoff Coulomb potential

The separation of short- and long-range behavior of the photoelectron phase in a streaking process has previously been performed by attributing the short-range behavior to a Wigner-Smith (WS) delay, and the long range behavior to a Coulomb-laser-coupling (CLC) term. The WS delay, as discussed before, refers to the energy derivative of the phase shift of the electronic wavepacket induced by the potential as compared to a free particle. The phase shift due to a Coulomb potential can be evaluated using asymptotic forms (see, e.g., [71], section 3.1.5), where the long range characteristics of the Coulomb potential show up in a logarithmic divergence term, and the phase shift for an electron traversing across such a potential is

$$\begin{aligned} \phi_{total} &= \phi_{\text{Coulomb}} + \phi_{\log} && (4.1) \\ &= \arg\left[\Gamma\left(1 + l + i\eta\right)\right] + \frac{Z}{k}\ln\left(2kr\right). && (4.2) \end{aligned}$$

The logarithmic divergence term makes it difficult to define a Wigner-Smith delay for a photoelectron escaping a Coulomb potential, and it is the tail of the Coulomb potential, coupled to the laser field, which is deemed relevant for the CLC term in (e.g., [17, 22, 24–26, 64, 73, 85–91, 114]):

$$\Delta t_s = \Delta t_{WS} + \Delta t_{CLC}\ . \tag{4.3}$$

In this section we will show how the finite-range behavior of the streaking delay can recover this separation of short- and long-range effects.

[1] The results of this section are also presented in C. Goldsmith, J. Su, A. Becker, and A. Jaroń-Becker, Phys. Rev. A **96**, 053410 (2017).

In section 2.2.2, we discussed that using a classical analysis it was found that the streaking time delay can be approximated as

$$\Delta t_s \simeq \frac{1}{E_s\left(t_i\right)} \int_{t_i}^{T_s} E_s\left(t\right) \left[1 - \frac{k_z^{(0)}\left(t\right)}{k_{0,z}}\right] dt. \tag{4.4}$$

When put in the form of a discrete sum, we had

$$\Delta t_s \simeq \sum_{j=1}^{N} \frac{E_s(t_j)}{E_s(t_{ion})}\, \Delta t_{ff}^{(j)}\,, \tag{4.5}$$

where $\Delta t^{(j)}_{\text{field-free}}$ is a piecewise field-free time delay that the electron accumulates during its propagation in the time interval $[t_j, t_j + \delta t]$ and over the related finite region $[z_j, z_j + \delta z]$ of the potential $V(\mathbf{r})$ as compared to the propagation of a free particle over the same distance in space. This formula states that the streaking delay may be considered as a sum of (streaking) field weighted field-free delays over a finite range and duration. The finite-range behavior is dictated by the duration of the streaking pulse. That is, the streaking delay is only accumulated until the end of the IR pulse, and hence probes the (long range) Coulomb potential over a finite distance only. It is therefore useful to consider a cutoff Coulomb potential, which has a finite phase-shift, and therefore does not diverge like the unmodified Coulomb potential.

In order to obtain an analytical expression, we write the field-free time delay as a difference:

$$\Delta t_{ff}^{(j)} = \Delta t_{ff}(k_{j+1}, r_{j+1}) - \Delta t_{ff}(k_j, r_j). \tag{4.6}$$

Here, $\Delta t_{ff}\left(k, r\right)$ is the field-free time delay accumulated during the propagation of the photoelectron, from the origin of the transition into the continuum by an XUV photon to location r, with constant momentum $k = k\left(r\right) = \sqrt{2(E_{asym} - V(r))}$, where E_{asym} is the asymptotic kinetic energy of the photoelectron. Considering the classical calculations for the streaking delay showing good agreement with full quantum mechanical simulations [73, 92], we assume a quantum-classical correspondence for the field-free time delay. Thus, we further decompose the (classical) time delay into three well-known terms:

$$\Delta t_{ff}(k, r) = \Delta t_{short}(k, r) + \Delta t_{phase}(k, r) + \Delta t_{log}(k, r). \tag{4.7}$$

Each of these terms represents the derivative of a contribution to the (quantum) phase shift with respect to the energy of the photoelectron. Δt_{short} is the short-range contribution, while

$$\Delta t_{phase}(k,r) = \frac{1}{k}\frac{\partial}{\partial k}\arg\left[\Gamma(1+l+i\eta)\right] \tag{4.8}$$

and

$$\Delta t_{log}(k,r) = \frac{1}{k}\frac{\partial}{\partial k}\left[\frac{Z}{k}\ln(2kr)\right] \tag{4.9}$$

where l is the angular momentum of the photoelectron, $\eta = -Z/k$ and Z is the charge of the residual ion. Since the sum is terminated at the end of the streaking pulse, we see that the sum over field-free delays will not diverge, despite that it contains a contribution from the logarithmic divergence term.

We furthermore recall that $\Delta t_{ff}(k,r)$ corresponds to the field-free time delay accumulated in the atomic potential, which is cut-off at r, and the phase-shift can be evaluated as explained above. The assumed quantum-classical correspondence in Eq. (4.7) is therefore expected to hold for cut-off distances, at which the short-range part of the potential has vanished. Conversely, for distances close to the core of the residual ion, at which multi-electron dynamics play a dominant role, the above assumption is no longer valid. Thus, for small energies, at which the photoelectron explores the short-range part of the potential for a significant time of the interaction with the pulse, this may lead to discrepancies between the analytical estimates, to be derived in the next subsections, and the results of advanced ab-initio quantum calculations.

4.1.2 Analytical formulation

4.1.2.1 Hydrogen-like systems: Coulomb-phase and logarithmic terms

We first consider the case of hydrogen-like atoms and ions with a bare Coulomb potential $V(r) = -Z/r$ without short-range contributions. The spectral derivative in Eq. (4.9) is readily determined as

$$\Delta t_{log}(k,r) = \frac{Z}{k^3}\left[1 - \ln(2kr)\right]. \tag{4.10}$$

Again, it is important to emphasize that since the streaking time delay, Eq. (4.5) depends on finite distances only, this term will not diverge. The Coulomb-phase term, Eq. (4.8), can be expressed in terms of the real part of the digamma function [26]. Here however, we use an expansion of the complex argument of the gamma function [115]:

$$\arg\left[\Gamma\left(x+iy\right)\right]=y\psi\left(x\right)+\sum_{n=0}^{\infty}\left[\frac{y}{x+n}-\arctan\left(\frac{y}{x+n}\right)\right], \tag{4.11}$$

where $\psi\left(x\right)$ is the polygamma function, and we use $x=l+1$ and $y=-\frac{Z}{k}$. Since $l+1>0$ for any possible angular momentum quantum number l, the polygamma function $\psi\left(l+1\right)$ in this expansion is well defined, and can be written as:

$$\psi\left(l+1\right)=-\gamma+\sum_{j=1}^{l}\frac{1}{j}, \tag{4.12}$$

where $\gamma\simeq 0.5772$ is the Euler constant. Using this expansion and the result for $\Delta t_{\log}$, we get the analytical expression for the field-free delay as

$$\Delta t_{ff}(k,r)=\frac{Z}{k^3}\left[F(k,l)+\sum_{m=1}^{l}\frac{1}{m}-\gamma+1-\ln\left(2kr\right)\right] \tag{4.13}$$

where

$$F(k,l)=\sum_{n=0}^{\infty}\frac{Z^2}{(n+l+1)([k(n+l+1)]^2+Z^2)}. \tag{4.14}$$

In Fig. 4.1, the accuracy of the predictions of the analytical expression for Δt_{ff} (solid line) can be seen from the comparison with previously published data extrapolated from *ab-initio* calculations (circles, [22]) as a function of the propagation time t after liberation of the electron into the continuum. In these calculations we have used $r=k_{\mathrm{asym}}t$, where $k_{asym}=\sqrt{2E_{\mathrm{asym}}}$, in accordance with the analysis in Ref. [22].

In order to calculate the streaking delay using Eq. (4.5), we must evaluate Eq. (4.13) at N finite distances r_j. These distances are estimated via the recursive relation

$$r_{j+1}=r_j+k(r_j)\delta t \tag{4.15}$$

where $r_1=r_{ion}$ and $k\left(r_1\right)=\sqrt{2\left(E_{\mathrm{asym}}-V\left(r_1\right)\right)}$ are the initial position and momentum, respectively, of the photoelectron once it has arrived in the continuum. We note that the distances can

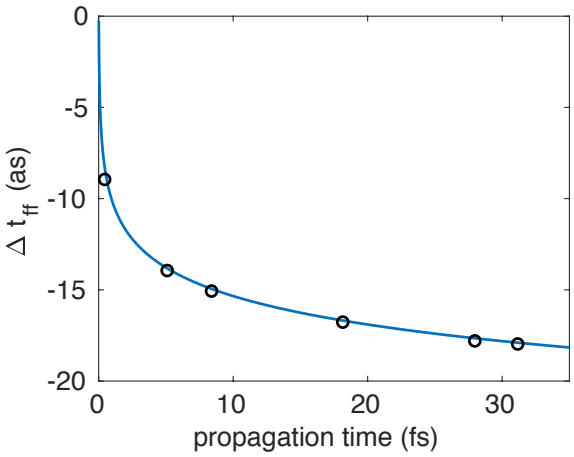

Figure 4.1: Comparison of predictions of analytical formula for the field-free time delay Δt_{ff}, Eq. (4.13), with results extrapolated from ab-initio calculations for hydrogen atom ($Z = 1$) [22] as a function of propagation time (Taken from [23]).

also be determined by using a variety of other standard approaches to solve the differential equation governing the classical trajectory $r(t)$. For such a calculation it is necessary to find δt such that convergence of the streaking delay is achieved. In Fig. 4.2, we show the percent error for three different final momenta of the electron as a function of the time-step used (log scale). We see that the calculation is very stable with respect to time step, with less than 1% error in the streaking delay for all time steps shown. We therefore choose $\delta t = 0.1$ as it allows for quick and accurate calculations.

Fig. 4.3 shows our analytical calculation of the streaking time delay for a hydrogen atom and helium ion compared to those of *ab-initio* calculations [22]. We find agreement within one attosecond over the entire range of asymptotic electron kinetic energies studied.

4.1.2.2 Short-range term for multielectron atoms

There do not exist analytical solutions for the ionization (half-scattering) of an electron from an atom with more than one electron, and because the exact numerical solution for such an atom requires excessively large calculations, the process is often modeled using single-active-electron (SAE) potentials. In such a potential, all electrons except the active photoelectron are assumed

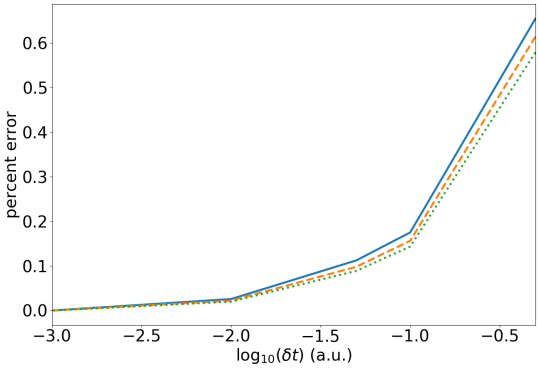

Figure 4.2: Convergence of the time delay shown as percent error of Δt_s as a function of the log of the timestep δt used for the case of the ionization of the hydrogen ground state where the final kinetic energy of the photoelectron is $k_f = 1.5$ a.u. (solid blue line), $k_f = 2.0$ a.u. (dashed orange), and $k_f = 2.5$ a.u. (dotted green). Streaking field parameters were $N = 3$ cycles, $\lambda = 800$ nm, $I_s = 1 \times 10^{12}$ W/cm^2.

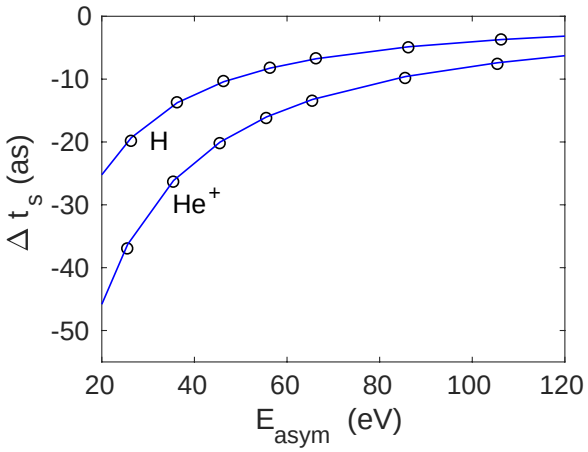

Figure 4.3: Comparison of analytical estimates (solid lines) with results of ab-initio calculations (circles, [22]) of the streaking delay in hydrogen atom and helium ion. Parameters of the streaking field: peak intensity $I_s = 1 \times 10^{12}$ W/cm^2, wavelength $\lambda_s = 800$ nm and pulse duration of three cycles. In the analytical calculations, ionization of the photoelectron at the peak of the pulse and the most probable location of the electron in the initial state has been assumed (Taken from [23]).

to be frozen during the interaction with the external fields. The corresponding SAE potentials are given by

$$V_{SAE}\left(\mathbf{r}\right) = -\frac{1}{r} + V_{\text{short}}\left(\mathbf{r}\right), \tag{4.16}$$

where the short-range part, V_{short}, is typically modeled via a linear combination of Yukawa terms, $V_{\text{Yukawa}}\left(\mathbf{r}\right) = a\exp\left(-\mu r\right)/r$, and exponential decay terms, $V_{\text{short}}\left(\mathbf{r}\right) = a\exp\left(-\mu r\right)$, with a and μ constant.

In determining the field-free time delay Δt_{ff} obtained by the photoelectron in a SAE potential, the sum of Δt_{phase} and $\Delta t_{\log}$ is given by Eq. (4.13) for $Z = 1$. Analogous to the other terms, the short-range contribution is given by the spectral derivative of the corresponding phase shift δ_{short}:

$$\Delta t_{short}(k,r) = \frac{1}{k}\frac{\partial}{\partial k}\delta_{short}(k,r). \tag{4.17}$$

In order to obtain analytical estimates of this delay, we make use of the distorted-wave Born approximation (DWBA), which accounts for scattering effects in a reference potential V_{short}, and provides good estimates as long as the difference to the real potential is sufficiently small, and the kinetic energy of the electron is not too low. Within the DWBA, we may calculate the phase shift due to the short-range part of the potential as [72]:

$$\delta_{short}(k,r) \simeq -\frac{1}{k^2}\int_0^\infty d\varrho F_{l,\eta}^2(k,r)V_{short}(r), \tag{4.18}$$

with the bare Coulomb wave function

$$F_{l,\eta}(k,r) = C_l e^{i\varrho}\varrho^{l+1}{}_1F_1\left(l+1+i\eta; 2l+2; -2i\varrho\right) \tag{4.19}$$

where $\varrho = kr$ and

$$C_l = 2^l e^{-\frac{\pi\eta}{2}}\frac{|\Gamma(l+1+i\eta)|}{\Gamma(2l+2)}. \tag{4.20}$$

For Yukawa and exponential potential terms, the integrals in Eq. (4.18) and the related derivatives in Eq. (4.17) have the following closed form solutions, which are derived in the next subsections:

$$\Delta t_{Yukawa} = \frac{\delta_{Yukawa}}{k^2}\left[f(k) + g(k) - 1\right] \tag{4.21}$$

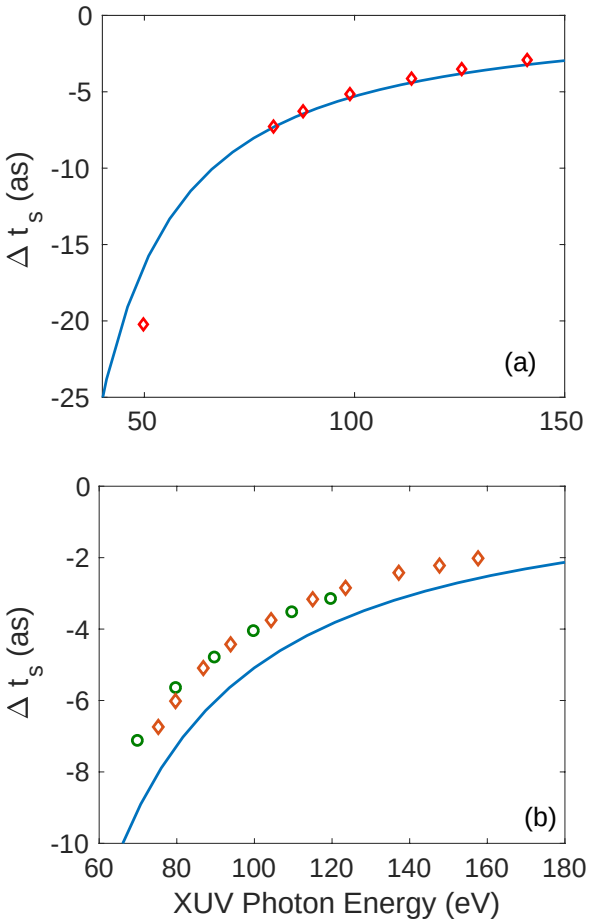

Figure 4.4: Comparison of analytical predictions (solid lines) with results of ab-initio calculations (symbols) for the streaking time delay in the case of photoionization of (a) helium (ab-initio data from [22]) and (b) neon atom as a function of the XUV photon energy. Ab-initio results for Ne are from calculations using the present SAE potential (circles, [24]) and multi-electron B-spline R-matrix calculations (diamonds, [25]) are shown. Streaking laser parameters as in Fig. 4.3 (Taken from [23]).

where the analytical forms of δ_{Yukawa}, f and g are given in Eqs. (4.25), (4.31) and (4.33) and

$$\begin{aligned}\Delta t_{exp} &= \frac{\delta_{exp}}{k}\left[\frac{2i(l+1-i\eta)}{\mu-2ik}-\frac{i\eta}{k}\log\left(1-\frac{2i}{\mu}k\right)\right.\\ &+\frac{2}{k}\left(l+\frac{\pi\eta}{2}-\frac{\eta}{k}\sum_{n=0}^{\infty}\frac{1}{(l+1+n)^2+\eta^2}\right)\\ &\left.+\frac{c_1(k)-c_2(k)-c_3(k)+c_4(k)}{c_0(k)},\right]\end{aligned} \tag{4.22}$$

the analytical forms of δ_{exp} and c_i $(i = 0, \ldots, 4)$ are given in Eq. (4.35), and Eq. (4.40) to Eq. (4.44), respectively.

We tested the analytical streaking formula by making use of the following form of the SAE potentials for electrons in the outermost shell of atoms:

$$V_{SAE}(\mathbf{r}) = -\frac{Z}{r} - \frac{a_1 e^{-\mu_1 r} + a_2 e^{-\mu_2 r}}{r} - a_3 e^{-\mu_3 r}, \tag{4.23}$$

where the parameters for various noble gas neutrals and ions are given in Ref. [97]. The streaking time delay can then be obtained in the same way as for hydrogen-like systems, using the analytical formulas for Δt_{short}, Δt_{phase} and Δt_{log}. As can be seen in Fig. 4.4, the analytical predictions are in good overall agreement with results of ab-initio calculations for photoionization of helium and neon atom. We note that in the case of ionization of Ne we have considered that the $2p \to d$ transition is strongly dominant over the $2p \to s$ one [86].

4.1.2.3 Short-range time delays for Yukawa Potentials

In this subsection we derive an analytical formula for the field-free time delay corresponding to the emission of an electron from a short range Yukawa potential of the form

$$V_{Yukawa} = \frac{a_Y \exp[-\mu r]}{r}, \tag{4.24}$$

where a_Y and μ are constants. Using the Distorted Wave Born Approximation the phase shift induced on a l-partial wave in the potential is given by [116]:

$$\begin{aligned}\delta_{Yukawa} &\simeq \frac{a_Y}{4k\Gamma(2l+2)}|\Gamma\left(l+1+i\eta\right)|^2\exp[-\pi\eta] \\ &\times\exp\left[2\eta\arctan\left(\frac{2k}{\mu}\right)\right]\left(1+\frac{\mu^2}{4k^2}\right)^{-(l+1)} \\ &\times{}_2F_1\left(l+1+i\eta,l+1-i\eta;2l+2;\frac{4k^2}{\mu^2+4k^2}\right)\end{aligned} \tag{4.25}$$

where

$$\begin{aligned}{}_2F_1\left(a,b;c;z\right) &= \sum_{n=0}^{\infty}\frac{\left(a\right)_n\left(b\right)_n z^n}{\left(c\right)_n n!} \\ &= \frac{\Gamma(c)}{\Gamma(b)\Gamma(c-b)}\int_0^1 dt\; t^{b-1}(1-t)^{c-b-1}(1-zt)^{-a}\end{aligned} \tag{4.26}$$

is the convergent Gaussian hypergeometric function, given both as series and Euler integral representation, with

$$(a)_i = \frac{\Gamma(a+i)}{\Gamma(a)}. \tag{4.27}$$

is the Pochhammer symbol.

Calculation of the corresponding time delay

$$\Delta t_{Yukawa} = \frac{\partial\delta_{Yukawa}}{\partial E} = \frac{1}{k}\frac{\partial\delta_{Yukawa}}{\partial k} \tag{4.28}$$

requires to take the derivative of the convergent Gaussian hypergeometric function, in which three of the four arguments depend on k. To this end, we make use of both representations of the function as follows:

$$\begin{aligned}&\frac{\partial}{\partial k}{}_2F_1\left(a\left(k\right),b\left(k\right);c;z\left(k\right)\right) \\ &= \left(\frac{\partial z}{\partial k}\right)\frac{{}_2F_1\left(a,b;c;z\right)}{z(1-z)}\left[\left(c-b\right)\frac{{}_2F_1\left(a,b-1;c;z\right)}{{}_2F_1\left(a,b;c;z\right)}+\left(b-c+az\right)\right] \\ &\quad+\left(\frac{\partial a}{\partial k}\right)\frac{\Gamma(c)}{\Gamma(b)\Gamma(c-b)}\int_0^1 t^{b-1}\left(1-t\right)^{c-b-1}\left(1-tz\right)^{-a} \\ &\quad\times\left[\log\left(\frac{1-t}{t\left(1-tz\right)}\right)+\psi^{(0)}(b)-\psi^{(0)}(c-b)\right]dt\end{aligned} \tag{4.29}$$

where we used that $\frac{\partial a}{\partial k} = -\frac{\partial b}{\partial k}$ and $\psi^{(0)}$ is the polygamma function.

Using this result the time delay is given as:

$$\Delta t_{Yukawa} = \frac{\delta_{Yukawa}}{k^2}\left[f(k)+g(k)-1\right] \tag{4.30}$$

with

$$f(k) = 2\eta\left[\frac{\pi}{2}+\frac{2k\mu}{4k^2+\mu^2}-\arctan\left(\frac{2k}{\mu}\right)-\frac{1}{k}\sum_{n=0}^{\infty}\frac{1}{(l+1+n)^2+\eta^2}\right]+\frac{(2l+2)\mu^2}{4k^2+\mu^2} \tag{4.31}$$

and

$$\begin{aligned} g(k) &= 2\left(l+1+i\eta\right)\left(\frac{{}_2F_1\left(l+1+i\eta,l-i\eta;2l+2;\frac{4k^2}{\mu^2+4k^2}\right)}{{}_2F_1\left(l+1+i\eta,l+1-i\eta;2l+2;\frac{4k^2}{\mu^2+4k^2}\right)}-\frac{\mu^2}{4k^2+\mu^2}\right) \\ &\quad -i\eta\int_0^1 t^{l-i\eta}\left(1-t\right)^{l+i\eta}\left(1-tz\right)^{-(l+1+i\eta)} \\ &\quad \times\left[\log\left(\frac{\left(1-t\right)\left(4k^2+\mu^2\right)}{\left(4k^2\left(1-t\right)+\mu^2\right)t}\right)-\sum_{n=0}^{\infty}\frac{2i\eta}{\left(l+1+n\right)^2+\eta^2}\right]dt \end{aligned} \tag{4.32}$$

where we have replaced the polygamma function by its respective series representation. We note that the full derivative of the hypergeometric function can alternatively be written as a series (as opposed to the integral), however the integral converges at a much higher rate than the series.

4.1.2.4 Short-range time delays for potentials with exponential decay

In this subsection we derive an analytical formula for the field-free time delay in a short range potential with exponential decay

$$V_{exp} = a_{exp}\exp[-\mu r], \tag{4.33}$$

where a_{exp} and μ are constants. The corresponding phase shift δ_{exp} has a closed form expression which can be represented in terms of the Appell F_2 function as [117]

$$\begin{aligned} \delta_{exp} &= \frac{a_{exp}(2l+2)|\Gamma(l+1+i\eta)|^2\exp[-\pi\eta]k^{2l}}{\Gamma(2l+2)\mu^{2l+3}} \\ &\quad \times F_2\left(2l+3;l+1+i\eta,l+1-i\eta;2l+2,2l+2;\frac{-2ik}{\mu};\frac{2ik}{\mu}\right) \\ &= \frac{a_{exp}(2l+2)|\Gamma(l+1+i\eta)|^2\exp[-\pi\eta]k^{2l}}{\Gamma(2l+2)\mu^{2l+3}}\left(1-\frac{2ik}{\mu}\right)^{-(l+1-i\eta)} \\ &\quad \times\left\{F_1\left(l+1+i\eta;l+2+i\eta,l+1-i\eta;2l+2;\frac{-2ik}{\mu};\frac{2ik}{2ik-\mu}\right)\right. \\ &\quad \left.-\frac{l+1-i\eta}{2l+2}\left(\frac{2ik}{2ik-\mu}\right)F_1\left(l+1+i\eta;l+2+i\eta,l+2-i\eta;2l+2;\frac{-2ik}{\mu};\frac{2ik}{2ik-\mu}\right)\right\}, \end{aligned} \tag{4.34}$$

where in the second equation we expanded the F_2 function in the more common Appell F_1 series as [117]

$$\begin{aligned} F_2\left(c+s;a,a';c,c-p;\frac{k}{h};\frac{k'}{h}\right) &= \left(1-\frac{k'}{h}\right)^{-a'}\sum_{m=0}^{s+p}\frac{(a')_m\,(-s-p)_m}{(c-p)_m\,m!}\left(1-\frac{h}{k'}\right)^{-m} \\ &\quad\times F_1\left(a;c+s-a',m+a';c;\frac{k}{h};\frac{k}{h-k'}\right), \end{aligned} \tag{4.35}$$

where

$$\begin{aligned} F_1\left(\alpha;\beta_1,\beta_2;\gamma;x,y\right) &= \sum_{m,n}^{\infty}\frac{(\alpha)_{m+n}(\beta_1)_m(\beta_2)_n}{(\gamma)_{m+n}m!n!}x^m y^n \\ &= \frac{\Gamma(\gamma)}{\Gamma(\alpha)\Gamma(\gamma-\alpha)}\int_0^1 t^{\alpha-1}(1-t)^{\gamma-\alpha-1}(1-xt)^{-\beta_1}(1-yt)^{-\beta_2}dt, \end{aligned} \tag{4.36}$$

given both as series and Euler integral representations.

Calculation of the corresponding time delay

$$\Delta t_{exp} = \frac{\partial\delta_{exp}}{\partial E} = \frac{1}{k}\frac{\partial\delta_{exp}}{\partial k} \tag{4.37}$$

requires to take the derivative of the Appell series, in which all of the arguments except γ depend on k. To this end, we make use of both representations of F_1 to get:

$$\begin{aligned} &\frac{\partial}{\partial k}F_1\left(\alpha(k);\beta_1(k),\beta_2(k);\gamma,x(k);y(k)\right) = \\ &\qquad\left(\frac{\partial x}{\partial k}\right)\frac{\alpha\beta_1}{\gamma}F_1\left(\alpha+1;\beta_1+1,\beta_2;\gamma+1;x,y\right) \\ &\quad+\left(\frac{\partial y}{\partial k}\right)\frac{\alpha\beta_2}{\gamma}F_1\left(\alpha+1;\beta_1,\beta_2+1;\gamma+1;x,y\right) \\ &\qquad+\frac{\partial\alpha}{\partial k}\frac{\Gamma(\gamma)}{\Gamma(\alpha)\Gamma(\gamma-\alpha)}\int_0^1 t^{\alpha-1}\left(1-t\right)^{\gamma-\alpha-1}\left(1-tx\right)^{-\beta_1}\left(1-ty\right)^{-\beta_2} \\ &\quad\times\left[\log\left(\frac{t(1-ty)}{(1-t)(1-tx)}\right)+\psi^{(0)}(\gamma-\alpha)-\psi^{(0)}(\alpha)\right]dt, \end{aligned} \tag{4.38}$$

where we used that $\frac{\partial\alpha}{\partial k}=\frac{\partial\beta_1}{\partial k}=-\frac{\partial\beta_2}{\partial k}$. Using this result the time delay is given by:

$$\begin{aligned} \Delta t_{exp} &= \frac{\delta_{exp}}{k}\left\{\frac{2i(l+1-i\eta)}{\mu-2ik}-\frac{i\eta}{k}\log\left(1-\frac{2i}{\mu}k\right)\right. \\ &\quad+\frac{2}{k}\left(l+\frac{\pi\eta}{2}-\frac{\eta}{k}\sum_{n=0}^{\infty}\frac{1}{(l+1+n)^2+\eta^2}\right)+\left.\frac{c_1(k)-c_2(k)-c_3(k)+c_4(k)}{c_0(k)}\right\}, \end{aligned} \tag{4.39}$$

with

$$c_0(k) = F_1\left(l+1+i\eta; l+2+i\eta, l+1-i\eta; 2l+2; \frac{-2ik}{\mu}; \frac{2ik}{2ik-\mu}\right) \tag{4.40}$$
$$-\frac{l+1-i\eta}{2l+2}\left(\frac{2ik}{2ik-\mu}\right) F_1\left(l+1+i\eta;\right.$$
$$\left. l+2+i\eta, l+2-i\eta; 2l+2; \frac{-2ik}{\mu}; \frac{2ik}{2ik-\mu}\right)$$

$$c_1(k) = \frac{2i}{(2l+2)(2ik-\mu)}\left(\frac{\mu(l+1-i\eta)}{2ik-\mu} - i\eta\right) \tag{4.41}$$
$$\times F_1\left(l+1+i\eta; l+2+i\eta, l+2-i\eta; 2l+2; \frac{-2ik}{\mu}; \frac{2ik}{2ik-\mu}\right)$$

$$c_2(k) = \frac{2i(l+1+i\eta)}{2l+2}\left\{\frac{l+2+i\eta}{\mu} F_1\left(l+2+i\eta; l+3+i\eta, \right.\right. \tag{4.42}$$
$$\left. l+1-i\eta; 2l+3; \frac{-2ik}{\mu}; \frac{2ik}{2ik-\mu}\right) + \frac{\mu(l+1+i\eta)}{(2ik-\mu)^2} F_1\left(l+2+i\eta;\right.$$
$$\left.\left. l+2+i\eta, l+2-i\eta; 2l+3; \frac{-2ik}{\mu}; \frac{2ik}{2ik-\mu}\right)\right\}$$

$$c_3(k) = \frac{4k|l+1+i\eta|^2}{(2l+2)^2(2ik-\mu)}\left\{\frac{l+2+i\eta}{\mu} F_1\left(l+2+i\eta; l+3+i\eta, \right.\right. \tag{4.43}$$
$$\left. l+2-i\eta; 2l+3; \frac{-2ik}{\mu}; \frac{2ik}{2ik-\mu}\right) + \frac{\mu(l+2-i\eta)}{(2ik-\mu)^2}$$
$$\left.\times \quad F_1\left(l+2+i\eta; l+2+i\eta, l+3-i\eta; 2l+3; \frac{-2ik}{\mu}; \frac{2ik}{2ik-\mu}\right)\right\}$$

$$c_4(k) = \delta F_1\left(l+1+i\eta; l+2+i\eta, l+1-i\eta; 2l+2; \frac{-2ik}{\mu}; \frac{2ik}{2ik-\mu}\right) \tag{4.44}$$
$$-\frac{l+1-i\eta}{2l+2}\left(\frac{2ik}{2ik-\mu}\right) \delta F_1\left(l+1+i\eta;\right.$$
$$\left. l+2+i\eta, l+2-i\eta; 2l+2; \frac{-2ik}{\mu}; \frac{2ik}{2ik-\mu}\right)$$

where

$$\delta F_1(\alpha; \beta_1, \beta_2; \gamma; x; y) = \frac{\partial\alpha}{\partial k}\frac{\Gamma(\gamma)}{\Gamma(\alpha)\Gamma(\gamma-\alpha)} \tag{4.45}$$
$$\times \quad \int_0^1 t^{\alpha-1}(1-t)^{\gamma-\alpha-1}(1-tx)^{-\beta_1}(1-ty)^{-\beta_2}$$
$$\times \quad \left[\log\left(\frac{t(1-ty)}{(1-t)(1-tx)}\right) + \psi^{(0)}(\gamma-\alpha) - \psi^{(0)}(\alpha)\right] dt.$$

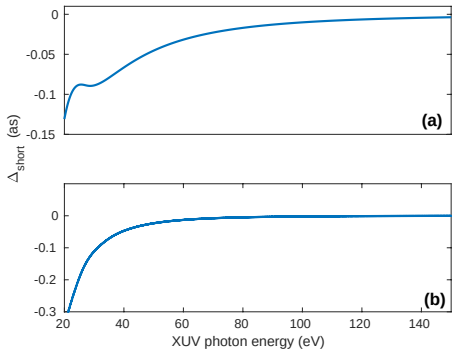

Figure 4.5: Absolute difference Δ_{short} as a function of the XUV photon energy for the contribution due to the short-range potential for (a) neon atom and (b) helium atom. Streaking laser parameters as in Fig. 4.3 (Taken from [23]).

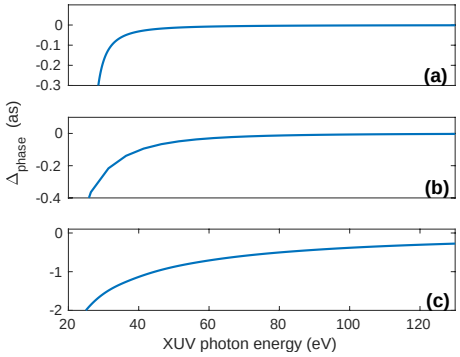

Figure 4.6: Absolute difference Δ_{phase} for photoionization of (a) neon, (b) helium and (c) hydrogen. Streaking laser parameters as in Fig. 4.3 (Taken from [23]).

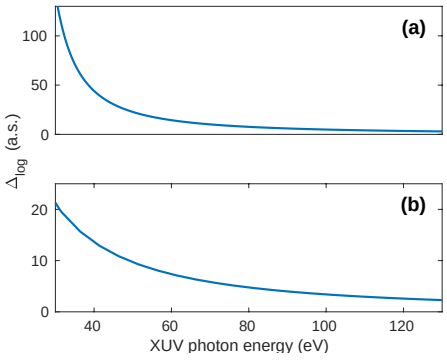

Figure 4.7: Absolute difference Δ_{log} for photoionization of (a) neon, and (b) helium. Streaking laser parameters as in Fig. 4.3 (Taken from [23]).

4.1.3 Relation to the Wigner-Smith Delay

Since we have established the usefulness of our analytical approximation, it is desirable to understand why it agrees with the streaking delay calculated in *ab-initio* simulations as a sum of Wigner-Smith and Coulomb-laser-coupling delays. We note that the field-free delay in Eq. (4.5) is split into three contributions, and may therefore study the effect of the streaking field on each of these terms. To this end, we have determined

$$\Delta_i = \sum_{j=1}^{N} \left[\frac{E_s\left(t_j\right)}{E_s\left(t_{ion}\right)} - 1 \right] \Delta t_i^{(j)} \tag{4.46}$$

for each of the three contributions ($i =$ short, phase, log). The corresponding results are shown in Figs. 4.5, 4.6 and 4.7, respectively. The comparison clearly shows that for the short-range and the Coulomb phase terms, the effect of the streaking field is significant for XUV photon energies near the threshold of photoionization only. At photoelectron energies of 10 eV or more the respective differences Δ_i are below 1 as. On the other hand the effect of the streaking field on the logarithmic term is much larger, even for photoelectron energies of several tens of eV.

Therefore, neglecting the photoelectron energies close to threshold, we can further approximate Eq. (4.5) as:

$$\begin{aligned}
\Delta t_s &= \sum_j \frac{E_s\left(t_j\right)}{E_s\left(t_i\right)} \left[\Delta t_{short}^{(j)} + \Delta t_{phase}^{(j)} + \Delta t_{log}^{(j)} \right] && (4.47)\\
&\simeq \sum_j \left[\Delta t_{short}^{(j)} + \Delta t_{phase}^{(j)} + \frac{E_s\left(t_j\right)}{E_s\left(t_i\right)} \Delta t_{log}^{(j)} \right] && (4.48)\\
&= \Delta t_{short} + \Delta t_{phase} + \sum_j \frac{E_s\left(t_j\right)}{E_s\left(t_i\right)} \Delta t_{log}^{(j)} && (4.49)\\
&= \Delta t_{WS} + \Delta t_{CLC} && (4.50)
\end{aligned}$$

where $\Delta t_{WS} = \Delta t_{short} + \Delta t_{phase}$ represents the well-known Wigner-Smith time delay for short range potentials, while $\Delta t_{CLC} = \sum_j \frac{E_s(t_j)}{E_s(t_i)} \Delta t_{log}^{(j)}$ can be interpreted as the Coulomb-laser-coupling term often used in the analysis of streaking time delays. Indeed, as shown in Fig. 4.8, the present estimates for Δt_{CLC} are in good agreement with another analytical estimate $\Delta t_{CLC} = Z[2 - \ln(E_{asym} T_{IR})]/(2E_{asym})^{3/2}$ [26], where T_{IR} is the streaking field period.

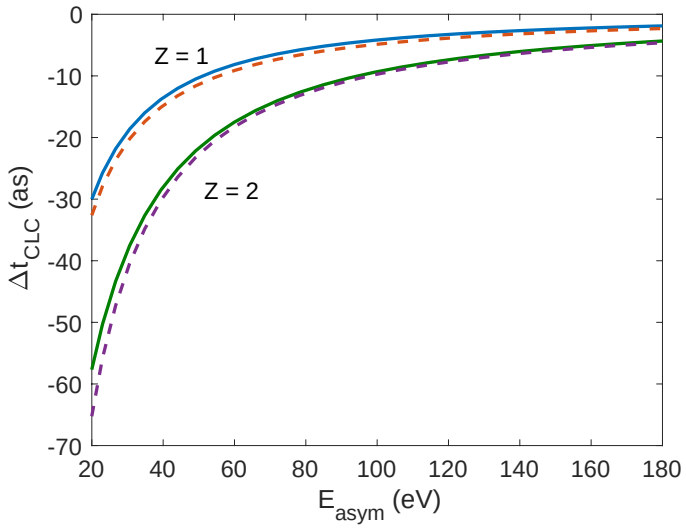

Figure 4.8: Comparison of present analytical estimates (solid lines) for Δt_{CLC} with those of an alternative analytical approximation (dashed lines, [26]). Streaking laser parameters as in Fig. 4.3 (Taken from [23]).

4.2 Application of analytical streaking formula

In the previous section we derived an analytical formula for the streaking time delay. As shown, the formula is useful to obtain accurate estimates of the delay in a short period of time, and furthermore provides new insights into the separation of the time delay into the WS time delay and a Coulomb-laser-coupling term. However, in consideration of the good agreement with numerical results and the efficiency to obtain predictions, the formula can also be easily applied to different situations, and hence help to analyze other theoretical proposals and/or potential effects on the streaking time delay. In this section we illustrate these opportunities for two examples.

4.2.1 Application to and analysis of recent theoretical proposal

Earlier this year, Kiesewetter *et al.* [27] performed a RABBITT experiment (c.f., section 1.3.1.2) using a novel analysis method, which they deemed RABBITT+, to extract the coarse characteristics of the binding potential of helium, neon, and argon atoms. They assume a simple pseudo-potential in their method, which allows for the modeling of the energy transfer occuring in an XUV-pump NIR-probe attosecond experiment, given that the electron has propagated over a large portion of the potential within the first half-cycle of the streaking field after ionization.

The pseudo-potential model from Ref. [27] is shown in Fig. 4.9. In the model, the electron appears in the continuum at time $t = 0$ in the presence of the streaking field with period T. In the first quarter cycle of the field after liberation into the continuum ($0 \leq t \leq T/4$), the photoelectron has an average momentum $\mathcal{P}_1$ and is assumed to experience a linear change in momentum along the laser polarization direction. The momentum is then constant at $\mathcal{P}_2$ until after next field maximum at $t = T/2 + t_0$, where the momentum assumes its asymptotic value p_0. The photoemission time delay is defined as the energy derivative of the phase of the wave packet in this model potential as compared to the phase of the corresponding free-particle (c.f., Eq. (2.1)). The wavepacket for the free particle by definition experiences no net energy transfer from a potential, and according to this model always has momentum p_0 throughout the propagation. It follows that the amount

of time delay accumulated during propagation should be directly related to the amount of energy transfer occuring within the first half cycle of streaking field after the liberation of the electron in the continuum. Since it has been shown that RABBITT and streaking measurements provide equivalent information concerning the time delay, the model by Kiesewetter *et al.* implies that the observed (streaking or RABBITT) time delay is essentially determined within one half cycle of the streaking field.

This model thus goes further then the interpretation provided by Su *et al.* [92] (c.f., section 2.2.2). While Su *et al.* showed that the streaking delay is accumulated until the end of the streaking pulse, Kiesewetter *et al.* suggest that the streaking delay is already within a good approximation of its final value after only a quarter or half cycle of the streaking pulse. We cannot test the pseudo-potential model of Ref. [27] directly, however our analytical formula allows us to test this last statement. To this end, we analyze the sum in Eq. (4.5) as a function of time t_j during the electron's propagation, until the sum achieves its final value at the end of the streaking pulse. In order to see to what end the assumption in Ref. [27] holds, concerning the time range over which the streaking delay is effectively obtained, we find at what times the sum has converged within 10% and 1% of its final value (denoted as $T_{10\%}$ and $T_{1\%}$ respectively), and compare these times to $T/4$ and $T/2$. For all calculations, the time of ionization t_{ion} is chosen to be the peak of the streaking pulse:

$$\mathbf{E}_s(t) = \hat{\mathbf{z}} E_0 \sin^2\left(\frac{\pi t}{\tau}\right) \sin\left(\frac{2\pi c}{\lambda_s} t + \phi_{\text{CEP}}\right). \tag{4.51}$$

In Figure 4.10 we present the results of such a calculation for four different streaking field wavelengths and for ionization of hydrogen atom. For each streaking field wavelength, we plot the sum (4.5) as a function of time for seven different XUV central frequencies. In addition, we show the times $T/4$ and $T/2$ (dashed vertical lines) in order to compare with the assumptions of the model by Kiesewetter *et al.* For each XUV central frequency considered, the times $T_{1\%}$ (circles) and $T_{10\%}$ (stars) are indicated.

We see that the general behavior of Eq. (4.5) as a function of t_j can be decomposed into

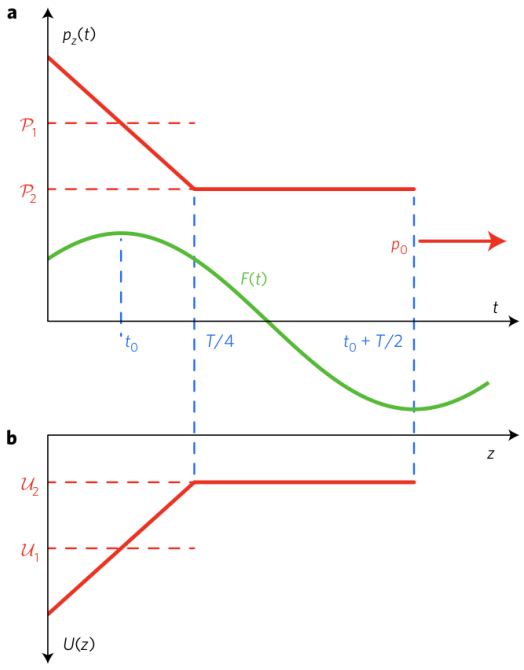

Figure 4.9: Pseudopotential as suggested in the work by Kiesewetter et al. [27]. (a) An electron is ejected at time $t = 0$ in the presence of a weak NIR field $F(t)$ with period T. For $0 \leq t \leq T/4$, the electron has an average momentum of $\mathcal{P}_1$ and experiences a constant restoring force along the laser polarization direction. For $t > T/4$, its momentum is modeled as constant at $\mathcal{P}_2$ until after the next field maximum at $T/2 + t_0$. After the net energy transfer has been established, the photoelectron assumes its asymptotic momentum p_0. (b) Illustration of the corresponding spatial dependence of the pseudo-potential along the field polarization. (Taken from Ref. [27])

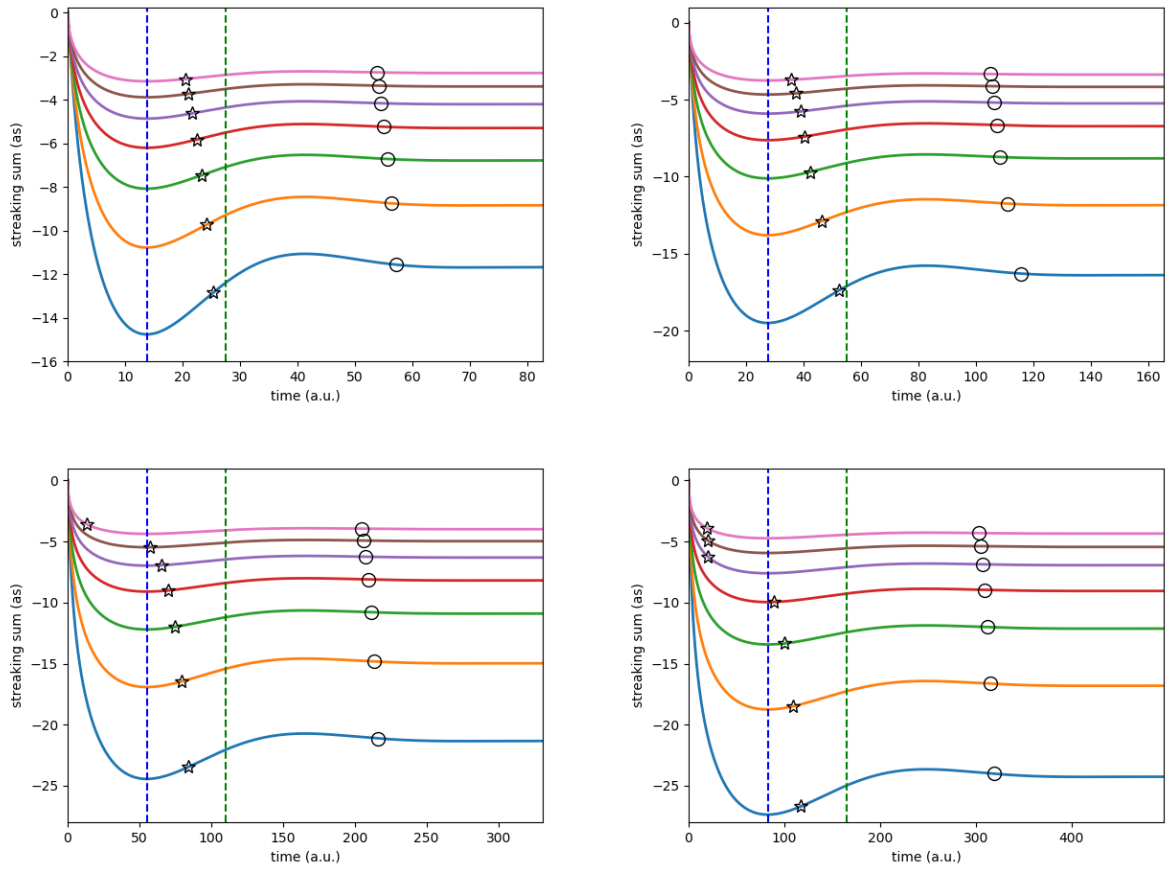

Figure 4.10: Eq. (4.5) shown as a function of time t_j for streaking wavelengths $\lambda_s = 400$ nm (a), 800 nm (b), 1600 nm (c), and 2400 nm (d). For each panel, the results are shown for final electron kinetic energies corresponding to XUV central frequencies of $\omega = 44.22$ eV (blue), 55.27 eV (orange), 68.03 eV (green), 82.48 eV (red), 98.64 (purple) eV, 116.49 eV (brown), and 136.05 eV (pink). The times $T_{10\%}$ and $T_{1\%}$ (as described in the text) are shown with stars and circles respectively. For all simulations shown, a 3 cycle streaking pulse of intensity $I_s = 1 \times 10^{12}$ W/cm^2 is used.

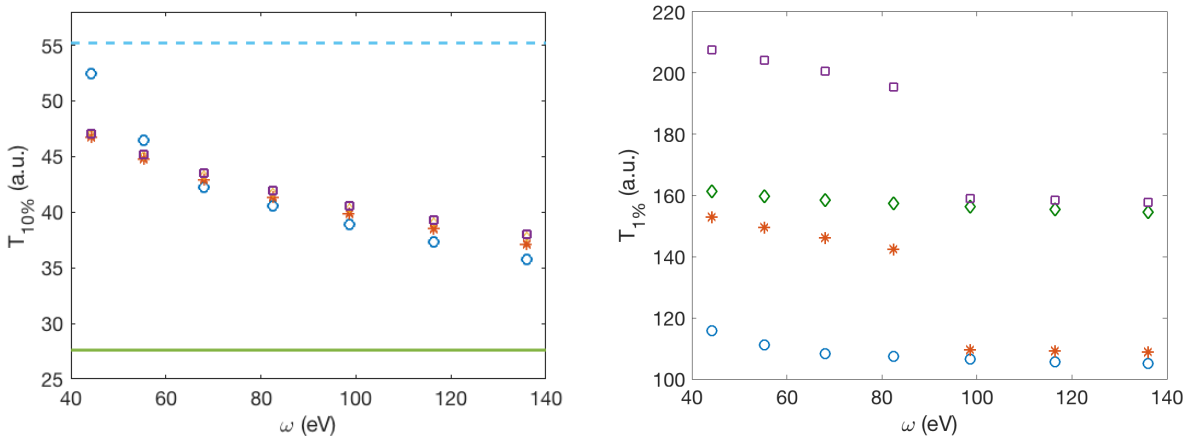

Figure 4.11: The times $T_{10\%}$ (left) and $T_{1\%}$ (right) shown as a function of XUV central frequency for different pulse durations; $N_s = 3$ cycles (circles), $N_s = 4$ cycles (stars), $N_s = 5$ cycles (diamonds), and $N_s = 6$ cycles (squares). For the case of $T_{10\%}$, we further show $T/2$ (dashed light blue) and $T/4$ (solid green). The same streaking pulse intensity as for the results in Fig. 4.10 is used for all calculations.

two regions. As also assumed by the pseudo-potential model, in the first region $0 \leq t \leq T/4$ the electron feels the influence of the Coulomb potential most strongly, and accordingly we see a sharp increase in the magnitude of the time delay. Beyond $t = T/4$ the field changes and then oscillates until the end of the pulse. Consequently, the accumulated streaking time delay as a function of time oscillates as well. The magnitude of the oscillation decreases due to two reasons: (i) the amplitude of the electric field decreases (reducing the weight of the field-free time delays) and (ii) the Coulomb potential decreases in strength (reducing the magnitude of the field-free time delays). Thus, overall we observe a damped oscillation of the streaking time delay towards its final value at the end of the pulse.

As we can see from the positioning of the stars and circles vs. the dashed vertical lines, $T_{10\%} < T/2$ and $T_{1\%} > T/2$ for all of the streaking wavelengths and ionizing photon energies considered. Furthermore, for almost every single case considered, $T/4 < T_{10\%} < T/2$. The cases where this does not hold (appears as a "jump" in the results) are for the longer streaking wavelengths considered, specifically for the highest XUV photon energy in the case of 1600 nm, and the three largest XUV photon energies considered in the case of 2400 nm. For all four cases, the values of $T_{10\%}$ are much smaller than $T/4$, and we can understand the reasoning for these outliers as follows. In each of these cases, the kinetic energy of the photoelectron is relatively large, and therefore the electron propagates away from the core of the potential quickly. Therefore, by the time the sign of the field changes, due to the large decrease in the magnitude of the Coulomb potential, the terms $\Delta t_{ff}^{(j)}$ are sufficiently small such that they do not contribute significantly to the total sum. Therefore Δt_s approaches within 10% of the final value much faster as compared to the cases of less energetic photoelectrons. In addition, we see this effect appear only for longer streaking wavelengths by similar reasoning. That is, the streaking field changes sign after a longer period of time, during which the influence of the Coulomb potential has decreased significantly. This argument is further supported by $T_{10\%}$ and $T_{1\%}$ both decreasing as a function of XUV photon energy for all streaking pulse wavelengths considered. In further regards to $T_{1\%}$, we note that for no case considered does this time fall between $T/4$ and $T/2$, and generally is reached towards the end of the streaking pulse.

Additionally, we present in Fig. 4.11 the results for $T_{10\%}$ and $T_{1\%}$ as a function of XUV central frequency using an 800 nm streaking field, now for four different streaking pulse durations. We furthermore show $T/2$ and $T/4$ as horizontal lines in the Figure for $T_{10\%}$. We see that $T_{10\%}$ does not vary by more than a few atomic units with respect to pulse duration, which implies that our observation $T_{10\%} < T/2$ is robust with respect to pulse duration. In contrast, $T_{1\%}$ varies with pulse duration by at least 40 a.u. for every XUV central frequency shown. This demonstrates that $T_{1\%}$ is reached before the end of the pulse, but only once the oscillations of the field have a sufficiently negligible influence on the propagation of the electron, which in general happens long after the electron has propagated over half a period of the field. Therefore, from our analysis we can conclude that the prediction of Kiesewetter *et al.* regarding the streaking delay being accumulated within the first half cycle of the streaking field after liberation of the electron into the continuum is accurate to within about 10% of the total streaking delay. In certain cases where the streaking field has a longer wavelength or when the photoelectron has a relatively high kinetic energy, this level of accuracy can be achieved at times earlier than $T/2$.

4.2.2 Influence of the attochirp on attosecond streaking delays[2]

As mentioned in Chapter 1, only a fraction of the relative delay of 21 as, measured in [17], has been accounted for by theory [19, 25, 86, 118], which has generated much of the interest in the interpretation of attosecond time delay measurements. It was recently suggested by Keller and co-workers [119] that the streaking time delay and other time measurements such as RABBITT [120, 121] may depend on the chirp of the ionizing attosecond XUV pulse. In the case of streaking this was related to the presumption that different times for the transition of the photoelectron into the continuum during the interaction with the XUV pulse would correspond to different asymptotic kinetic energies of the electron. Previous theoretical studies focused on the analysis of the method of measurement itself, namely the retrieval of the Wigner-Smith time delay from streaked energy

[2] The results of this section are also presented in C. Goldsmith, A. Jaroń-Becker, and A. Becker, J. Phys. B **51**, 025601 (2018).

spectra using chirped pulses [91, 120]. It was demonstrated that the spectrogram itself is sensitive to the attochirp of the XUV pulse and for chirped pulses the retrieved time delays may depend on the accuracy of the retrieval algorithm and/or the central momentum approximation, in which the momentum of the photoelectron is approximated by the center momentum of the unstreaked spectrum. Here, we show an application of the analytical formula derived in the previous section in order to provide a complimentary study of the attochirp effect on the attosecond streaking time delay. Instead of focusing on the experimental methods of extracting the WS time delays, we study how the streaking time delay itself, intrinsic to the photoionization process in the superposition of the two pulses, depends on the chirp of the attosecond XUV pulse.

4.2.2.1 Accounting for the attochirp in the model

In the previous section we showed that for asymptotic photoelectron energies E_{asym} not too close to threshold the effect of the streaking field on the short-range and Coulomb phase parts of the field-free delay are negligible and we can approximate the streaking delay via

$$\Delta t_s(\omega, t_i) = \Delta t_{WS}(\omega) + \sum_{j=1}^{N} \frac{E_s\left(t_j\right)}{E_s\left(t_i\right)} \Delta t_{log}^{(j)}(\omega), \tag{4.52}$$

where $\Delta t_{WS} = \Delta t_{short} + \Delta t_{phase}$ represents the Wigner-Smith time delay [68–70] and the second term can be interpreted as the Coulomb-laser-coupling term often part of the commonly used analysis of the streaking time delay [22, 24–26, 64, 73, 75, 76, 84–91, 114]. The Wigner-Smith time delay can be either estimated analytically (see previous section) or determined using literature values based on advanced calculations (e.g., [29, 79]). In the calculations presented below we have used the data for the Wigner-Smith time delay obtained by Kheifets [29]. The logarithmic term can be calculated analytically using

$$\Delta t_{log}^{(j)}(\omega) = Z \left[\frac{1 - \ln\left(2k_{j+1}r_{j+1}\right)}{k_{j+1}^3} - \frac{1 - \ln\left(2k_j r_j\right)}{k_j^3} \right] \tag{4.53}$$

along the method outlined in Section 4.1.

In Figure 4.12 we present results of the analytical estimates for the streaking time delay for photoemission from a neon atom ((a) $2p$ and (b) $2s$) and argon atom ((c) $3p$ and (d) $3s$) as a

function of XUV central frequency. In the calculations we assumed a Gaussian XUV laser pulse with a FWHM pulse duration of $\tau_{FWHM} = 40$ as and used a streaking pulse with $\sin^2$ envelope consisting of 3 cycles. The maxima of the two fields were set to coincide in time.

We furthermore compare estimates for the streaking delays for three different times of transition of the photoelectron into the continuum during the XUV laser pulse, i.e., we show delays for the cases $t_i = -20$ as, $t_i = 0$ as, and $t_i = 20$ as. This comparison shows that the streaking time delay does not have a significant dependence upon the time of transition. This is due to the fact the streaking pulse does not vary much over the interval of 40 as. In addition, the estimates of the delay for the neon atom are in good agreement with results from *ab-initio* simulations (diamonds, [25]). It is important to note however that the current model formula does not provide an improvement concerning the discrepancies between the experimental data of [17] and theoretical predictions. Since we discussed in Section 4.1 that the predictions of the model formula are expected [23, 93] to be less reliable for XUV central frequencies near the ionization threshold, we restrict ourselves in the frequency range of the attosecond pulse in the analysis below.

While the time delays for Ne and Ar($3s$) increase quite smoothly as a function of the XUV frequency, while a pronounced minimum appears around the Cooper minimum for Ar($3p$). The minimum arises from the WS time delay and is related to the change of sign in the dipole matrix element [29, 79, 122–124].

In order to study the effect of the attochirp using Eq. (4.52), we determine the expectation value of the streaking time delay in a chirped laser pulse as

$$\langle \Delta t_s \rangle (\omega_0, b) = \int d\omega \int dt_i P(\omega, \omega_0, t_i, b) \, \Delta t_s(\omega, t_i), \tag{4.54}$$

where $P(\omega, \omega_0, t_i, b)$ is the probability distribution for a transition at a certain frequency ω at a given time t_i; ω_0 is the central frequency of the pulse, and b is a parameter which describes the chirp of the pulse (see Eq. (4.58) below). Since the dependence of $\Delta t_s(\omega, t_i)$ on t_i during the interaction with the XUV pulse is negligible (see Fig. 4.12), we can further approximate

$$\langle \Delta t_s \rangle (\omega_0, b) \simeq \int d\omega \Delta t_s(\omega) \, P_{avg}(\omega, \omega_0, b), \tag{4.55}$$

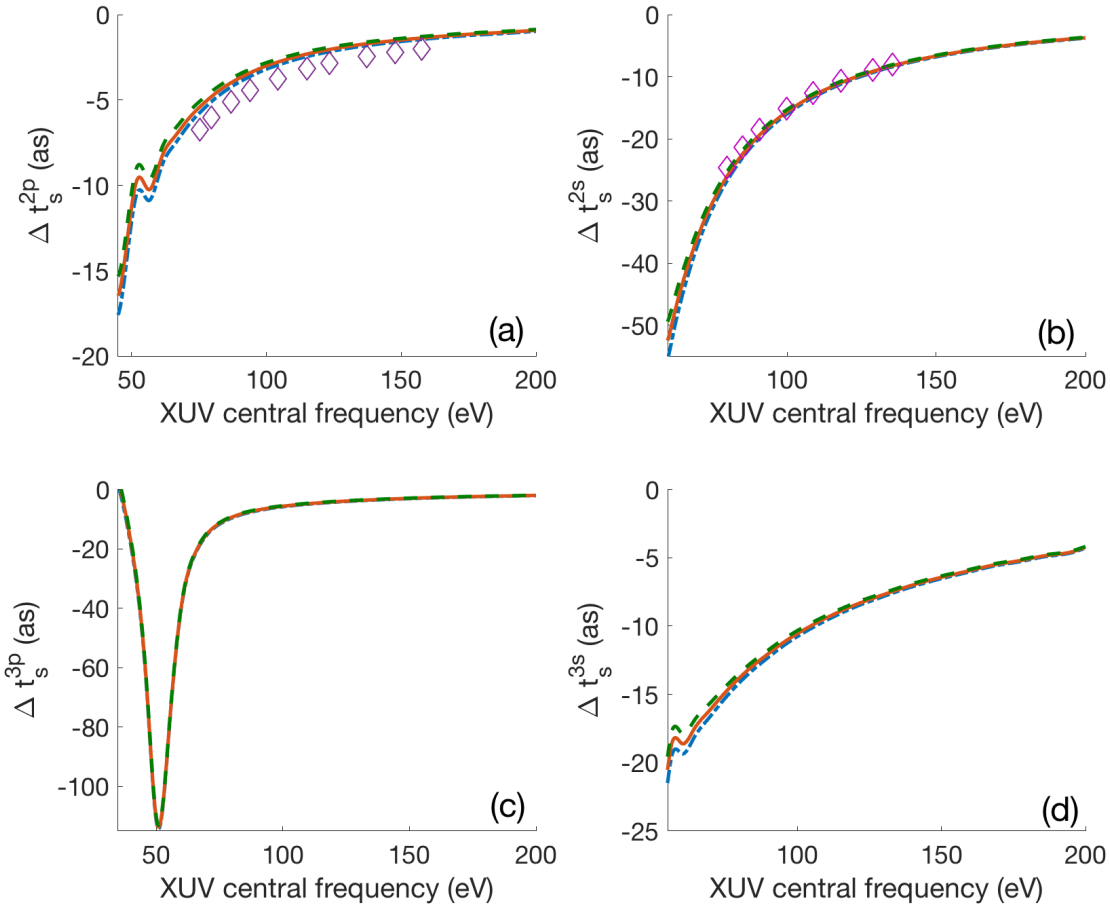

Figure 4.12: Estimates of the streaking delay for Neon ((a) $2p$, (b) $2s$) and Argon ((c) $3p$, (d) $3s$) given by Eq. (4.52), as a function of the central XUV frequency for times of the transition in the continuum, $t_i = -\tau_{FWHM}/2$ (dash-dotted line), $t_i = 0$ (solid line), and $t_i = \tau_{FWHM}/2$ (dashed line) are compared. Also shown are results from ab-initio calculations (diamonds), [25]. In all calculations a streaking pulse of wavelength $\lambda_s = 800$ nm, $\sin^2$-envelope consisting of 3 cycles, and peak intensity $I_s = 1 \times 10^{12}$ W/cm^2 has been considered (Taken from [28]).

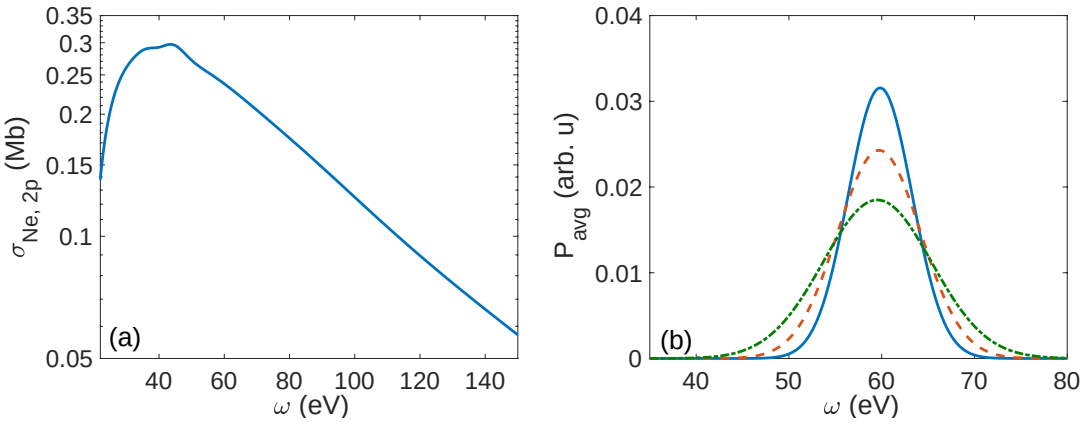

Figure 4.13: (a) Neon $2p$ photoionization cross section [29] and time averaged probability for (b) $\omega_0 = 60$ eV. The chirp is taken to be $b = 0$ eV/fs (solid line), $b = 15$ eV/fs (dashed line), and $b = 25$ eV/fs (dash-dotted) and $\tau = 450$ as (Taken from [28]).

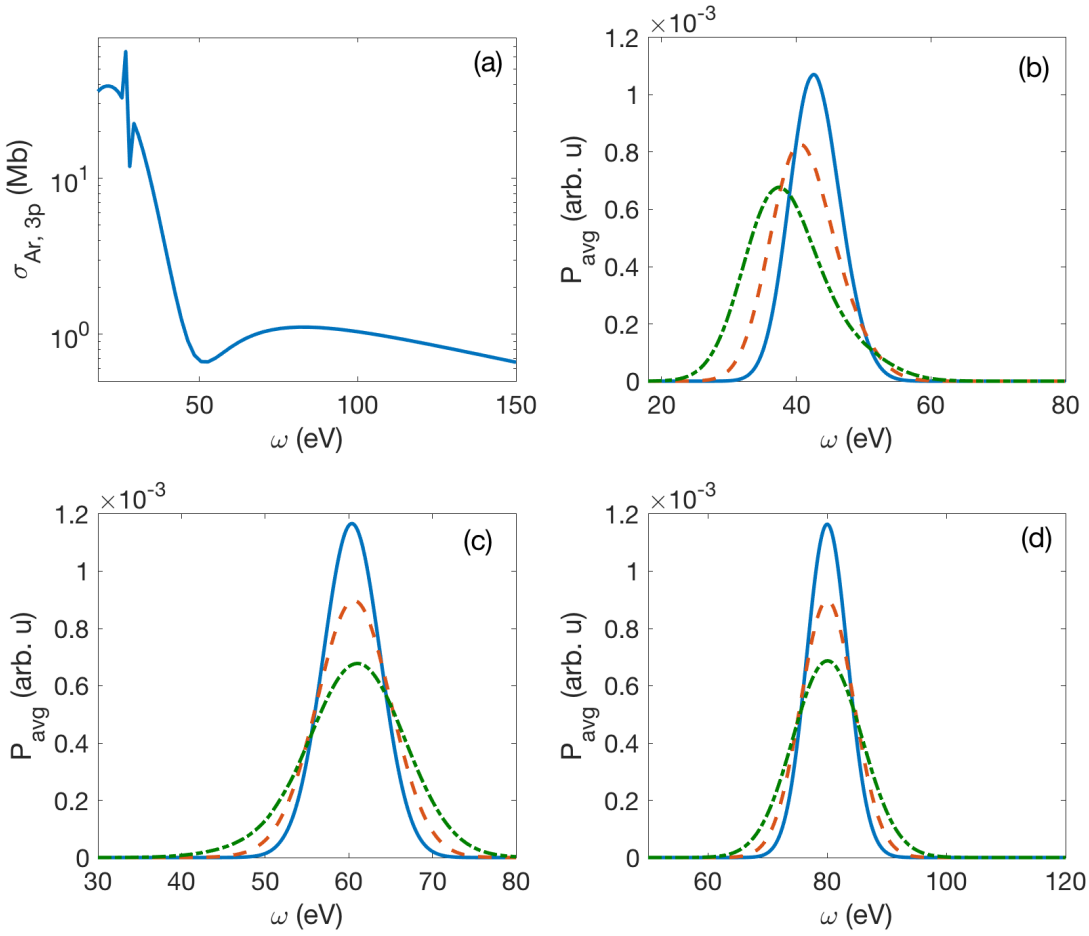

Figure 4.14: Same as Fig. 4.13 but for (a) Argon $3p$ photoionization cross-section [29]; time averaged probability for (b) $\omega_0 = 45$ eV, (c) $\omega_0 = 60$ eV, and (d) $\omega_0 = 80$ eV (Taken from [28]).

where $P_{avg}(\omega, \omega_0, b)$ is the time averaged probability distribution. In our studies below we consider a linear chirped laser Gaussian pulse for which [125]

$$P_{avg}(\omega, \omega_0, b) = N\sigma(\omega) \int_{-\infty}^{\infty} g(\omega, \omega_0, t, b)\, U(t) dt, \tag{4.56}$$

where $\sigma(\omega)$ is the photoionization cross-section and

$$U(t) = \exp\left[\frac{-(16\ln 2)^2 t^2}{\tau^2}\right] \tag{4.57}$$

is the temporal intensity distribution with $\tau/8\sqrt{\ln(2)}$ being the FWHM pulse duration of the Gaussian pulse. The instantaneous spectral distribution of the pulse is

$$g(\omega, \omega_0, t, b) = \exp\left[-\frac{(\omega - \omega_0 - bt)^2}{\gamma^2/4\ln 2}\right], \tag{4.58}$$

with $\gamma^2 = \Gamma^2 - \frac{\tau^2 b^2}{4}$, where $\Gamma = \frac{1}{\tau}\left[64(\ln 2)^2 + \tau^4 b^2\right]^{1/2}$ and N is a normalization factor.

For an unchirped pulse (i.e., $b = 0$) the instantaneous spectral distribution g is time-independent and P_{avg} is given by the photoionization cross section weighted by a Gaussian distribution centered about the central frequency (ω_0) (solid lines in Figs 4.13 (b) and 4.14(b)-(d)). For photoemission from the $2p$ state of Neon (and the s-states, not shown), the cross section varies rather smoothly as a function of XUV frequency (Fig. 4.13(a)). Consequently, a temporal chirp in the pulse causes a broader and less intense time averaged probability distribution while the position of the maximum in the distribution does not shift significantly, independent of the central frequency ω_0 (Fig. 4.13(b)).

In contrast in the case of Ar($3p$) (Fig. 4.14) the variation in the photoionization cross section near the frequency ω_C for the Cooper minimum leads to a shift of the maximum of P_{avg}. For central frequencies which are slightly below ω_C (Fig. 4.14(b)) the frequency at which the maximum appears is less than ω_0, and decreases as the chirp of the pulse increases due to the rapid decrease of the photoionization cross section. We note that the effect of Fano resonances below 30 eV (see Fig. 4.14(a)) on the present results cannot be further analyzed, since the resonances appear outside the frequency range which is applicable for our model formula. At frequencies just above ω_C (Fig.

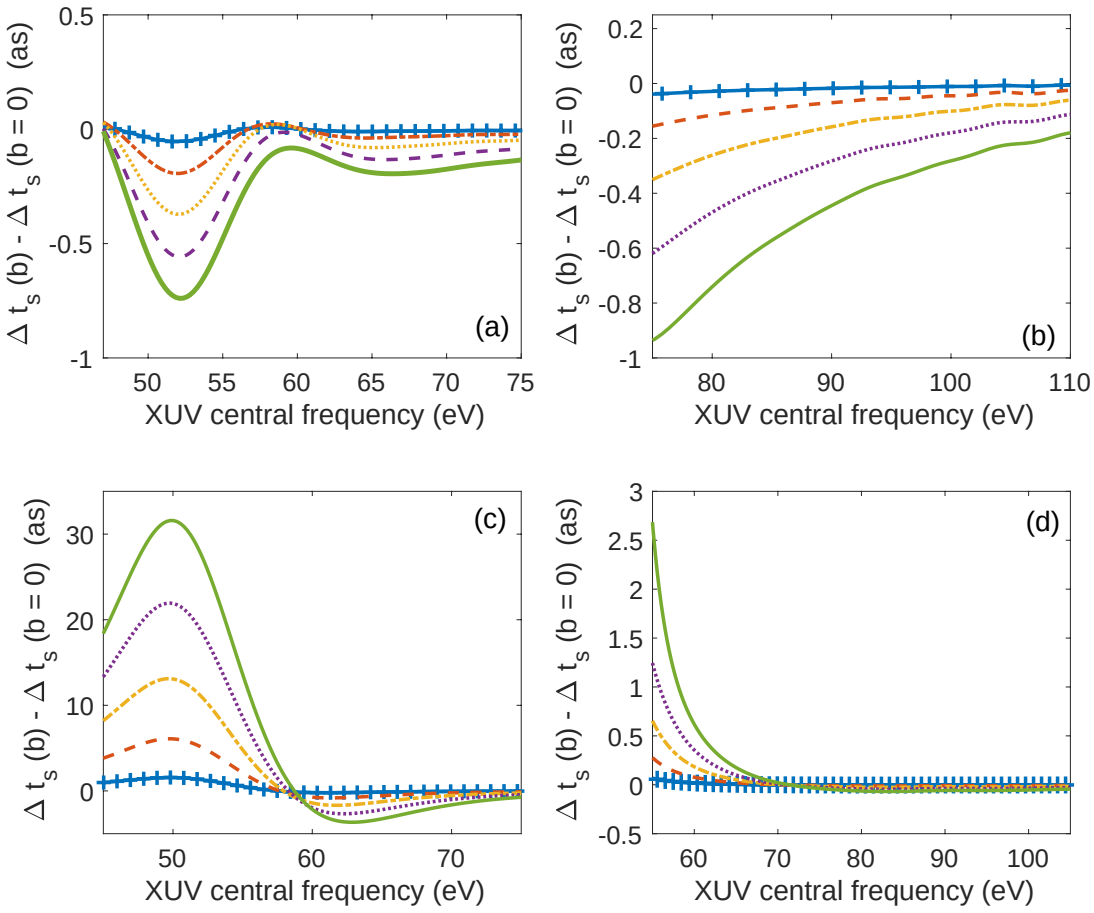

Figure 4.15: Change in streaking time delay for photoionization of Ne from $2p$ (a) and $2s$ (b) shells and of Ar from $3p$ (c) and $3s$ (d) in chirped laser pulses (with respect to an unchirped pulse) for $b = 5$ eV/fs (line with plus signs), $b = 10$ eV/fs (dashed), $b = 15$ eV/fs (dash-dot), $b = 20$ eV/fs (dotted), and $b = 25$ eV/fs (solid) (Taken from [28]).

4.14(c)), we observe a small effect of the chirp due to the increase of the photoionization cross section. On the other hand for frequencies significantly above ω_C (Fig. 4.14(d)), the distribution of P_{avg} for Ar($3p$) changes similar to the case of Ne($2p$) as well as the s-states.

We also note that the analytical formula allows us to predict that for very large chirp

$$\lim_{b\to\infty} g\left(\omega,\omega_0,t_i,b\right) = \exp\left[\frac{-16\ln\left(2\right)}{3}\left(\frac{t}{\tau}\right)^2\right], \tag{4.59}$$

while the time averaged probability distribution is given by

$$\lim_{b\to\infty} P_{avg}\left(\omega,\omega_0,b\right) = N\sigma(\omega)\frac{\tau}{8}\sqrt{\frac{3\pi}{\ln 2}} \tag{4.60}$$

and the expectation value of the streaking delay, Eq. (4.55), becomes independent of the central frequency ω_0. As test calculations have shown however, this limit is only reached approximately for unrealistic values of the chirp parameter b of a few hundred eV/fs.

4.2.2.2 Effect of the Cooper minimum in Argon

As can be seen from Eq. (4.55) the effect of the attochirp on the streaking time delay arises from the convolution of the time averaged probability distribution $P_{avg}(\omega,\omega_0,b)$ and the variation of the delay with XUV photon energy ω. In Fig. 4.15 we present predictions for the difference between the streaking time delays obtained in a chirped pulse and an unchirped pulse for (a) Ne($2p$), (b) Ne($2s$) as well as for (c) Ar($3p$) and (d) Ar($3s$). In each case, the difference increases as the chirp parameter b increases, and we observe variations as a function of XUV central frequency. For Neon the effect is smaller than 1 as over the whole range of frequencies, even for the largest attochirp considered ($b = 25$ eV/fs). This is due to the rather smooth variation as a function of frequency of both the streaking time delay and the photoionization cross section for photoemission from the $2p$ and $2s$ subshells.

According to our results in the previous section, the influence of the chirp is much larger when the time delay and the cross section change rapidly as a function of the laser frequency. Consequently, we observe significant changes of up to a couple of tens of attoseconds in the streaking

time delay at small XUV frequencies for photoemission from the $3p$ shell in Ar, with a pronounced maximum centered near the Cooper minimum (Fig. 4.15(c)). This confirms previous expectations [79] that time delays and related effects are most pronounced near a Cooper minimum. The effect is larger at frequencies lower than ω_C than for $\omega > \omega_C$, in agreement with the results for P_{avg} in Fig. 4.14. In contrast, the changes in the streaking time delay for ionization of Ar($3s$) as well as of Ar($3p$) at frequencies significantly above the Cooper minimum are as small as for photoionization of Ne atom. We have further analyzed the impact of the two contributions to the streaking delay, namely Wigner-Smith term and Coulomb-laser coupling term, on the change observed in Fig. 4.15. The data in Fig. 4.16 show that the significant change for the Ar($3p$) photoemission primarily results from the Wigner-Smith contribution (Fig. 4.16(a)). This is due to the fact that the Wigner-Smith term varies more rapidly than the Coulomb-laser coupling term around the Cooper minimum.

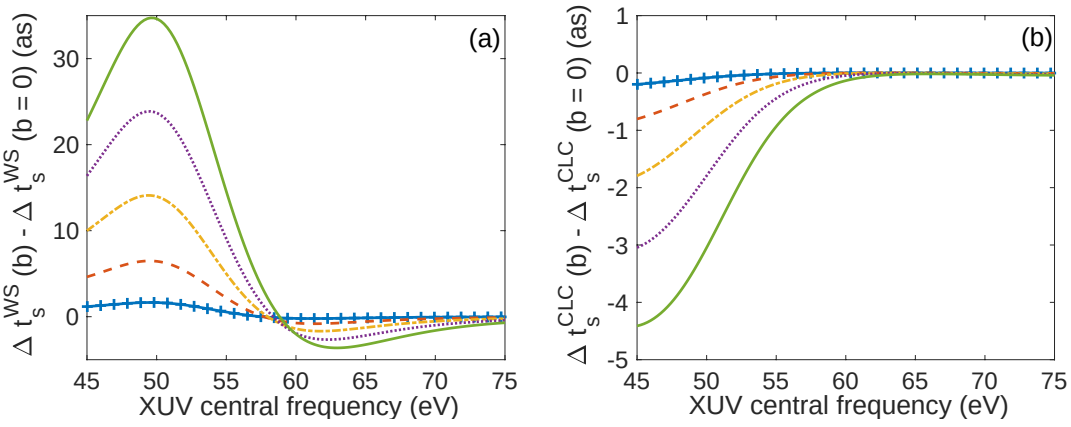

Figure 4.16: Comparison of the contributions from the (a) Wigner-Smith and (b) Coulomb-laser coupling terms for the change in the streaking delay for photoionization of Ar from $3p$ shell. Lines and symbols as in Fig. 4.15(c) (Taken from [28]).

Finally, we present in Fig. 4.17 the relative time delays for photoemission from the different subshells in (a) Ne and (b) Ar as a function of the chirp parameter b. As expected, in the case of Ne it is found that an attochirp has a negligible effect on the intrinsic value of the relative streaking time delay. In particular, the relative time delay at 100 eV remains at about 12-13 as independent of the value of the chirp parameter, and thus cannot account for the discrepancy between theoretical

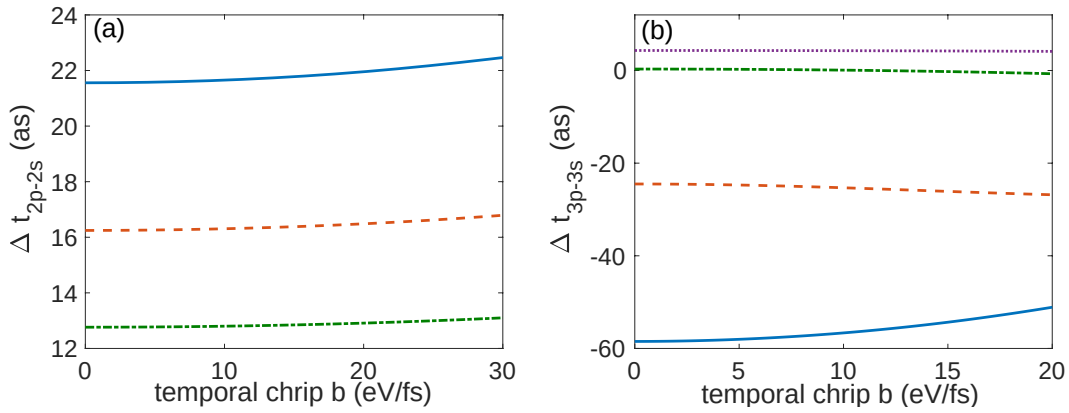

Figure 4.17: Difference of streaking time delays for photoemission (a) from $2p$ and $2s$ in Neon at XUV central frequencies of 80 eV (solid), 90 eV (dashed), and 100 eV (dash-dotted) and (b) from $3p$ and $3s$ in Argon at XUV central frequencies of 55 eV (solid), 60 eV (dashed), 70 eV (dash-dot), and 80 eV (dotted) as a function of the chirp parameter b (Taken from [28]).

predictions and the experiment of [17]. On the other hand, for argon the relative delay can vary by several attoseconds for XUV laser frequencies near the Cooper minimum.

Chapter 5

Absorption time delays in resonant and non-resonant two-photon ionization

In recent studies, it has been suggested to apply the attosecond streaking principle to temporally resolve electron dynamics in two-photon resonant ionization [20, 21, 67, 80] and double ionization [90]. These studies showed that the time delay between the absorption of two photons may be retrieved from the streaking or RABBITT time delays, and that this delay can be controlled by parameters of the applied XUV laser, such as pulse duration in the case of Ref. [20], and central frequency as shown in Ref. [67]. Further analysis is necessary to understand whether or not such results can be used for advanced time-resolved measurements.

As discussed in section 2.3, Su and coworkers [20] found that for a two-photon ionization process, an additional time-delay, called the absorption delay Δt_{abs}, may occur that is not accounted for by the streaking time delay obtained in the continuum (as in the case of one-photon ionization, see also Chapter 4). Furthermore, Δt_{abs} is observed to be non-zero in the case of resonant two-photon ionization only [16]. As the absorption delay depends on the energy level structure of the target, it may open a route towards probing attosecond dynamics in atoms and molecules. In this Chapter, we show under which conditions the absorption delay can be approximated using time-dependent perturbation theory. We then demonstrate how our perturbative model can be used to illuminate dynamics.

In section 5.1, we derive an analytical formula that captures the absorption delay through an isolated resonance, and compare to the predictions of TDSE simulations. Furthermore, we show how the inclusion of an additional resonance improves agreement with TDSE calculations. Then, in

section 5.2 we analyze how the behavior of the absorption delay is modified in cases where multiple intermediate resonances are within the bandwidth of the XUV pulse. In addition, we discuss how the streaking results are related to observables in attosecond transient absorption spectroscopy [14], which is an alternative method for time-resolved measurements. Finally, in section 5.3 we show results of the absorption delay in the simplest molecule H_2^+ using a one-dimensional model.

5.1 Two-photon ionization through an isolated resonance[1]

The work by Su *et al.* [20] proposed that the time delay in streaking of two-photon ionization can be parametrized by:

$$\Delta t_s^{(2\omega)} = \Delta t_{abs} + \Delta t_c, \tag{5.1}$$

where Δt_c is the time delay accumulated by the photoelectron during propagation in the continuum after absorbing two photons, and Δt_{abs} is the delay which contains temporal information about the transition of the electron from the ground state into the continuum (see section 2.3). We note that in the context of this Chapter, the two-photon streaking delay $\Delta t_s^{(2\omega)}$ in Eq. (5.1) corresponds to the two-photon process, and therefore we refer to it as simply Δt_s for the rest of this thesis.

In the previous Chapter, we have considered analysis of the second term in the sum (5.1), i.e., the continuum delay. We saw that the continuum delay could be accounted for via classical simulations or the sum (4.5). Indeed, in one photon ionization processes being probed by attosecond streaking, the continuum delay accounts for the entirety of the observed streaking delay. In this respect, the liberation of the electron into the continuum is instantaneous within the resolution of the simulation.

Through our analysis below, we derive an analytical formula for the absorption delay which in the case of an isolated resonance shows the strong linear dependence of the absorption delay upon the XUV pulse duration previously seen in the TDSE simulations of Ref. [20] (c.f., section 2.3). Furthermore, our analysis reveals a dependence on the detuning of the central frequency of the

[1] The results of this section are also presented in C. Goldsmith, J. Su, A. Jaroń-Becker, and A. Becker, J. Phys. B: At. Mol. Opt. Phys. **51**, 155602 (2018).

XUV pulse from the resonance. In addition, we estimate the effect of the inclusion of an additional intermediate state.

5.1.1 Time-dependent perturbation theory analysis

We wish to model a two-photon ionization process, starting from an initial bound state $|i\rangle$ into a final continuum state $|f\rangle$ with respect to parameters of the ionizing attosecond pulse. Assuming the ionizing pulse is sufficiently weak, the amplitude c_{fi} can be written within second order perturbation theory (c.f., section 3.1.3) as [126]:

$$c_{fi}(\omega) = \sum\!\!\!\!\!\!\int_m \int_{-\infty}^{\infty} \mu_{fm} e^{i\delta_f t} E(t) \int_{-\infty}^{t} \mu_{mi} e^{i\delta_m t'} E(t') dt' dt \,, \tag{5.2}$$

where μ_{jk} is the transition dipole moment between states $|j\rangle$ and $|k\rangle$, $E(t)$ is the field envelope and ω is the central frequency of the XUV pulse, $\delta_f = E_f - E_m - \omega$, and $\delta_m = E_m - E_i - \omega$ with $E_f = E_i + 2\omega$. The sum with integral represents the expansion of the intermediate state over all field-free states of the target atom or molecule. Eq. (5.2) can be solved analytically for a Gaussian field envelope $E(t) = E_0 e^{-t^2/2T^2}$ [126]

$$c_{fi} = \pi E_0^2 T^2 \sum\!\!\!\!\!\!\int_m \mu_{fm}\mu_{mi} \left[e^{-\delta_m^2 T^2} - i\frac{2}{\sqrt{\pi}} F(\delta_m T) \right], \tag{5.3}$$

where $F(x) = e^{-x^2} \int_0^x e^{-t^2} dt$ is Dawson's integral. Assuming that the bandwidth of the attosecond pulse predominantly covers only one intermediate (resonant) state $|r\rangle$ we further approximate [126]

$$c_{fi} = \pi E_0^2 T^2 \left[\mu_{fr}\mu_{ri} e^{-\delta_r^2 T^2} - i\frac{2}{\sqrt{\pi}} \sum\!\!\!\!\!\!\int_m \mu_{fm}\mu_{mi} F(\delta_m T) \right], \tag{5.4}$$

since the Gaussian term decays quickly as a function of detuning and therefore contributes for the resonant state only.

The absorption time delay is related to the phase of the two-photon transition amplitude as

$$\phi_f = \arg c_{fi} = \arctan\left[\frac{\mathrm{Im}(c_{fi})}{\mathrm{Re}(c_{fi})} \right]. \tag{5.5}$$

Before proceeding, we note that it is only the absolute value of the dipoles which are of concern. The dipole matrix element $\mu_{fm} = |\mu_{fm}| e^{i\theta_{fm}}$, involving the transition into the continuum state, has

a phase θ_{fm} whose derivative with respect to energy is merely the widely discussed Wigner-Smith delay. This delay, and therefore the corresponding phase, is accounted for in the continuum delay Δt_c, or equivalently does not contribute to the absorption delay. On the other hand, the dipole matrix elements μ_{mi} between bound states are, in general, real. Therefore, we proceed to get the phase related to the absorption time delay as follows:

$$\begin{aligned} \phi_{abs} &= \arctan\left[-\frac{2}{\sqrt{\pi}}\sum\!\!\!\!\!\!\int_m \frac{|\mu_{fm}\mu_{mi}|\,F\left(\delta_m T\right)}{|\mu_{fr}\mu_{ri}|\,e^{-\delta_r^2 T^2}}\right] && (5.6)\\ &= -\arctan\left[\frac{2}{\sqrt{\pi}}\left(e^{\delta_r^2 T^2}F\left(\delta_r T\right)+\sum\!\!\!\!\!\!\int_{m\neq r}\frac{|\mu_{fm}\mu_{mi}|\,F\left(\delta_m T\right)}{|\mu_{fr}\mu_{ri}|\,e^{-\delta_r^2 T^2}}\right)\right], && (5.7)\end{aligned}$$

where we have separated the contribution by the resonant state from those by the other states. Assuming that the latter contributions are small, we make a Taylor expansion by considering the closest (dipole allowed) non-resonant state $|b\rangle$ in the sum over m only and obtain:

$$\phi_{abs} = \phi_{abs}^{(res)} + \phi_{abs}^{(non-res)} \tag{5.8}$$

with

$$\begin{aligned} \phi_{abs}^{(res)} &= -\arctan\left[\frac{2}{\sqrt{\pi}}e^{\delta_r^2 T^2}F\left(\delta_r T\right)\right] && (5.9)\\ \phi_{abs}^{(non-res)} &= -\frac{a_b(\delta_b,\delta_r,T)}{1+\mathrm{erfi}^2(\delta_r T)}+\frac{2}{\sqrt{\pi}}\frac{a_b^2(\delta_b,\delta_r,T)e^{\delta_r^2 T^2}F\left(\delta_r T\right)}{\left(1+\mathrm{erfi}^2(\delta_r T)\right)^2} && (5.10)\end{aligned}$$

where

$$a_b(\delta_b,\delta_r,T) = \frac{|\mu_{fb}\mu_{bi}|}{|\mu_{fr}\mu_{ri}|}F\left(\delta_b T\right)e^{\delta_r^2 T^2}, \tag{5.11}$$

$\mathrm{erfi}(\delta_r T) = \frac{2}{\sqrt{\pi}}F(\delta_r T)e^{\delta_r^2 T^2}$, and the above expansion was made about $a_b = 0$. The absorption time delay is given by the spectral derivative of ϕ_{abs}:

$$\begin{aligned} \Delta t_{abs}\left(\delta_r,\delta_b,T\right) &= \Delta t_{abs}^{(res)}\left(\delta_r,T\right)+\Delta t_{abs}^{(non-res)}\left(\delta_b,\delta_r,T\right)\\ &= \frac{\partial\phi_{abs}^{(res)}}{\partial E_f}+\frac{\partial\phi_{abs}^{(non-res)}}{\partial E_f} = \frac{\partial\delta_r}{\partial E_f}\frac{\partial\phi_{abs}^{(res)}}{\partial\delta_r}+\frac{\partial\phi_{abs}^{(non-res)}}{\partial E_f}\\ &= \frac{T}{\sqrt{\pi}}\frac{e^{(\delta_r T)^2}}{1+\mathrm{erfi}^2\left(\delta_r T\right)}+\frac{\partial\phi_{abs}^{(non-res)}}{\partial E_f}. && (5.12)\end{aligned}$$

where we used $\delta_r = E_r - E_i - \omega = E_r - \frac{1}{2}(E_i + E_f)$. The first term is the contribution from the resonant intermediate state and the second term is the approximate correction due to the closest

(dipole allowed) non-resonant state. In the present analysis we obtained the latter correction by calculating the corresponding phase and performing the derivative numerically. As we will show below, the correction term is typically small and we neglected it in the main part of our analysis (unless mentioned otherwise).

Eq. (5.12) shows that the absorption delay $\Delta t_{abs}^{(res)}(\delta_r, T)$ depends on the detuning from the resonance δ_r and the duration of the ionizing laser pulse T, while it is independent of other laser or target parameters. In Fig. 5.1, we present the predictions for $\Delta t_{abs}^{(res)}(\delta_r, T)$ as a function of δ_r and T. As one would expect, for large durations (i.e., small energy bandwidth of the pulse) the absorption delay is non-negligible for small detunings from the resonance only, while the detuning range over which $\Delta t_{abs}^{(res)}(\delta_r, T)$ is significant increases with a decrease of the pulse duration.

5.1.2 Comparison with numerical simulations

In order to test if the predictions of the model formula, Eq. (5.12), are reliable we have performed numerical simulations of a streaking measurement (see section 3.3 for details). Since according to our analytical model the general trends for the absorption time delay through a single intermediate resonance (i.e. when $\Delta t_{abs}^{(non-res)} \simeq 0$) are independent of the specific form of the atomic potential, we have chosen a model system for the main part of our analysis.

To this end, we have considered a one-dimensional (1D) potential:

$$V(x) = -\frac{Z}{\sqrt{x^2 + a}}\,, \tag{5.13}$$

where Z is the effective charge and a is a soft-core parameter. Choosing $Z = 3.0$ and $a = 0.15$, the energies of the three lowest states are $E_1 = -5.32$, $E_2 = -2.31$, and $E_3 = -1.30$ a.u. These eigenstates are well separated such that one can selectively study the two-photon absorption into the continuum via a single intermediate resonance. In order to keep the duration of the XUV pulse shorter than the oscillation period of the streaking pulse, we have used a 3-cycle streaking field of 2400 nm in wavelength with $I_s = 1.0 \times 10^{11}$ W/cm^2 and $\phi_s = -\pi/2$. In order to test the predictions of the perturbative analysis in case of nearby additional states, we have also made use of previously

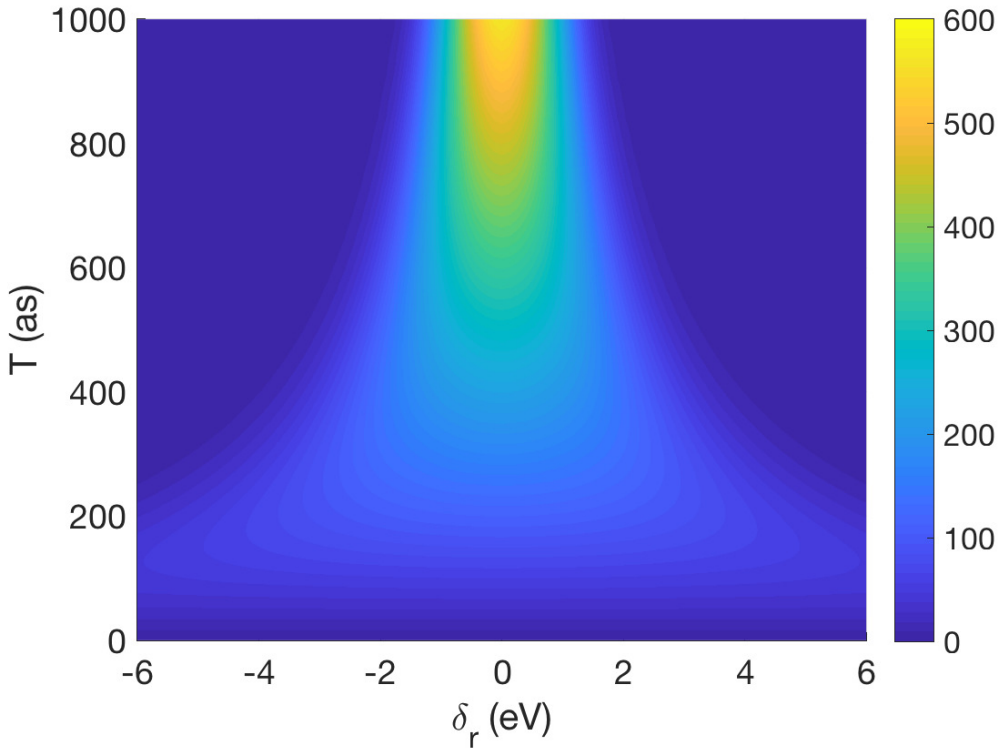

Figure 5.1: Resonant contribution to the absorption delay $\Delta t_{abs}^{(res)}$(in attoseconds) as a function of detuning δ_r and pulse duration T (Taken from Ref. [1]).

obtained data for the absorption delay for resonant two-photon ionization of the helium atom [20].

To obtain the absorption time delay from the numerical results for the streaking delay we need to retrieve the contribution due to the continuum time delay. As discussed in Chapters 2 and 4, several techniques are known to obtain Δt_c from the well-studied streaking of photoionization. One of these techniques makes use of the fact that the propagation in the continuum can be often well described by classical analysis [73]. We have therefore used a classical trajectory method to determine the continuum time delay in this particular instance. To this end, we consider the Newton equation for the dynamics of the electron in the field generated by the Coulomb potential of the residual ion and the streaking field of the linearly polarized laser. The corresponding differential equation has been solved using the fourth-order Runge–Kutta method. As initial conditions, we have chosen the most probable position of the electron in the ground state of the potential and the initial momentum of the electron due to the absorption of a photon in the Coulomb potential. Alternatively, one can sample the initial conditions in Monte-Carlo calculations [73]. The delay between the XUV pulse and streaking pulse corresponds to the instant of the appearance of the photoelectron in the continuum during the streaking pulse. We have therefore varied this initial time instant to obtain a classical streaking trace in terms of the classical final momentum. The continuum time delay Δt_c can be then retrieved from this classical streaking trace in the same way as Δt_s from the quantum streaking simulations. For further details of this classical trajectory calculations we refer to [92]. An example of the procedure is shown in Fig. 5.2 for a resonant two-photon ionization of the model system. The absorption time delay is then given as $\Delta t_{abs} = \Delta t_s - \Delta t_c$ (c.f., Eq. (5.1)).

Considering resonant two-photon ionization at the central frequency of the pulse, i.e. detuning $\delta_r = 0$, we have performed streaking simulations using the model potential and an ionizing pulse with $\omega = 3.01 = E_2 - E_1$. In Fig. 5.3 (a), we present the numerically determined absorption time delay $\Delta t_{abs} = \Delta t_s - \Delta t_c$ (circles) as a function of the pulse duration T. The numerical results are compared with the theoretical model predictions for the absorption time delay Δt_{abs} (Eq. (5.12), solid line), including both resonant and non-resonant contributions, and the resonant contribution

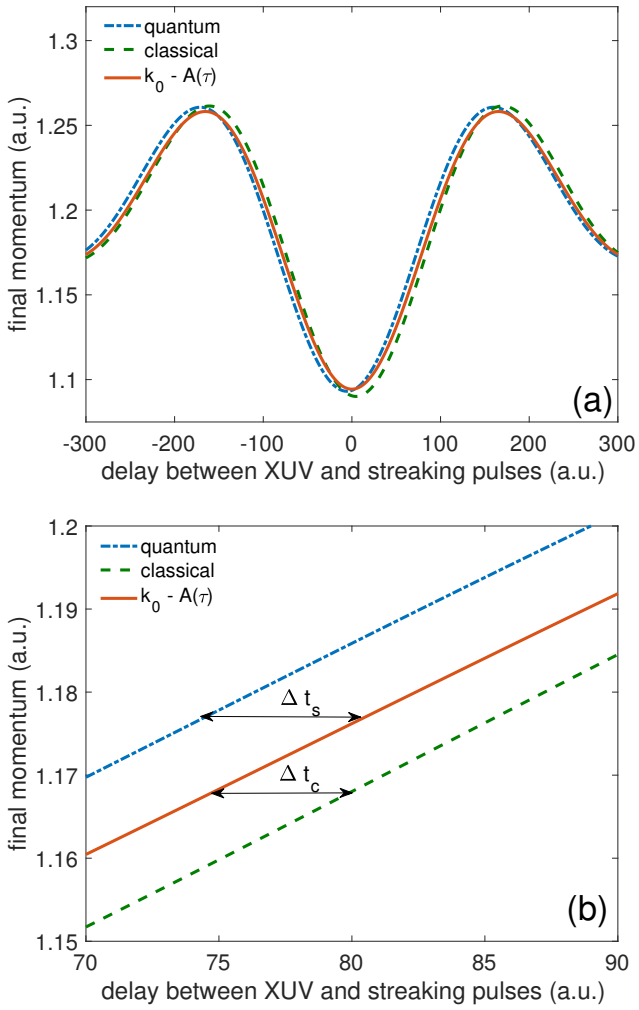

Figure 5.2: Three streaking traces for a resonant two-photon ionization from numerical streaking simulations (blue solid curve), classical electron trajectory calculations (green dashed line), and the reference free-particle streaking formula $k_f^{(\mathrm{free})}(t_i) = k_0 - A_s(t_i)$ (red dashed-dotted curve). Panel (b) is an enlargement of the traces in panel (a) to show the streaking (Δt_s) and continuum (Δt_c) time delay. Laser parameters used in the simulations are: $I_{\mathrm{XUV}} = 1.0 \times 10^{13}$ W/cm^2, $\omega_{\mathrm{XUV}} = 81.81$ eV, $T = 550$ as, and $\phi_{\mathrm{XUV}} = -\pi/2$; $I_s = 1.0 \times 10^{11}$ W/cm^2, $\lambda_s = 2400$ nm, $N_s = 3$, and $\phi_{\mathrm{s}} = -\pi/2$ (Taken from Ref. [1]).

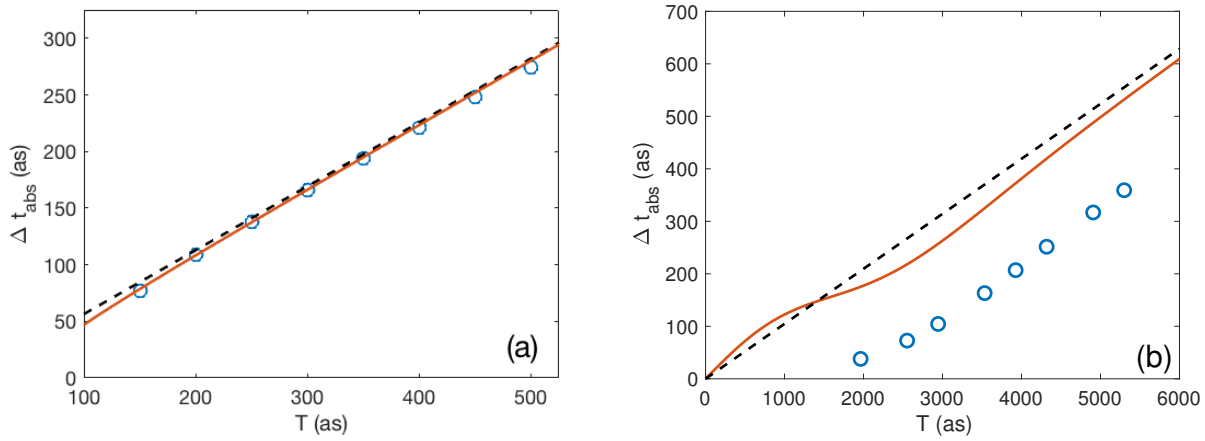

Figure 5.3: Absorption time delay from numerical simulations (blue circles) and model predictions for $\Delta t_{abs}^{(res)} + \Delta t_{abs}^{(non-res)}$ (red solid line) and $\Delta t_{abs}^{(res)}$ (black dashed line) as a function of pulse duration for a Gaussian XUV pulse tuned into resonance with the first excited state of (a) the model system and (b) helium atom (data for numerical simulations taken from [20]). Laser parameters: $I_{\mathrm{XUV}} = 1.0 \times 10^{13}$ W/cm^2 (resonant), $\phi_{\mathrm{XUV}} = -\pi/2$; $I_s = 1.0 \times 10^{11}$ W/cm^2, $\lambda_s = 2400$ nm, $N_s = 3$, and $\phi_{\mathrm{s}} = -\pi/2$ (Taken from Ref. [1]).

$\Delta t_{abs}^{(res)}$ (dashed line) only. Note that in the case of resonant central frequency $\lim_{\delta_r \to 0} \Delta t_{abs}^{(res)} = \frac{T}{\sqrt{\pi}}$. The absorption time delays extracted from the numerical simulations indeed reproduce the linear dependence on the pulse duration as predicted by perturbation theory. Although the correction from the non-resonant contribution is small (c.f., solid line vs. dashed line), its inclusion further improves the agreement between predictions and numerical data.

In Fig. 5.3 (b), we compare predictions from perturbation theory to TDSE simulations of the absorption delay in 3D helium atom taken from [20]. In the calculations of the dipole matrix elements for the helium atom, we used bound state wavefunctions in the Coulomb field of an effective charge $Z_e = 27/16$ and the plane wave approximation for the continuum states. The comparison reveals that while the numerical results qualitatively reproduce the linear dependence of the absorption time delay on the pulse duration, there is an almost constant offset. This offset was interpreted before as the influence of the streaking field on the resonant $2p$ state [20], which is not taken into account in the present perturbation model. In the present comparison we however also observe that in the case of the helium atom consideration of the non-resonant correction term (c.f., solid line vs. dashed line) has a much larger effect than for the model system (Fig. 5.3 (a)), where the states are more separated in energy. Thus, it is likely that in the case of helium atom further improvement may require to consider more than one non-resonant state in the analysis, which is beyond the scope of the present section.

As mentioned above, in our perturbative model analysis of the absorption time delay we have neglected the influence of the streaking pulse. In case of the model system with the transition through a strongly bound resonant state, this assumption is confirmed by the results of our numerical simulations. For example, in Table 5.1 it is shown that, although the streaking and continuum time delays (not shown) vary with a change of either the wavelength or the intensity of the streaking pulse, the variation of the extracted absorption time delays is less than 5 as. This implies that by accurate determination of the continuum time delay one is able to obtain the absorption time delay, independent of the parameters of the applied streaking pulse, if the intermediate resonant state is well isolated from other states and the effect of the streaking field on the intermediate state

T	$\lambda_s = 2400$ $I_s = 10^{11}$	$\lambda_s = 3200$ $I_s = 10^{11}$	$\lambda_s = 4800$ $I_s = 10^{10}$	$\Delta t_{abs}^{(res)}$	$\Delta t_{abs}^{(res)} + \Delta t_{abs}^{(non-res)}$
250.0	137.79	134.34	140.08	141.05	137.40
350.0	193.47	190.52	195.96	197.47	194.86
450.0	247.66	244.87	250.49	253.89	251.86

Table 5.1: Results of simulations for the absorption delay (in as) in the model system as a function of the pulse length T (in as) of a two-photon resonantly ionizing pulse and streaking pulses at different wavelengths λ (in nm), intensities I (in W/cm^2). Also shown are the predictions $\Delta t_{abs}^{(res)} = T/\sqrt{\pi}$ (in as) and $\Delta t_{abs}^{(res)} + \Delta t_{abs}^{(non-res)}$ (in as) from perturbation theory (Taken from Ref. [1]).

is negligible. In the following section, we shall see that this last assumption in particular is not always justified.

For the case of a well-isolated intermediate state, as in the case of the 1D model system, we have also considered how $\Delta t_{abs}^{(res)}$ changes for small detunings, i.e. $\delta_r \neq 0$. The predictions of the perturbative analysis for the absorption delay $\Delta t_{abs}^{(res)}$ as a function of pulse duration T for various detunings δ_r are shown in Fig. 5.4. We note that for the 1D model system, the contribution $\Delta t_{abs}^{(non-res)}$ is less than 10 as even for the largest δ_r considered, as can be seen in Fig. 5.5.

One can see that for small T, or more generally small product $\delta_r T$, the absorption delay approximately depends linearly on the pulse duration, as in the on-resonant case. This can be understood by expanding the model formula in a Taylor series for $x = \delta_r T$ about $x = 0$:

$$\Delta t_{abs}^{(res)}(x) \simeq \frac{1}{\sqrt{\pi}\delta_r}\left[x + \left(1 - \frac{4}{\pi}\right)x^3 + O\left(x^5\right)\right]. \tag{5.14}$$

For a given detuning δ_r and sufficiently small T, the first term of the expansion is dominant and the absorption delay is approximately determined by $\Delta t_{abs}^{(res)} = T/\sqrt{\pi}$. Physically, this corresponds to the situation that the frequency for the resonant transition lies well within the bandwidth of the ionizing laser pulse.

On the other hand, we see that the model prediction for the absorption delay $\Delta t_{abs}^{(res)}$ goes to zero for large pulse durations, independent of the detuning δ_r. Physically, this corresponds to the situation that the energy bandwidth of the pulse is sufficiently small and the contributions at the resonant frequency become negligible. In this case the streaking delay is determined by the

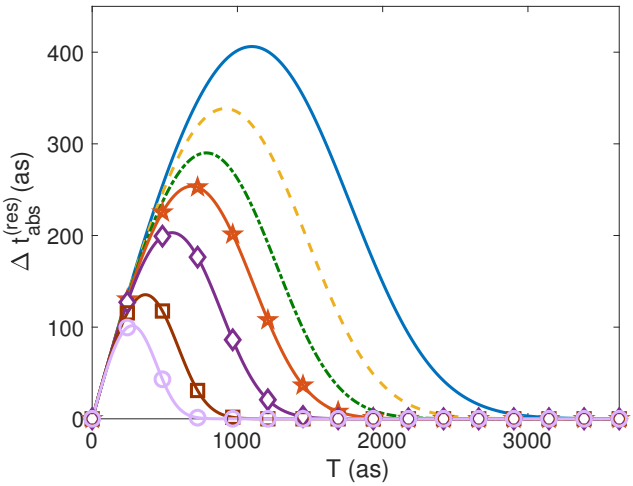

Figure 5.4: Absorption delay $\Delta t_{abs}^{(res)}$ as a function of pulse duration for detunings $\delta_r = 0.68$ eV (solid line), 0.82 eV (dashed line), 0.95 eV (dash-dot line), 1.09 eV (stars), 1.36 eV (diamonds), 2.04 eV (boxes), and 2.72 eV (circles) (Taken from Ref. [1]).

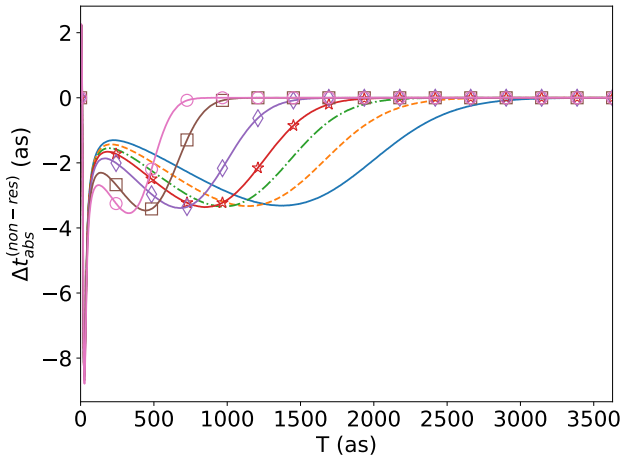

Figure 5.5: Absorption delay $\Delta t_{abs}^{(non-res)}$ as a function of pulse duration for detunings $\delta_r = 0.68$ eV (solid line), 0.82 eV (dashed line), 0.95 eV (dash-dot line), 1.09 eV (stars), 1.36 eV (diamonds), 2.04 eV (boxes), and 2.72 eV (circles).

continuum time delay only, as discussed before [20]. This can be also shown by taking the limit of $\Delta t_{abs}^{(res)}$ for $T \to \infty$ as:

$$\lim_{T\to\infty} \Delta t_{abs}^{(res)}(\delta_r, T) = \frac{1}{\sqrt{\pi}} \lim_{T\to\infty} \frac{\frac{d}{dT}\left(Te^{\delta_r^2 T^2}\right)}{\frac{d}{dT}\left(1+\mathrm{erfi}^2(\delta_r T)\right)} \tag{5.15}$$

$$= \lim_{T\to\infty} \frac{1+2\delta_r^2 T^2}{2\delta_r \,\mathrm{erfi}(\delta_r T)} \tag{5.16}$$

$$= \lim_{T\to\infty} \frac{\delta_r T^2}{\mathrm{erfi}(\delta_r T)} = 0 \tag{5.17}$$

where we have repeatedly applied L'Hospital's rule.

Besides these limits, further analysis of $\Delta t_{abs}^{(res)}$ reveals another interesting dependence: If the detuning δ_r is inversely proportional to the pulse duration T, i.e. $\delta_r T = \text{const.}$, the absorption delay depends linearly on T. Since the half-width of a pulse with Gaussian envelope is given by $\Delta\omega_{1/2} = \frac{\sqrt{2\ln 2}}{T}$, we therefore expect $\Delta t_{abs}^{(res)} \propto T$ for $\delta_r = \Delta\omega_{1/2}$. In Fig. 5.6, we present results of TDSE simulations for the streaking, continuum and absorption delay as a function of the pulse duration for this case using the 1D model system. Indeed, the linear relationship of $\Delta t_{abs}^{(res)}$ on the pulse duration is captured by the ab-initio calculations of Δt_{abs} for pulse durations $T > 200$ as. For shorter pulse durations we observe a deviation from the linear trend, since the corresponding broad bandwidth of the pulse covers more than one resonance. In the next section, we take the next steps towards analyzing the role of multiple resonances.

5.2 Absorption delay in the case of multiple resonances

As seen in the previous section, when more than one resonance is within the bandwidth of the ionizing pulse, the analytical solution presented is no longer well applicable. While Eq. (5.3) is still valid, the result will depend on the accurate calculation of more than one dipole moment. Thus, the sum has to be calculated numerically and the dipole moments must be calculated to good approximation.

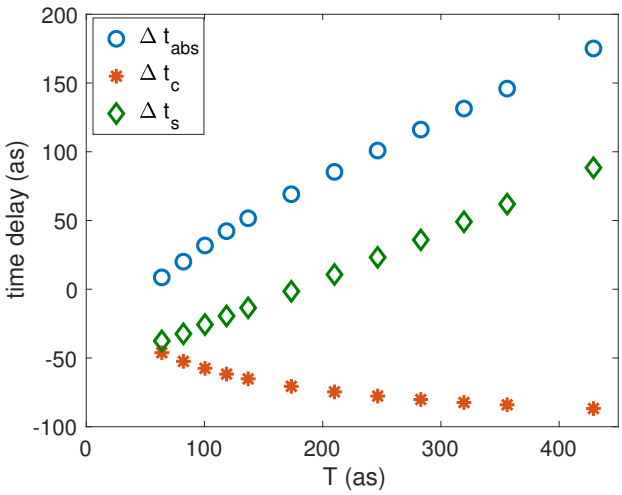

Figure 5.6: Absorption delay as a function of XUV pulse duration, for a detuning chosen such that the resonance is at FWHM of the XUV pulse (Taken from Ref. [1]).

5.2.1 Analysis using model potentials

In order to be able to clearly distinguish between the regimes of isolated resonances and overlapping resonances, we use the same 1D model potential as in the previous section, Eq. (5.13), but with $Z = 3$ and $\alpha = 1.0$. The lowest six states for this potential are $E_0 = -2.336$, $E_1 = -1.360$, $E_2 = -0.8697$, $E_3 = -0.5946$, $E_4 = -0.4303$, and $E_5 = -0.3244$ a.u. Thus, the first two allowed transitions from the ground state are well separated as compared to a typical bandwidth ($\simeq 0.5$ a.u. in the case of Ref. [17]) of the ionizing pulse. This is desirable as it allows us to still observe the effects of individual resonances, while analyzing additional effects in the regions where the resonances overlap.

Using this potential, we solved for the absorption delay across a central frequency range 1.5–2.1 a.u., which spans frequencies resonant with the 3rd excited state to the 5th excited state. In order to calculate the absorption delay in TDSE simulations, we again use $\Delta t_{abs} = \Delta t_s - \Delta t_c$. The streaking delay Δt_s is obtained from the streaking trace for two-photon ionization. For the determination of the continuum delay Δt_c, instead of using classical simulations as in the previous section, we use the other method described in section 3.3, which is to solve the TDSE for the corresponding one-photon ionization process. The results of the TDSE simulations for the streaking time delay, the continuum time delay, and the obtained absorption time delay are shown in Fig 5.7 (a), where we see three peaks in the absorption delay. The first peak is relatively broad and is centered around the central frequency resonant with the third excited state ($\omega_{30} = 1.7414$ a.u., see section 3.1.3.2 for notation), and the peak corresponding to the highest energy is centered around the fifth excited state resonant frequency ($\omega_{50} = 2.0116$ a.u.). Another sharp peak appears in the vicinity of the fourth excited state resonance ($\omega_{40} = 1.9057$ a.u.).

To gain insights into these features, we first use the model calculations of the absorption delay based on time-dependent perturbation theory which was presented in the previous section. Here, we are required by Eq. (5.3) to know the transition dipole moments corresponding to every contributing state. As a further approximation however, we assume that the dipole moments

between the bound states and the continuum are approximately constant in this energy regime, and use the dipole moment products as fitting parameters for the absorption delay. In this sense, we fit the result of second order perturbation theory to the TDSE calculations, with the dipole moment product $\mu_{fj}\mu_{ji}$ for different intermediate states $|j\rangle$ as constant complex numbers. The results of this fit are shown in Fig. 5.7 (b), for the cases where states $|3\rangle$ and $|5\rangle$ are included as intermediates (dashed line), and when the first excited state $|1\rangle$ (solid line) is included as well. We note that the even parity states $|2\rangle$ and $|4\rangle$ do not contribute, as single photon transitions between these states and the (even parity) ground state are dipole forbidden, i.e., the dipole moments μ_{02} and μ_{04} are identically zero, and therefore are not considered as fitting parameters.

The two peaks which appear about the third and fifth excited state resonances can be well reproduced in the cases where these excited states are included, and further improvement (at low energies) is achieved when the first excited state is additionally included. From the previous section, the absorption delay $\Delta t_{abs}^{(res)}$, as a function of detuning and therefore central frequency, peaks with a roughly Gaussian shape about the resonant frequency for an isolated resonance (c.f., Fig. 5.1). Due to the model potential having well isolated resonances, the model should capture these features, which is indeed what we observe. However, the sharp peak at approximately 1.9 a.u. is not captured by the perturbation theory model, and therefore cannot be attributed to an overlapping of the third and fifth excited state resonances.

The effect of overlapping resonances is observed, however, in the frequency regime between the first and third excited state resonances. This can be seen in Fig. 5.7 (b) in the result of the model calculation when the first excited state is included. What we observe is that the decrease of the absorption delay at frequencies $\omega < \omega_{30}$ is captured only once the first excited state is included in the fit. This is interesting since for a frequency resonant with the first excited state, at $\omega = \omega_{10} = 0.976$ a.u., there is not sufficient energy to ionize the system from the ground state ($E_0 = -2.336$ a.u.) with two photons of the central frequency. Therefore, the influence of the first excited state is due to the broad bandwidth of the attosecond pulse and its strong coupling to the ground state.

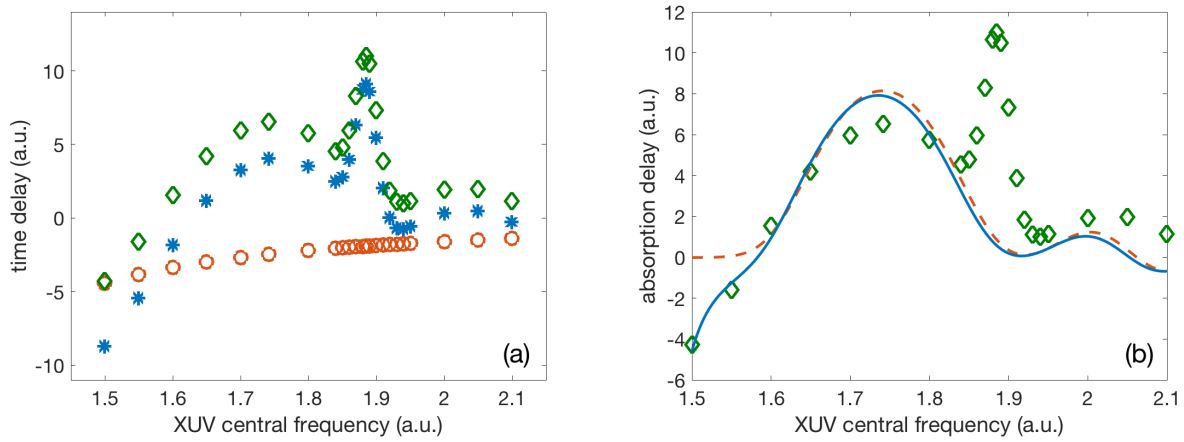

Figure 5.7: (a) TDSE calculations of the absorption delay Δt_{abs} (diamonds), the two-photon streaking delay Δt_{s} (stars), and the continuum delay Δt_{c} (circles) for the model system as a function of XUV central frequency. The pulse parameters used are $\lambda_{\mathrm{s}} = 2400$ nm, $N_{\mathrm{s}} = 3$ cycles, $I_{\mathrm{s}} = 1 \times 10^{11}\,\mathrm{W/cm^2}$, $\phi_s = \phi_{XUV} = -\pi/2$, $\tau_{\mathrm{XUV}}^{\mathrm{FWHM}} = 350$ as. For the simulation of the resonant two-photon ionization, an XUV intensity of $I_{\mathrm{XUV}} = 1 \times 10^{13}\,\mathrm{W/cm^2}$ is used, whereas for the continuum delay Δt_c, an intensity of $I_{\mathrm{XUV}} = 1 \times 10^{14}\,\mathrm{W/cm^2}$ is used to initiate the one-photon ionization. In (b), the absorption delay from TDSE calculations (diamonds) are compared with perturbation theory predictions, when including the third and fifth excited states as intermediates (dashed line) as well as when the first excited state is also included (solid line). The dipole moment products $\mu_{fj}\mu_{ji}$ for intermediate state $|j\rangle$ have been used as (constant) fitting parameters.

The feature which is not captured by the model is the sharpest and tallest peak in the absorption delay profile. This peak appears in the region around $\omega = 1.9$ a.u, which is very close to the fourth excited state resonance ($\omega_{40} = 1.9057$ a.u.), and it was mentioned above that this transition is dipole forbidden. Our model however, beyond the assumptions of second order perturbation theory, only considers interaction with the XUV pulse. Therefore, in order to understand the occurence of the sharp peak, we need to consider other effects beyond our model, e.g., the influence of the streaking field. In section 5.1, we showed that the streaking pulse has no effect on the absorption delay for the system and pulses considered in that study where the resonant state was strongly bound. In general, it has usually been assumed that the streaking pulse plays no role on the transition of the electron into the continuum itself. However, it was suggested in the previous section as well as in Ref. [20] that the discrepancies seen between our model calculations for He atom and TDSE simulations in Fig. 5.3 (b) may be due to the effect of the infrared pulse upon the intermediate states.

The influence of the IR field on electronic transitions is known from other methods involving the simultaneous application of XUV and IR pulses [14, 15]. For example, in attosecond transient absorption spectroscopy (ATAS) (c.f., section 1.3.2), sidebands are observed around energies corresponding to so-called "dark states" [15], as shown in Fig. 5.8. Dark states are states that cannot be populated via transition from the ground state due to dipole selection rules. These sidebands are referred to in the literature as light-induced states (LISs) [14] and occur in the region of an ATAS spectrum where the XUV and IR pulses overlap. In a simple picture of this effect, each LIS may be associated with a two-photon process that involves the absorption of an XUV photon and then either absorption or stimulated emission of an IR photon, such that the atom may end up with population in a state that cannot be populated by a single XUV photon, as illustrated in the schematic shown in Fig. 5.8. In the current context of attosecond streaking, such effects would be present in the absorption delay if an electron populating a dark state, having undergone the process shown in Fig. 5.8, transitions into the continuum via absorption of a second XUV photon.

In order to determine whether the same physics is responsible for the occurence of the sharp

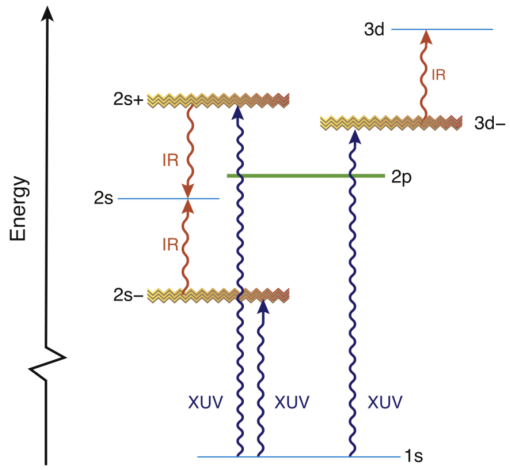

Figure 5.8: The "dark" 2s state in He may be populated via absorption or stimulated emission of an IR photon in addition to an XUV photon for a transition from the initial 1s state (Taken from Ref. [14]).

peak in Fig. 5.7, we performed a few test calculations. First, contrary to what we saw in the case of the isolated resonance (c.f., Table 5.1) the peak should depend on the intensity of the IR field, but not the XUV intensity. Second, the other peaks that we explained via our perturbative model should not depend on the IR intensity. Lastly, the position of the peak should not be at the forbidden transition frequency ω_{40}, but should be offset by an IR photon, i.e., $\omega = \omega_{40} - \omega_{IR} \simeq 1.886$ a.u.

The first and last expectations are satisfied, as demonstrated by the results in Fig. 5.9 (a), where the absorption delay for various frequencies in the region around the sharpest peak of Fig. 5.7 is plotted as a function of streaking pulse intensity. We see that there is a significant dependence upon the streaking field intensity when the XUV central frequency is tuned to $\omega_{40} - \omega_{IR}$, yet no such dependence is present at the other central frequencies considered. In addition, we see in Fig. 5.9 (b) that the absorption delay in the vicinity of the fourth excited state does not depend on the XUV intensity. The second condition is shown to be satisfied in Fig. 5.9 (c), where we see that the absorption delay about the dipole-allowed third excited state transition has minimal dependence on the streaking field intensity, which implies that the absorption delay at this frequency can be

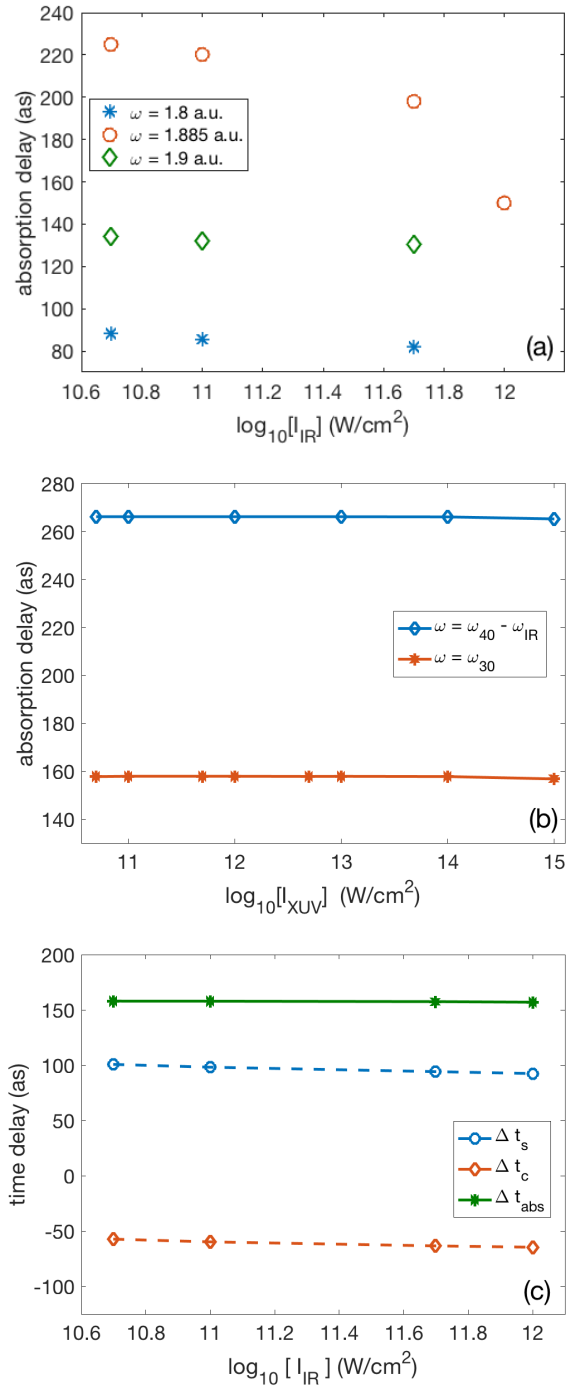

Figure 5.9: (a) Absorption delay as a function of streaking pulse intensity for three different XUV central frequencies. All other parameters remain fixed to the same values as in Fig. 5.7. (b) Absorption delay as a function of ionizing pulse intensity for the case of the dipole-forbidden fourth excited state minus a streaking photon (blue line plus diamonds), and the case where resonant with the dipole-allowed third excited state (red line plus asterisks). All other pulse parameters remain fixed. (c) The streaking (blue dashed with circles), continuum (red dashed with diamonds), and absorption (solid green line with asterisks) delay as a function of streaking pulse intensity when the ionizing pulse is tuned to resonance with the dipole-allowed third excited state.

well described by the method of section 5.1. Our results indicate that it is primarily the streaking pulse which enables the accumulation of an absorption delay in the vicinity of one-photon forbidden transitions.

We further note that the peak in the absorption delay only appears at $\omega = \omega_{40} - \omega_{IR} = 1.886$ a.u., and not at the frequency $\omega = \omega_{40} + \omega_{IR} = 1.9254$ a.u. Remembering that Fig. 5.7 is plotted as a function of XUV central frequency, this asymmetry implies that the dark state is populated via absorption of one XUV photon and then subsequent absorption of an IR photon, but is not populated via absorption of one XUV photon and the emission of an IR photon. This is contrary to what is observed in ATAS experiments and simulations (see Fig. 5.8), where peaks corresponding to both absorption and stimulated emission of an infrared photon are observed. Currently the reason for this is unknown, and further investigation is needed.

We have shown in this section that overlapping resonances can give rise to absorption delays of different behavior to that of the previous section. In addition, we have shown that in contrast to the strongly bound case studied in Chapter 4, the streaking pulse may play a role in the accumulation of an absorption delay, specifically it can contribute an infrared photon to populate an intermediate state which would otherwise be forbidden for a transition initiated by a single XUV photon.

5.3 Absorption delay in H_2^+

In the quest to control interactions of light and matter on the attosecond timescale, it is desirable that the methods used to obtain information for atoms may also be extended to learn about molecules. In particular, we wish to see whether the absorption delay is a useful observable for dynamics in molecules. As a first step, we will consider only electronic resonances in a model for a simple one-electron diatomic molecule, while neglecting rovibrational transitions. To this end, in this section we study the behavior of the absorption delay in resonant two-photon ionization of a 1D model of the simplest molecule H_2^+ under the Born-Oppenheimer (fixed-nuclei) approximation.

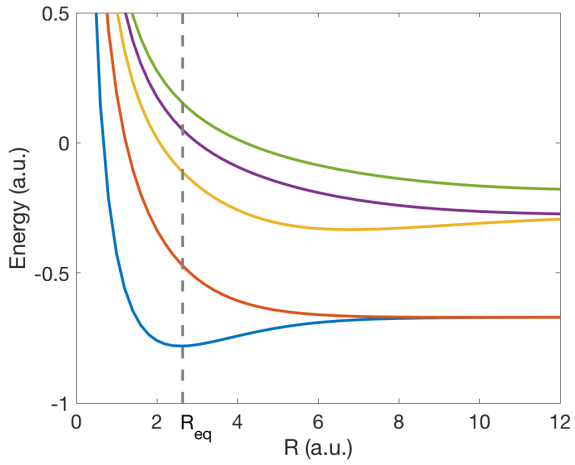

Figure 5.10: Potential energy surface for the 1D model of H_2^+. The ground state, and the first four excited states are shown as a function of internuclear distance. Also shown is the equilibrium internuclear distance of $R_{eq} = 2.64$ a.u. (dashed line).

5.3.1 Simulations of the absorption delay

For our TDSE simulations of the streaking of our model H_2^+ molecule, we take a one-dimensional Born-Oppenheimer potential of the form

$$V(r) = -\frac{1}{\sqrt{\left(r+\frac{R}{2}\right)^2+\alpha}} - \frac{1}{\sqrt{\left(r-\frac{R}{2}\right)^2+\alpha}} + \frac{1}{R}, \tag{5.18}$$

with the nuclei located at $\pm\frac{R}{2}$ where R is the internuclear distance. On the right hand side of Eq. (5.18), the first two terms represent the attractive potential felt by the electron due to each of the nuclei, and the last term represents the energy due to nuclear repulsion. We solved for the Born-Oppenheimer potential energy surfaces of the molecular model by solving the time-independent Schrödinger equation for varying internuclear distances R. We found the internuclear distance at equilibrium at $R_{eq} = 2.64$ a.u. by solving for the minimum of the ground state potential energy surface, as shown in Fig. 5.10 (dashed line). The lowest electronic energies at the equilibrium internuclear distance $E_n(R_{eq})$ are $E_0 = -1.1591$, $E_1 = -0.8502$, $E_2 = -0.4905$, $E_3 = -0.3278$, $E_4 = -0.2251$, and $E_5 = -0.1665$ a.u.

As mentioned, we wish to see if the concept of the absorption delay may be extended to a molecular system. Therefore, we calculated the absorption delay as a function of XUV central

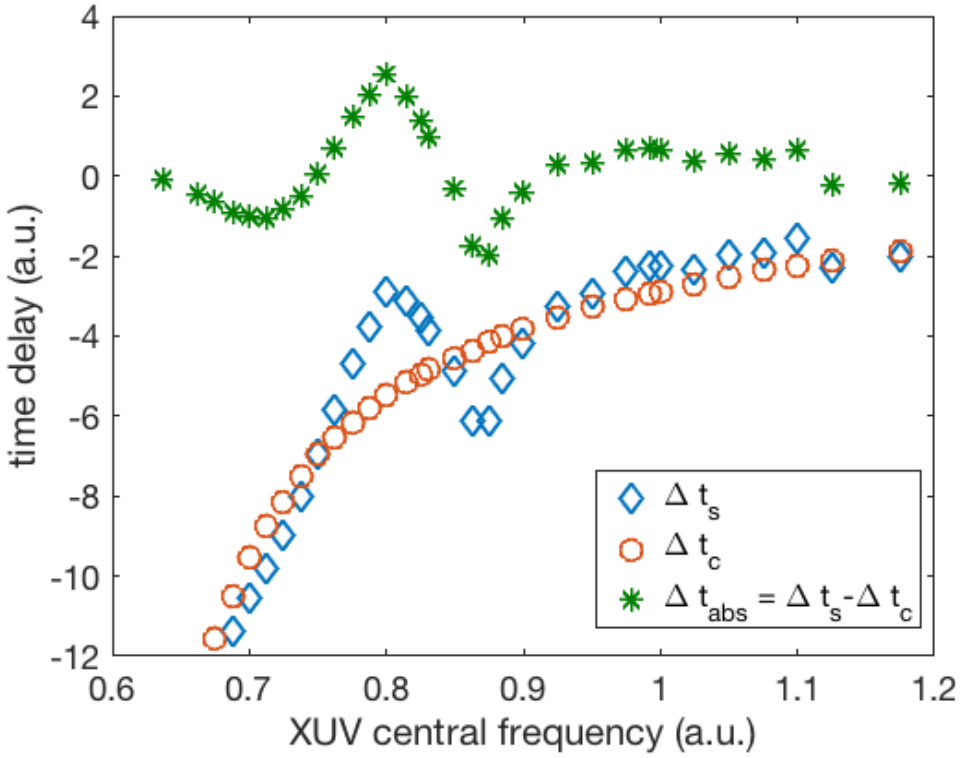

Figure 5.11: Absorption delay as a function of XUV central frequency for the resonant two-photon ionization of H_2^+. Field parameters for the streaking pulse used are the same as those in Fig. 5.7. For the XUV pulse, a sine squared envelope is used with a pulse duration of $T_{XUV} = 3$ fs, and the same intensity and CEP is used as in Fig. 5.7.

frequency in exactly the same manner as in the previous section. The range of XUV central frequencies considered for the two-photon process was from 0.65 a.u. to 1.1591 a.u., where the upper bound is simply the ionization potential. Within this range, the electron is most likely to transition into the continuum via the absorption of two XUV photons. The results for the absorption delay are shown in Fig. 5.11. We no longer see the pronounced features of individual resonances as in the previous two sections. Instead, the absorption delay appears to contain contributions from several resonances, which gives a less clear picture. In order to further analyze the result, we again turn to second order time dependent perturbation theory to help shine light on the physics. In particular, as in the previous section we wish to know which excited states play a role over the central frequency range considered.

5.3.2 Role of the excited states and interfering pathways

Our analysis is made in a similar manner as in the previous section. We use Eq. (5.3), and allow more excited states to participate in the sum over intermediate states. The most distinctive feature in Fig. 5.11 is the asymmetric, Fano-like lineshape centered around the $|0\rangle \rightarrow |3\rangle$ resonant transition at $\omega_{30} = 0.8313$ a.u. As seen in the previous examples of the current Chapter, the absorption delay for resonant two-photon transitions as a function of XUV central frequency is generally at a maximum when tuned exactly to resonance. This is in contrast to what is shown in Fig. 5.11, where at $\omega = \omega_{30}$, the absorption delay is close to zero, which is perhaps indicative of an interference effect. In order to reveal which states are responsible for this feature, we systematically allow for more intermediate states $|m\rangle$ to contribute to the sum in Eq. (5.3) and analyze the resulting absorption delay for each number of contributing intermediate states.

In order to accurately determine the dipole moment contributions in Eq. (5.3), we have numerically calculated the transition dipole moments, using the plane wave approximation for the bound-free transitions giving way to μ_{fm}. We then calculated c_{fi} and ϕ_f using Eqs. (5.3) and (5.5), and obtained $\Delta t_{abs} = \partial\phi_f/\partial E$ through the use of a numerical derivative. The absorption delay calculated in this manner, when considering only the 3rd excited state as an intermediate is

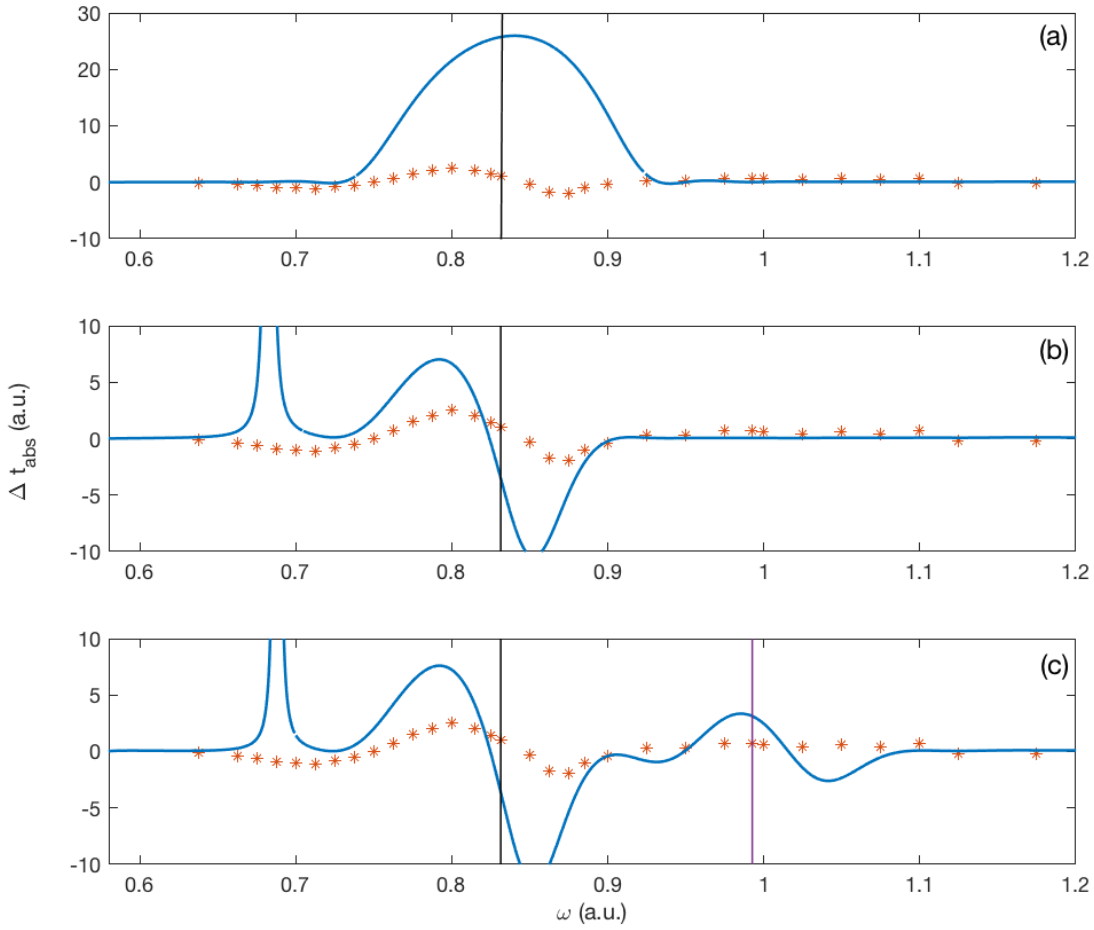

Figure 5.12: Resonant two-photon ionization of the 1D model of H_2^+ calculated via time-dependent perturbation theory (blue solid line) where (a) $m = 1$, (b) $m = 1$, 3, and (c) $m = 1$, 3, and 5 are considered in the sum in Eq. (5.3) as compared to TDSE simulations (red stars). The vertical lines mark the third (black) and fifth (purple) excited state resonances.

shown in Fig. 5.12 (a) (solid line) as compared to the TDSE simulations (stars). We clearly see that a single intermediate state cannot explain the feature seen around $\omega = \omega_{30}$. The absorption delay, when including both the first and third excited states as intermediates, is presented in Fig. 5.12 (b). We now see the appearance of an asymmetric feature in the model calculation of the absorption delay centered around the third excited state resonance, however it is of a significantly larger magnitude than that found in the TDSE simulations. Finally, we consider including the fifth excited state as a possible intermediate in Fig. 5.12 (c), and we see that a similar feature appears about the fifth excited state resonance ω_{50}. However, due to a high density of states in this region and the large bandwidth of the attosecond pulse, a larger number of intermediates are likely to be contributing, causing a different lineshape than is seen in the TDSE result. Therefore, in order to obtain better quantitative agreement in future work, more intermediate states need to be included to predict this lineshape.

We note that in panels (b) and (c) of Fig. 5.12, we see a large, divergent peak around the central frequency corresponding to $\omega_{20} = 0.6686$ a.u., in contrast to the TDSE result (stars), which shows a smooth minimum in the absorption delay around this region. It is therefore another indication that our model calculation, when considering the 1st, 3rd, and 5th excited states as intermediates, is not sufficient in describing the dynamics in this region. It is unlikely that continuing to add dipole-allowed intermediate states in our second-order model will account for this particular feature, and therefore future work will need to go beyond the additional approximations made in our model. For example, going beyond second order perturbation theory, which was discussed in the previous section, is such a consideration. We saw that a third order process in the form of the IR pulse contributing a photon during transition into the continuum could lead to the occupation of an otherwise forbidden intermediate state. The same could be true in the current case for the second excited state of the model, but further investigation is needed.

Chapter 6

Single photon ionization with isolated elliptically polarized attosecond pulses

As discussed in Chapter 1, isolated circularly and elliptically polarized attosecond pulses have recently been demonstrated experimentally [9]. Since this is a new development, the use of these pulses for applications in attosecond spectroscopy has not been thoroughly explored. In this Chapter we study photoionization of atoms with isolated elliptically polarized attosecond pulses, and take a few first steps towards exploring the possibility of gaining information about both the pulse and the system being probed with the use of an isolated attosecond pulse only, i.e., without a femtosecond pulse. In section 6.1, we motivate the method and describe our numerical simulations. Then, in section 6.2, we demonstrate the ability to control the resulting photoelectron angular distribution through changing the ellipticity of the applied pulse, and postulate the possible connection of the rotation of the distribution to a time. Finally, in section 6.3, we discuss opportunities for future study regarding so-called "ring current" states.

6.1 Unassisted XUV ionization

Up until now in this thesis, we have only considered methods in which an atom or molecule is exposed to both an XUV attosecond pulse and a femtosecond NIR pulse. The goal of this section is to analyze the photoelectron angular distribution (PAD) resulting from the application of an isolated elliptically polarized attosecond pulse to an atom or molecule, and to explore if dynamical information can be obtained. To this end, we show that the PAD depends upon the ellipticity of the applied attosecond pulse, and postulate the use of such a dependency to study dynamics on a

finer temporal resolution scale than the attoclock, which is a similar method.

The attoclock technique (see Refs. [13, 66], section 1.3.1.3) exposes an atom or molecule to a femtosecond circularly polarized laser pulse with a duration of two (or less) cycles. Normally, a circularly polarized pulse of many cycles will result in an isotropic PAD with respect to emission angle. In the attoclock technique however, the femtosecond pulse has few enough cycles such that the emission of an electron is predicted to be most probable in the positive and negative directions along the axis where the field vector points at its maximum intensity. This axis is typically chosen in numerical attoclock simulations as the $y-$axis in the plane of polarization. In such a case, the positive $\hat{y}-$direction is defined as the "time zero" of the clock. The obtained photoelectron spectrum in the attoclock setup is then measured in the plane of polarization. The attoclock time delays are determined by the angular offset of the maximum of the PAD from the direction of time zero (90° for the positive $\hat{y}-$direction). This angular offset is then converted into a time by considering that a full rotation of 360° corresponds to one period of the field (2.67 fs for an 800 nm pulse).

It is desirable to see if we can extend the concept of the attoclock to the case of an isolated XUV pulse which has a period on the scale of attoseconds. In order to achieve a similar symmetry of the PAD to the attoclock with an attosecond pulse of several cycle duration, we use an elliptically polarized pulse, constructed such that the field reaches its maximum when its polarization vector lies along the positive $\hat{y}-$direction, i.e., the major axis of the polarization ellipse. Thus in the following, we simulate the interaction of an atom with such a pulse, and determine the offset angle between the maximum of the calculated PAD and the positive $y-$axis. We will then briefly consider the consequences of converting this angle to a time, as is done for the attoclock.

6.1.1 TDSE simulations

We simulate the photoemission on a Cartesian 2D grid, corresponding to the polarization plane of the pulse, and use the SLEPc method described in Chapter 3 to solve the TDSE. Although we use length gauge for the interaction Hamiltonian, we set the vector potential as opposed to the

electric field, primarily due to how the code implementing the SLEPc method is set up. To this end, we use

$$\mathbf{A}(t) = \frac{\mathcal{A}_0(t)}{\sqrt{1+\xi^2}}\left[\cos(\omega t + \phi_{\text{CEP}})\,\hat{\mathbf{y}} - \xi\sin(\omega t + \phi_{\text{CEP}})\,\hat{\mathbf{x}}\right], \tag{6.1}$$

where $-1 \leq \xi \leq 1$ is the ellipticity of the pulse, ω describes the central frequency, ϕ_{CEP} is the carrier envelope phase, and $\mathcal{A}_0(t)$ is the envelope of the pulse, for which we use a Gaussian function:

$$\mathcal{A}_0(t) = A_0 \text{exp}\left[-\frac{(t - T_{\text{FWHM}}/2)^2}{(2\ln 2)\,T_{\text{FWHM}}^2}\right] \tag{6.2}$$

where T_{FWHM} is the full-width-half-maximum (FWHM) duration of the pulse envelope, and A_0 is the strength of the vector potential, which is related to the strength of the electric field as $A_0 = \frac{c}{\omega}E_0$. Note that we have chosen the $x-y$ plane as the plane of polarization with the y-axis defining the major axis of the ellipse. Furthermore, $\xi = \pm 1$ corresponds to left (right) circularly polarized light, and $\xi = 0$ corresponds to linearly polarized light along the y-axis. Throughout this section we use an attosecond pulse with intensity $I_{XUV} = |E_0|^2 = 10^{13}$ W/cm^2, central frequency $\omega = 1.0$ a.u., $\phi_{\text{CEP}} = 0$, and a pulse duration of 5 cycles FWHM. The ellipticity of the pulse will be varied in the calculations. In our simulations, we make use of a model hydrogen atom in 2D Cartesian space (x, y). The potential is chosen as

$$V(x,y) = -\frac{1}{\sqrt{x^2+y^2+\alpha^2}} \tag{6.3}$$

with $\alpha = 0.8$. Using a grid spacing of $\Delta x = \Delta y = 0.2$ and a grid size of [-750, 750] a.u. for both $x-$ and $y-$axes, the use of the Krylov-Schur method gives a ground state energy of $E_g = -0.4996$ a.u., and the first and second excited states are degenerate with an energy of $E_{1,2} = -0.1842$ a.u., which are reasonably close to the $n = 1$ and $n = 2$ energy levels of the 3D hydrogen atom.

We obtain the photoelectron momentum distributions in a similar way as outlined in the case of linear streaking (see section 3.3). That is, we propagate the ionized wavepacket sufficiently far on the grid such that it is well separated from the remaining ion core, while confirming that it does not reach the boundaries. Assuming that we have propagated sufficiently far such that the error from projecting onto a plane wave is negligible, we cut out the remaining core, and perform a Fourier transform to obtain the photoemission spectrum.

6.2 Dependence of angular distributions on ellipticity

Using the method described above, we obtain the PAD for the ionization of our model system initially in the ground state $|g\rangle$ with isolated elliptically polarized attosecond pulses of various ellipticities. The results are shown in Fig. 6.1, where we show the PAD in momentum space for a few selected ellipticities. In the case of $\xi = 0.0$ (a), we see the typical p-wave behavior of photoemission pumped by a linearly polarized pulse from an $s-$like ground state. As the ellipticity is increased, the PAD extends over a broader angular range until for $\xi = 1.0$ ((e), right handed circular polarization) we observe the expected isotropic emission pattern. Besides covering a broader range in angular emission, the angle of maximum emission does not remain at 90° as the ellipticity is increased from 0 to 1.0. This variation is not resolved in the presentation of the PADs in Fig. 6.1, but it becomes obvious in Fig. 6.2, where we have replotted the angular distributions (for fixed $k = 1.0$ a.u.) for the same value of ellipticity as in Fig. 6.1. We can now clearly see that as the ellipticity is increased, the angle for maximum emission is offset further from the $y-$axis (denoted as 0° in the Figure). In Fig. 6.3, we summarize these results by showing this offset angle as a function of ellipticity, spanning across the entire range of ellipticity from left circularly polarized to right circularly polarized. We see that the maximum of the PAD rotates in the direction of the polarization of the field such that the angular offset is an odd function with respect to ellipticity, i.e. representing the offset as $\theta_{\max}(\xi)$, we have $\theta_{\max}(\xi) = -\theta_{\max}(-\xi)$. As the limit of circularly polarized light is approached, the offset angle diverges since we reach an isotropic angular emission pattern in this case. Therefore, we can conclude that the ellipticity and helicity (left vs. right) of the ionizing attosecond elliptical pulse can be determined from the PAD. Furthermore, such a dependence of the preferred emission direction on the ellipticity may prove to be useful in potential control applications.

Having in mind that PADs generated by the interaction of atoms with circularly polarized femtosecond pulses were used to obtain information into temporal dynamics, it now becomes tempting to associate the observed rotation of the PAD with a time. The elliptically polarized pulses used

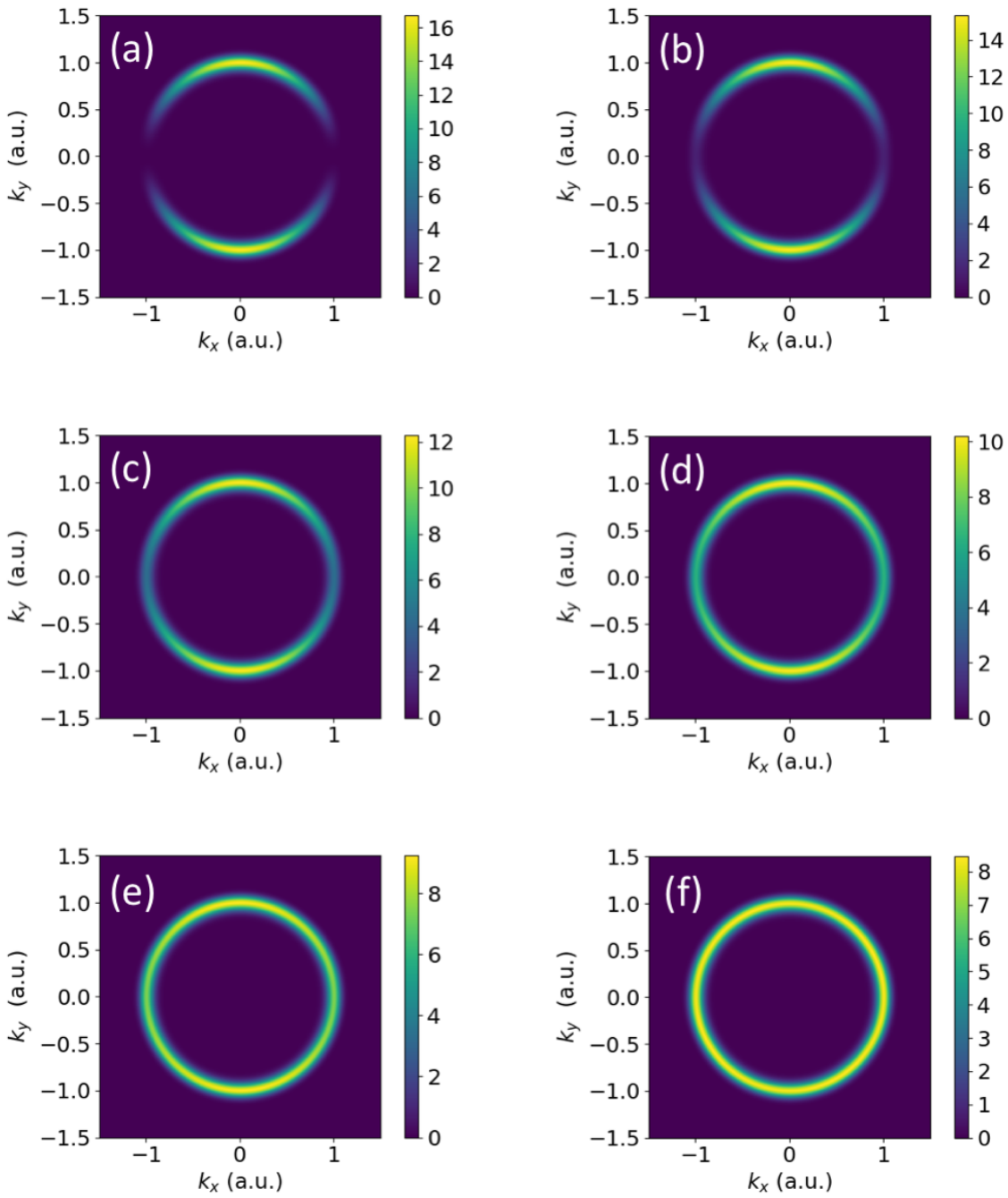

Figure 6.1: PADs for ionization from the ground state of the 2D hydrogen model for ellipticities of ξ = (a) 0.0 (linearly polarized), (b) 0.3, (c) 0.6, (d) 0.8, (e) 0.9, and (f) 1.0 (right circularly polarized). Other laser parameters are given in the text.

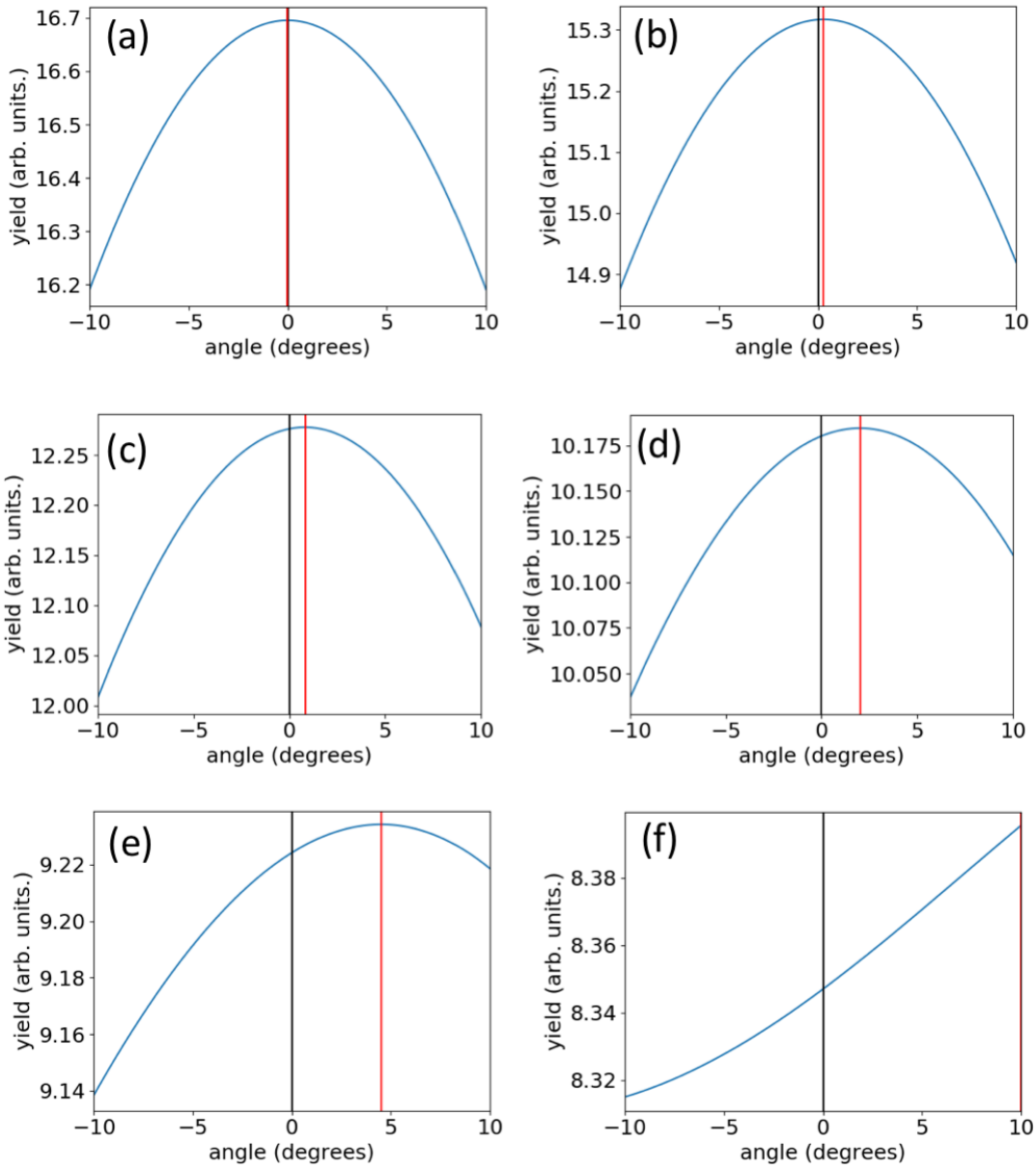

Figure 6.2: PADs along k_{max} as a function of angle. Ellipticities are the same as in Fig. 6.1. The peak of the distribution (red vertical line) and the location corresponding to zero degrees rotation from the major axis (black vertical line) are shown.

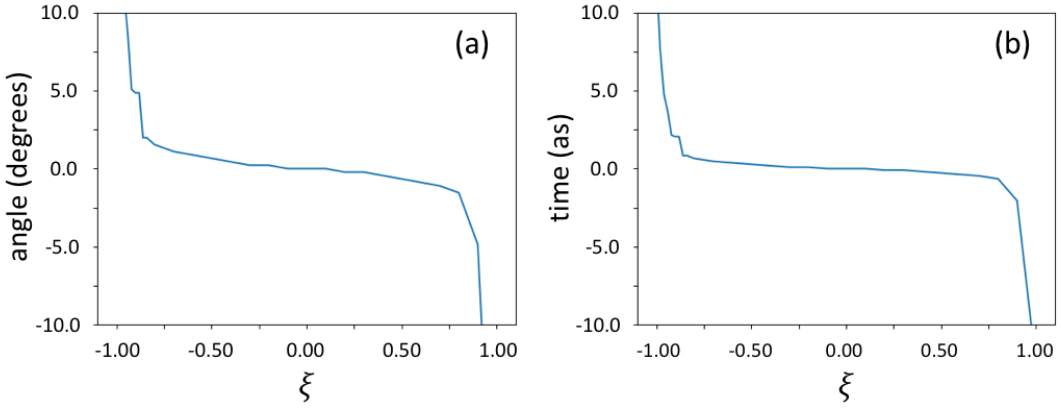

Figure 6.3: Angle of maximum emission in the PADs from ionization of the 1s state of the 2D hydrogen model, plotted as (a) an angle and (b) a time (see text for relation), as a function of ellipticity ξ.

in the calculations have a period of 152 as, and therefore we can associate a time with the observed angle by using the conversion $360^\circ = 152$ as. Accordingly, the obtained angle of maximum emission is replotted as time vs. ellipticity in Fig. 6.3 (b). Assuming that this conversion is meaningful, we see that the times measured using this technique are below one attosecond.

6.3 Future work

In considering potential applications of the method described in this Chapter, we pose the question of whether the technique can be used to temporally resolve the rotation of the electron probability distribution in a so-called "ring current state", which has been observed in both atoms and conjugated ring molecules [127, 128]. Furthermore, it has been recently proposed that the attoclock could be used to time resolve the rotation of such a state [129]. Ring current states are superposition states which are characterized by an electron distribution which rotates in time, subsequently creating a magnetic field. These states have a well-defined angular momentum projection quantum number $\pm m$, where +(-) corresponds to counterclockwise (clockwise) rotation, if viewing from above the polarization plane. In this section, we demonstrate the preparation of a ring current state, using our 2D hydrogen model potential, to visualize the temporal- and angular-distribution

of the state as a function of time. The demonstration is provided in order to motivate future proof of principle studies with respect to using isolated elliptically polarized attosecond pulses to image the oscillation of the ring current state in time.

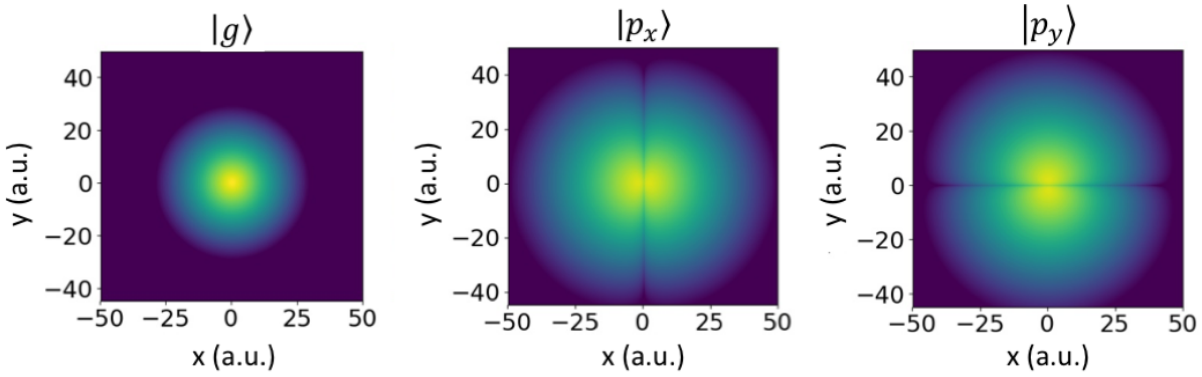

Figure 6.4: The first three eigenstates of the 2D model hydrogen atom are shown, where $|g\rangle$ denotes the ground state, and since we only consider three eigenstates in this section, we label the first two excited states as $|p_x\rangle$ and $|p_y\rangle$ without a principal quantum number.

The first three eigenstates for the 2D hydrogen model defined by the potential in Eq. (6.3) are shown in Fig. 6.4, where we label the states as $|g\rangle$ for the ground state, and since the first two excited states have angular nodes aligned with the $x-$ or $y-$ axis, we denote them as $|p_x\rangle$ and $|p_y\rangle$ according to the direction along which the maximum of the electron probability distribution lies. It is important to note that because we are in 2D Cartesian coordinates, one cannot label the eigenstates of the 2D model Hamiltonian with the common quantum numbers of 3D atoms, and the use of the labels p_x and p_y is a choice made for convenience, as these orbitals are similar to the $|2p_x\rangle$ and $|2p_y\rangle$ states of hydrogen. Since we limit ourselves to these three eigenstates, no principal quantum number n is needed in the current discussion to distinguish between the different states. In our model potential, a ring current state can be prepared by superposing the ground state with the states $|p_\pm\rangle$ defined as

$$|p_\pm\rangle = |p_x\rangle \pm i\,|p_y\rangle \tag{6.4}$$

such that the ring current states are

$$|\Psi_\pm\rangle = c_g\,|g\rangle + c_p\,|p_\pm\rangle\,, \tag{6.5}$$

where $|g\rangle$ denotes the ground state, and $|p_x\rangle$ and $|p_y\rangle$ refer to the states labeled as such in Fig. 6.4. For the current demonstration, let $c_g = \frac{1}{\sqrt{3}}$ and $c_p = \sqrt{\frac{2}{3}}$, and without loss of generality, assume we wish to prepare the state $|p_+\rangle$. The probability distribution $|\Psi_+(t)|^2$ rotates in the counterclockwise direction with a period of rotation of $\tau = 2\pi/|E_p - E_s| \simeq 20$ a.u., or 483.8 as. Since this rotation occurs on the attosecond time scale, it provides a test case to see if the rotation can be temporally resolved to a high degree by ionizing the state with an isolated elliptically polarized attosecond pulse. We demonstrate the rotation of the ring current state by allowing the superposition state to oscillate freely in time, and calculate the $\hat{x}$ and $\hat{y}$ components of the time-dependent dipole moment, which is defined as the negative expectation value of position as a function of time:

$$\mathbf{d}(t) = -\langle \Psi_+(t) | \mathbf{r} | \Psi_+(t) \rangle . \tag{6.6}$$

The results are shown in Fig. 6.5, where the $x-$ (blue) and $y-$ (orange) components of $\mathbf{d}(t)$ demonstrate that the oscillation period is 20 a.u. as expected.

The goal for a possible next step will be to resolve the oscillating phase of the ring current as a function of time, such that imaging of the superposition state becomes possible. Furthermore, future work could also focus on the resonant two-photon ionization using the ring current state as an intermediate, and whether or not the concept of the absorption delay for resonant two-photon ionization with an isolated linearly polarized attosecond pulses, as discussed in detail in Chapter 5, can be extended to the proposed study.

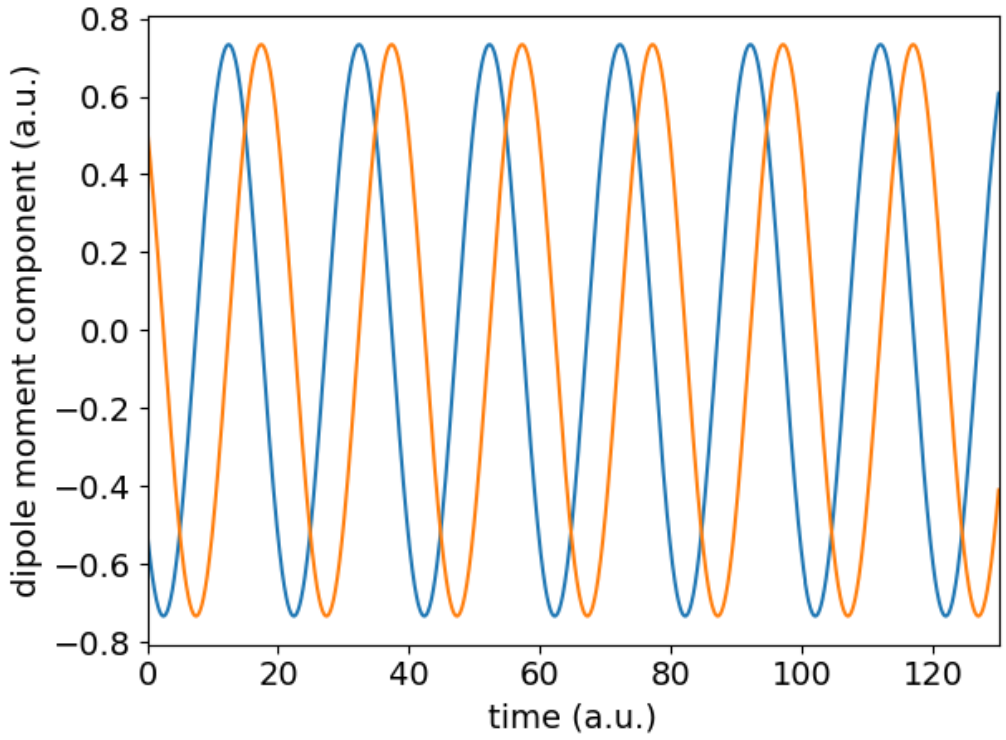

Figure 6.5: Vector components of the time-dependent dipole moment, Eq. (6.6), of the ring current state, when allowed to freely evolve in time. We see that both d_x (blue) and d_y (orange) oscillate with a period of about 20 a.u.

Chapter 7

Summary and perspective

This thesis involved theoretical efforts to resolve electron dynamics on attosecond timescales through the study of photoemission time delays in one- and two-photon ionization, particularly through the use of the attosecond streaking technique. We have developed analytical models for the two contributions to the photoemission delay: the so-called continuum and absorption time delays, which agree well with numerical simulations. We have further shown that these analytical formulae can be used to provide a deeper understanding of the origin of the time delays themselves, and also to analyze effects in attosecond streaking not considered up to this point.

To this end, we covered in the first three Chapters a description of fundamental concepts regarding attosecond laser physics and the basic techniques of the field, previous studies regarding the subject of photoemission time delays, as well as an overview of the analytical and numerical methods used in this thesis to analyze laser-matter interactions.

We then continued in Chapter 4 by analyzing the continuum delay in one-photon ionization. We were able to derive an analytical formula for the contribution, and showed that it can be used to efficiently obtain accurate estimates of the streaking time delay. Furthermore, we provided new insights in the separation of the time delay into the WS time delay and a Coulomb-laser coupling term. We then showed how the analytical formula could also be easily applied to other scenarios, and hence to analyze a recent theoretical proposal as well as the potential effects of the attochirp on the continuum delay.

In Chapter 5, we used time-dependent perturbation theory to derive an analytical expression

of the absorption delay, and obtained good agreement with numerical simulations in the case of an isolated resonance. We then extended our studies to gain insight into cases where multiple resonances contribute to the absorption delay. Furthermore, by comparing our analytical results to numerical simulations for a model system, we were able to determine that the streaking pulse can play a role in populating so-called dark states, similar to that of the near-infrared field in attosecond transient absorption spectroscopy. In the final section, we showed an application of our analytical formula to the study of the absorption delay in a model H_2^+ molecule, and showed that novel features in the absorption delay are obtained. We ended the Chapter by suggesting that future studies should be made to gain further insights into these features in order to study electron dynamics in molecules.

Lastly, in Chapter 6 we began to study the ionization of an atom interacting with an isolated elliptically polarized attosecond pulse, since these pulses have now become available in experiment. We studied the photoelectron angular distribution resulting from the application of pulses with varying ellipticity. We were able to determine that there is an offset of the angular distribution with respect to the major polarization axis of the elliptical pulse, and that the offset depends on ellipticity, and is asymmetric with respect to helicity. Finally, we considered the attoclock concept to demonstrate that the rotations correspond to a resolution on a sub-attosecond time scale, assuming that such a conversion is applicable. We concluded by suggesting that this technique could potentially be used in future studies to image dynamics involving ring current states in atoms.

Bibliography

[1] C. Goldsmith, J. Su, A. Jaroń-Becker, and A. Becker. Journal of Physics B: Atomic and Molecular and Optical Physics, 51:155602, 2018.

[2] P. B. Corkum and F. Krausz. Nature Physics, 3:381–387, 2007.

[3] M. F. Kling and M. J. Vrakking. Annual Review of Physical Chemistry, 59:463–492, 2008.

[4] Michelle Miller. Time Resolving Electron Dynamics in Atomic and Molecular Systems Using High-Harmonic Spectroscopy. PhD thesis, University of Colorado at Boulder, 2016.

[5] H. C. Kapteyn, M. M. Murnane, and I. P. Christov. Physics Today, 58:39, 2005.

[6] M. Chini, K. Zhao, and Z. Chang. Nature Photonics, 8:178, 2014.

[7] J. A. Wheeler, A. Borot, S. Monchocè, H. Vincenti, A. Ricci, A. Malvache, R. Lopez-Martens, and F. Quèrè. Journal of Physics B: Atomic and Molecular and Optical Physics, 6:829–833, 2012.

[8] M. C. Chen, C. Mancuso, C. Hernández-Garcia, F. Dollar, B. Galloway, D. Popmintchev, P.-C. Huang, B. Walker, L. Plaja, A. Jaroń-Becker, A. Becker, M. M. Murnane, H. C. Kapteyn, and T. Popmintchev. Nature Photonics, 111:E2361, 2014.

[9] P.-C. Huang, J.-T. Huang, P.-Y. Huang, C.-H. Lu, C. Hernández-Garcia, A. H. Kung, S.-D. Yang, and M.-C. Chen. Polarization control of isolated attosecond pulses. In Conference on Lasers and Electro-Optics, page JTh5B.9. Optical Society of America, 2017.

[10] F. Krausz and M. Ivanov. Review of Modern Physics, 81:163–234, 2009.

[11] M. Uiberacker and F. Krausz. SPIE's oemagazine, May:18–22, 2004.

[12] K. Klünder, J. M. Dahlström, M. Gisselbrecht, T. Fordell, M. Swoboda, D. Guenot, P. Johnson, J. Caillat, J. Mauritsson, A. Maquet, R. Taïeb, and A. L'Huillier. Physical Review Letters, 106:143002, 2011.

[13] L. Gallmann, C. Cirelli, and U. Keller. Annual Review of Physical Chemistry, 63:447–469, 2007.

[14] M. Wu, S. Chen, S. Camp, K. J. Schafer, and M. B. Gaarde. Journal of Physics B: Atomic and Molecular and Optical Physics, 49:062003, 2016.

[15] A. N. Pfeiffer, M. J. Bell, A. R. Beck, H. Mashiko, D. M. Neumark, and S. R. Leone. Physical Review A, 88:051402(R), 2013.

[16] Jing Su. Theoretical Analysis and Numerical Simulation of Attosecond Time Delays in Photoionization. PhD thesis, University of Colorado at Boulder, 2014.

[17] M. Schultze, M. Fieß, N. Karpowicz, J. Gagnon, M. Korbman, M. Hofstetter, S. Neppl, A. L. Cavalieri, Y. Komninos, T. Mercouris, C. A. Nicolaides, R. Pazourek, S. Nagele, J. Feist, J. Burgdörfer, A. M. Azzeer, R. Ernstorfer, R. Kienberger, U. Kleineberg, E. Goulielmakis, F. Krausz, and V. S. Yakovlev. Science, 328:1658–1662, 2010.

[18] M. Isinger, R. J. Squibb, D. Busto, S. Zhong, A. Harth, D. Kroon, S. Nandi, C.L. Arnold, M. Miranda, J.M. Dahlström, E. Lindroth, R. Feifel, M. Gisselbrecht, and A. L'Hullier. Science, 358:6365, 2017.

[19] J. M. Dahlström, T. Carette, and E. Lindroth. Physical Review A, 86:061402, 2012.

[20] J. Su, H. Ni, A. Jaroń-Becker, and A. Becker. Physical Review Letters, 113:263002, 2014.

[21] C. Cirelli, C. Marange, S. Heuser, C. L. M. Petersson, Á. Jiménez-Galán, L. Argenti, S. Zhong, D. Busto, M. Isinger, S. Nandi, S. Maclot, L. Rading, P. Johnsson, M. Gisselbrecht, M. Lucchini, L. Gallmann, J. M. Dahlström, E. Lindroth, A. L'Hullier, F. Martín, and U. Keller. Nature Communications, 9:955:1–9, 2018.

[22] R. Pazourek, S. Nagele, and J. Burgdörfer. Faraday Discussions, 163:353–376, 2013.

[23] C. Goldsmith, J. Su, A. Becker, and A. Jaroń-Becker. Physical Review A, 96:053410, 2017.

[24] S. Nagele, R. Pazourek, J. Feist, and J. Burgdörfer. Physical Review A, 85:033401, 2012.

[25] J. Feist, O. Zatsarinny, S. Nagele, R. Pazourek, J. Burgdörfer, X. Guan, K. Bartschat, and B.I. Schneider. Physical Review A, 89:033417, 2014.

[26] R. Pazourek, S. Nagele, and J. Burgdörfer. Review of Modern Physics, 87:765–802, 2015.

[27] D. Kiesewetter, R. R. Jones, A. Camper, S. B. Schoun, P. Agostini, and L. F. DiMauro. Nature Physics, 14:68–73, 2018.

[28] C. Goldsmith, A. Jaroń-Becker, and A. Becker. Journal of Physics B: Atomic and Molecular and Optical Physics, 51:025601, 2017.

[29] A. S. Kheifets. Physical Review A, 87:063404, 2013.

[30] M. Ferray, A. L' Huillier, X. F. Li, L. A. Lompre, G. Mainfray, and C. Manus. Journal of Physics B, 21:L31–L35, 1988.

[31] A. McPherson, G. Gibson, H. Jara, U. Johann, T. S. Luk, I. A. McIntyre, K. Boyer, and C. K. Rhodes. Journal of the Optical Society of America B, 4:595–601, 1987.

[32] J. L. Krause, K. J. Schafer, and K. C. Kulander. Physical Review A, 45:4998–5010, 1992.

[33] J. L. Krause, K. J. Schafer, and K. C. Kulander. Physical Review Letters, 68:3535–3538, 1992.

[34] P. B. Corkum. Physical Review Letters, 71:1994–1997, 1993.

[35] M. Lewenstein, Ph. Balcou, M. Y. Ivanov, A. L'Huillier, and P. B. Corkum. Physical Review A, 49:2117–2132, 1994.

[36] I. P. Christov, J. Zhou, J. Peatross, A. Rundquist, M. M. Murnane, and H. C. Kapteyn. Physical Review Letters, 77:1743–1746, 1996.

[37] J. Zhou, J. Peatross, M. M. Murnane, H. C. Kapteyn, and I. P. Christov. Physical Review Letters, 76:752–755, 1996.

[38] I. P. Christov, J. Zhou, J. Peatross, A. Rundquist, M. M. Murnane, and H. C. Kapteyn. Physical Review Letters, 78:1251–1254, 1997.

[39] T. Popmintchev, M.-C. Chen, P. Arpin, M. M. Murnane, and H. C. Kapteyn. Nature Photonics, 4:822–832, 2010.

[40] T. Popmintchev, M.-C. Chen, D. Popmitchev, P. Arpin, S. Brown, S. Ališauskas, G. Andriukaitis, T. Balčiunas, O. D. Mucke, A. Pugzlys, A. Baltuška, B. Shim, S. E. Schrauth, A. Gaeta, C. Hernández-García, L. Plaja, A. Becker, A. Jaroń-Becker, M. M. Murnane, and H. C. Kapteyn. Science, 336:1287–1291, 2012.

[41] A. Einstein. Annalen der Physik, 17:132, 1905.

[42] A. B. Arons and M. B. Peppard. American Journal of Physics, 33:367–374, 1965.

[43] M. Göppert-Mayer. Annalen der Physik, 9:273–295, 1931.

[44] R. L. Fork, C. H. Brito-Curz, P. C. Becker, and C. V. Shank. Optics Letters, 12:483, 1987.

[45] M. M. Murnane, H. C. Kapteyn, M. D. Rosen, and R. W. Falcone. Science, 251:531–536, 1991.

[46] M. T. Asaki, C.-P. Huang, D. Garvey, J. Zhou, H. C. Kapteyn, and M. M. Murnane. Optics Letters, 18:977–979, 1993.

[47] P. Antoine, A. L'Hullier, and M. Lewenstein. Physical Review Letters, 77:1234, 1996.

[48] Z. Chang, A. Rundquist, H. Wang, M. M. Murnane, and H. C. Kapteyn. Physical Review Letters, 79:2967, 1997.

[49] O. E. ALong, V. Averbukh, and N. Moiseyev. Physical Review Letters, 80:3743, 1998.

[50] A. Rundquist, C. G. Durfee III, Z. Chang, C. Herne, S. Backus, M. M. Murnane, and H. C. Kapteyn. Science, 280:1412–1415, 1998.

[51] P. M. Paul, E. S. Toma, P. Breger, G. Mullot, F. Augé, Ph. Balcou, H. G. Muller, and P. Agnostini. Science, 292:1689–1692, 2001.

[52] R. Bartels, S. Backus, E. Zeek, L. Misoguti, G. Vdovin, I. P. Christov, M. M. Murnane, and H. C. Kapteyn. Nature, 406:164–166, 2000.

[53] M. Hentschel, R. Kienberger, Ch. Spielmann, G. A. Reider, N. Milosevic, T. Brabec, P. Corkum, U. Heinzmann, M. Drescher, and F. Krausz. Nature, 414:509–513, 2001.

[54] D. Umstadter, J. K. Kim, and E. Dodd. Physical Review Letters, 76:2073, 1996.

[55] T. Kwan, J. M. Dawson, and A. T. Lin. The Physics of Fluids, 20:581, 1977.

[56] P. B. Corkum, N. H. Burnett, and M. Y. Ivanov. Optics Letters, 19:1870, 1994.

[57] I. J. Sola, E. Mevel, L. Elouga, E. Constant, V. Strelkov, L. Poletto, P. Villoresi, E. Benedetti, J.-P. Caumes, S. Stagira, C. Vozzi, G. Sansone, and M. Nisoli. Nature Physics, 2:319, 2006.

[58] H. Vincenti and F. Quéré. Physical Review Letters, 108:113904, 2012.

[59] M. Ya. Schelev, M. C. Richardson, and A. J. Alcock. Applied Physics Letters, 18:354–357, 1971.

[60] D. J. Bradley, B. Liddy, and W. E. Sleat. Optics Communications, 2:391–395, 1971.

[61] J. Itatani, F. Quéré, G. L. Yudin, M. Y. Ivanov, F. Krausz, and P. B. Corkum. Physical Review Letters, 88:173903, 2002.

[62] M. Kitzler, N. Milosevic, A. Scrinzi, F. Krausz, and T. Brabec. Physical Review Letters, 88:173904, 2002.

[63] M. Drescher, M. Hentschel, R. Kienberger, G. Tempea, Ch. Spielmann, G. A. Reider, P. B. Corkum, and F. Krausz. Science, 291:1923–1927, 2001.

[64] J. M. Dahlström, D. Guénot, K. Klünder, M. Gisselbrecht, J. Mauritsson, A. L'Huillier, A. Maquet, and R. Taïeb. Chemical Physics, 414:53–64, 2013.

[65] A. Jaroń-Becker and A. Becker. Attosecond spectroscopy (invited review). In R. Guenther and D. Steel, editors, Encyclopedia of Modern Optics (2nd Edition), pages 233–243. Oxford: Elsevier, 2018.

[66] P. Eckle, M. Smolarski, P. Schlup, J. Biegert, A. Staudte, M. Schöffler, H. G. Muller, R. Dörner, and U. Keller. Nature Physics, 4:565–570, 2008.

[67] L. Argenti, Á. Jiménez-Galán, J. Caillat, R. Taïeb, and F. Martín. Physical Review A, 95:043426, 2017.

[68] L. Eisenbud. Dissertation. PhD thesis, Princeton University, 1948.

[69] E.P. Wigner. Physical Review, 98:145–147, 1955.

[70] F.T. Smith. Physical Review, 118:349–356, 1960.

[71] J.R. Taylor. Scattering Theory. Dover and New York, 2006.

[72] A. Messiah. Quantum Mechanics. Wiley and New York, 1966.

[73] S. Nagele, R. Pazourek, J. Feist, K. Doblhoff-Dier, C. Lemell, K. Tökéski, and J. Burgdörfer. Journal of Physics B: Atomic and Molecular and Optical Physics, 44:081001, 2011.

[74] A. S. Kheifets, I. A. Ivanov, and I. Bray. Journal of Physics B, 44:101003, 2011.

[75] I. A. Ivanov. Physical Review A, 83:023421, 2011.

[76] I. A. Ivanov. Physical Review A, 86:023419, 2012.

[77] I. A. Ivanov, A. S. Kheifets, and V. V. Serove. Physical Review A, 86:063422, 2012.

[78] V. V. Serov, V. L. Derbov, and T. A. Sergeeva. Physical Review A, 87:063414, 2013.

[79] G. Dixit, H. S. Chakraborty, and M. E-A. Madjet. Physical Review Letters, 111:233003, 2013.

[80] Á. Jiménez-Galán, L. Argenti, and F. Martín. Physical Review Letters, 113:263001, 2014.

[81] A. Marian, M. C. Stowe, J. R. Lawall, D. Felinto, and J. Ye. Science, 306:2063–2068, 2004.

[82] J. Su, H. Ni, A. Becker, and A. Jaroń-Becker. Physical Review A, 87:033420, 2013.

[83] J. Su, H. Ni, A. Becker, and A. Jaroń-Becker. Journal of Modern Optics, 60:1484–1491, 2013.

[84] C.-H Zhang and U. Thumm. Physical Review A, 84:033401, 2011.

[85] M. Ivanov and O. Smirnova. Physical Review Letters, 107:213605, 2011.

[86] A. S. Kheifets and I. A. Ivanov. Physical Review Letters, 105:233002, 2010.

[87] J. M. Dahlström, A. L'Huillier, and A. Maquet. Journal of Physics B: Atomic and Molecular and Optical Physics, 45:183001, 2012.

[88] A. Maquet, J. Caillat, and R. Taieb. Journal of Physics B: Atomic and Molecular and Optical Physics, 47:204004, 2014.

[89] C.-H Zhang and U. Thumm. Physical Review A, 82:043405, 2010.

[90] R. Pazourek, S. Nagele, and J. Burgdörfer. Journal of Physics B: Atomic and Molecular and Optical Physics, 48:061002, 2015.

[91] H. Wei, T. Morishita, and C. D. Lin. Physical Review A, 93:053412, 2016.

[92] J. Su, H. Ni, A. Becker, and A. Jaroń-Becker. Physical Review A, 88:023413, 2013.

[93] J. Su, H. Ni, A. Becker, and A. Jaroń-Becker. Physical Review A, 89:013404, 2014.

[94] C. J. Joachain, N. J. Kylstra, and R. M. Potvliege. Atoms in Intense Laser Fields. University Press and Cambridge, 2012.

[95] F. H. M. Faisal. Theory of Multiphoton Processes. Springer and New York, 1987.

[96] X. M. Tong and S. Chu. Physical Review A, 55:3406–3416, 1997.

[97] X. M. Tong and C. D. Lin. Journal of Physics B: Atomic and Molecular and Optical Physics, 38:2593–2600, 2005.

[98] P. Atkins and R. Friedman. Molecular Quantum Mechanics. University Press and Oxford, 2011.

[99] W. Pauli. General Principles of Quantum Mechanics. Springer and Berlin, 1980.

[100] E. Cormier and P. Lambropoulos. Journal of Physics B: Atomic and Molecular and Optical Physics, 29:1667, 1996.

[101] B. Bergues, Z. Ansari, D. Hanstorp, and I. Yu. Kiyan. Physical Review A, 75:063415, 2007.

[102] J. Zhang and T. Nakajima. Physical Review A, 77:043417, 2008.

[103] J. H. Bauer. Journal of Physics B: Atomic and Molecular and Optical Physics, 49:145601, 2016.

[104] D. Bauer and D. B. Milošević. Journal of Physics B: Atomic and Molecular and Optical Physics, 49:145601, 2016.

[105] B. C. Hall. Lie Groups and Lie Algebras and Representations. Springer and New York, 2003.

[106] J. Crank and P. Nicolson. Advances in Computational Mathematics, 6:207–226, 1996.

[107] O. A. Sharafeddin, D. J. Kouri, and D. K. Hoffman. Canadian Journal of Chemistry, 70:686–692, 1992.

[108] W. H. Press. Numerical Recipes: The Art of Scientific Computing and Third Edition. University Press and Cambridge, 2007.

[109] Vicente Hernandez, Jose E. Roman, and Vicente Vidal. ACM Trans. Math. Software, 31(3):351–362, 2005.

[110] C. Campos and J. E. Roman. SIAM J. Sci. Comput., 38(5):S385–S411, 2016.

[111] F. He, C. Ruiz, and A. Becker. Physical Review A, 75:053407, 2007.

[112] L. Tao, W. Vanroose, B. Reps, T. N. Rescigno, and C. W. McCurdy. Physical Review A, 80:063419, 2009.

[113] A. Scrinzi. Physical Review A, 81:053845, 2010.

[114] M. Ossiander, F. Siegrist, V. Shirvanyan, R. Pazourek, A. Sommer, T. Latka, A. Guggenmos, S. Nagele, J. Feist, J. Burgdörfer, R. Kienberger, and M. Schultze. Nature Physics, 13:280–285, 2017.

[115] M. Abramowitz and I. Stegun. Handbook of Mathematical Functions with Formulas and Graphs and Mathematical Tables. Dover and New York, 1965.

[116] S. Klarsfeld. Il Nuovo Cimento A, 43:1077–1094, 1966.

[117] N. Saad and R. L. Hall. Journal of Physics A: Mathematical and General, 36:7771–7788, 2003.

[118] L. R. Moore, M. A. Lysaght, J. S. Parker, H. W. van der Hart, and K. T. Taylor. Physical Review A, 84:061402, 2011.

[119] M. Sabbar, S. Heuser, R. Boge, M. Lucchini, T. Carette, E. Lindroth, L. Gallmann, C. Cirelly, and U. Keller. Physical Review Letters, 115:133001, 2015.

[120] L. Cattaneo, J. Vos, M. Lucchini, L. Gallmann, C. Cirelli, and U. Keller. Optics Express, 24:29060, 2016.

[121] C. Palatchi, J. M. Dahlströhm, A. S. Kheifets, I. A. Ivanov, D. M. Canady, P. Agnostini, and L. DiMauro. Journal of Physics B: Atomic and Molecular and Optical Physics, 47:245003, 2014.

[122] S. Saha, A. Mandal, J. Jose, H. R. Varma, P. C. Deshmukh, A. S. Kheifets, V. K. Dolmoatov, and S. T. Manson. Physical Review A, 90:053406, 2014.

[123] M. Magrakvelidze, M. Madjet, G. Dixit, M. Ivanov, and H. S. Chakraborty. Physical Review A, 91:063415, 2015.

[124] M. Magrakvelidze, M. Madjet, and H. S. Chakraborty. Physical Review A, 94:013429, 2016.

[125] E. E. Krasovskii and M. Bonitz. Physical Review A, 80:053421, 2009.

[126] K. L. Ishikawa and K. Udea. Applied Sciences, 3:189–213, 2013.

[127] R. McWeeny. Molecular Physics, 4:311–321, 1958.

[128] V. Elser and R. C. Haddon. Nature, 325:792–794, 1987.

[129] J. Kaushal, F. Morales, and O. Smirnova. Physical Review A, 92:063405, 2015.

[130] S. Svensson, B. Eriksson, N. Martensson, G. Wendin, and U. Gelius. Journal of Electron Spectroscopy and Related Phenomena, 47:327–384, 1988.

[131] K. Gottfried and T. M. Yan. Quantum Mechanics: Fundamentals. Springer and New York, 2003.